University of Alberta

Self-Assembly of Block Copolymers for Nanopatterning

by

Nathanael Lap-Yan Wu

A thesis submitted to the Faculty of Graduate Studies and Research
in partial fulfillment of the requirements for the degree of

Doctor of Philosophy

in

Microsystems and Nanodevices

Department of Electrical and Computer Engineering

Spring 2014
Edmonton, Alberta

Abstract

The impressive developments in the semiconductor industry over the past five decades have largely been dependent on the ability to continually reduce the dimensions of devices on a chip. However, as critical dimension requirements for these devices approach the limits of photolithography, new fabrication strategies must be introduced for these remarkable advances to continue. One technology listed by the International Technology Roadmap for Semiconductors as a candidate for next-generation nanostructure fabrication is the directed self-assembly of block copolymers. Block copolymers have received significant attention of late for their ability to template large regular arrays of nanostructures with dimensions ranging from 10 to 50 nm. The production of denser sub-10 nm nanostructures is also possible by reducing the size of these polymers, but a reduction of the polymer size also compromises the quality of nanostructures, making small polymers extremely difficult to use.

In this thesis, two different patterning approaches are introduced to push the nanostructure density limits possible for a given polymer. In the first, a novel patterning approach involving thin films of bilayer block copolymer domains

is used to effectively double the nanostructure density patterned by a given polymer. The technique is successfully applied to different types and sizes of polymer, and can also form highly controlled arrays of patterns with the help of surface topography. By varying different process parameters during the self-assembly or subsequent plasma steps, the dimensions of these density-doubled patterns may be finely-tuned to the desired width and pitch. The surface coverage of these density-doubled nanostructures is also maximized through adjusting the film thickness and parameters in the self-assembly process.

Besides using bilayer films, dense arrays of nanostructures may also be patterned using a multi-step patterning approach. In this approach, multiple layers of block copolymer films are subsequently deposited onto the substrate to template nanostructures. Because nanostructures from previous layers contribute to the surface topography, they influence the self-assembly of successive layers and more dense and complex patterns may be produced as a result.

Preface

This thesis is organized into 6 chapters. Chapter 1 describes the current trends in nanostructure fabrication and why block copolymer self-assembly is a promising patterning technology. Chapter 2 serves to familiarize the reader with basic concepts in polymer chemistry and self-assembly, and describes the recent developments in using block copolymer self-assembly to fabricate nanostructures. Chapter 3 then introduces a new technique of effectively doubling the density of nanostructures using bilayer films of cylinder-forming block copolymers. Chapter 4 investigates various methods of tuning the dimensions of these density-doubled nanostructures. Chapter 5 then explores the effect of surface topography on density-doubled patterns, and uses multiple layers of block copolymer films to create more dense and complex patterns. Finally, chapter 6 summarizes the main conclusions of this thesis and highlights several areas for future study.

Acknowledgements

First of all, I would like to thank my supervisors Prof. Jillian Buriak and Prof. Michael Brett for giving me the opportunity to work in such a high-calibre group. I was able to learn so much through the many experiences and through the wonderful people that I got to meet during these past 5 years. I particularly want to thank Jillian for providing me with continual guidance, support, and feedback, and encouraging me to move out of my comfort zone. Her wealth of knowledge, enthusiasm, and love of science has taught me so much about research and how to better express my ideas during presentations.

While in the Buriak group, I also had the privilege of working with many excellent collaborators, including Dr. Kenneth Harris, Dr. Xiaojiang Zhang, Jeffrey Murphy, Jeremy Bau, Dr. Erik Luber, Jennifer Bruce, Dr. Brian Worfolk, Fenglin Liu, Bing Cao, Shuai Chen, and Cong Jin. I would particularly like to thank Ken for the countless discussions in his office, and for his ideas and support whenever I was stuck. Xiaojiang, a brilliant experimentalist and a great friend, also provided me with considerable help in the beginning when I was struggling with the solvent annealing work. I would also like to thank Jeffrey, who greatly facilitated this research through his work in automating ellipsometry measurements and image analysis, and through his extensive knowledge.

I would also like to thank all the kind staff in the Nanofab — Stephanie Bozic, Jolene Chorzempa, Keith Franklin, Les Showalter, Scott Munro, and Dr. Eric Flaim — for their training and support. The staff at the Alberta Centre for Surface Engineering and Science (ACSES) — Dr. Dimitre Karpuzov, Dr. Anquang He, and Shihong

Xu — also provided considerable support and expertise that was helpful for this research. Daniel Salamon and Paul Concepcion from the National Institute for Nanotechnology (NINT) provided training and support for the SEM, which was used extensively for this project. This research would also not have been possible without the generous support from NSERC and Alberta Innovates.

Lastly, this thesis would not exist without the love and support of my family. Many thanks to my parents Patrick and Gina, who have taught me the value of discipline and hard work and have provided me with so many opportunities to explore my interests, and to my brother Barnabas for making my life so much more fun and interesting.

Contents

List of Tables

List of Figures

List of Symbols

Symbol	Meaning [units]	Symbol	Meaning [units]
a	Kuhn length [nm]	N	Degree of polymerization
b	Block interfacial width [nm]	N_A	Avogadro's number
χ	Flory-Huggins parameter	P	Pressure [Pa]
d	Cylinder diameter [nm]	ϕ	Volume fraction
D	Degree of swelling	R	Ideal gas constant [J/mol K]
$\vec{E}$	Electric field [V/m]	R_D	Displacement length [nm]
ϵ	Permittivity [F/m]	R_g	Radius of gyration [nm]
F	Fill ratio	ρ	Resistivity [Ω cm]
ΔF_{mix}	Free energy of mixing [J]	ϱ	Density [g/nm^3]
γ	Surface energy [J/m^2]	ΔS_{mix}	Entropy of mixing [J/K]
h	Polymer film thickness [nm]	σ_j	BCP junction area [nm^2]
ΔH_{mix}	Enthalpy of mixing [J]	t	Time [s]
k	Rate constant [m^3/s]	T	Temperature [K]
k_B	Boltzmann constant [J/K]	T_g	Glass transition temperature [K]
L	Characteristic period [nm]	T_{ODT}	ODT temperature [K]
λ	Wavelength [nm]	V	Volume [m^3]
m	Mass [kg]	w	Line width [nm]
M_n	Number average molar mass [g/mol]		
M_w	Weight average molar mass [g/mol]		

List of Abbreviations

Abbreviation	Meaning
AFM	Atomic force microscope
ALD	Atomic layer deposition
BCP	Block copolymer
DRAM	Dynamic random-access memory
DSA	Directed self-assembly
EBL	Electron beam lithography
EUVL	Extreme ultraviolet lithography
FFT	Fast Fourier transform
HSQ	Hydrogen silsesquioxane
ITO	Indium tin oxide
ITRS	International Technology Roadmap for Semiconductors
LER	Line edge roughness
MIBK	Methyl isobutyl ketone
MSN	Mesoporous silica nanoparticle
NIL	Nanoimprint lithography
ODT	Order-disorder transition
OOT	Order-order transition
P2VP	Poly(2-vinylpyridine)
P4VP	Poly(4-vinylpyridine)
PAA	Poly(acrylic acid)
PB	Polybutadiene
PDMS	Poly(dimethyl siloxane)

Abbreviation	Meaning
PE	Polyethylene
PEO	Poly(ethylene oxide)
PFS	Polyferrocenylsilane
PI	Polyisoprene
PLA	Polylactide
PMMA	Poly(methyl methacrylate)
PS	Polystyrene
PTFE	Polytetrafluoroethane
PTMSS	Poly(trimethylsilylstyrene)
RIE	Reactive ion etch
RMS	Root mean square
SAM	Scanning Auger map
SAXS	Small-angle x-ray scattering
SEM	Scanning electron microscope
SIS	Sequential infiltration synthesis
TEM	Transmission electron microscope
TEOS	Tetraethyl orthosilicate
THF	Tetrahydrofuran
TMAH	Tetramethylammonium hydroxide
TPE	Thermoplastic elastomer
UV	Ultraviolet

1

Introduction

Nanotechnology is the design and fabrication of materials with dimensions on the order of 1 to 100 nm.[1] The field was first conceived in the famous 1959 lecture "There's Plenty of Room at the Bottom" by Nobel Laureate Richard P. Feynman, who envisioned that miniaturization and the manipulation of atoms would progress to the point where the entire Encyclopaedia Brittanica would be written using atoms on the head of a pin.[2] Since that time, interest and development in this field has grown at an unprecedented rate due to interest in the many unique chemical, electrical, optical, and mechanical properties that manifest only with structures of this length scale. These unique properties have allowed for the development of many novel devices for applications ranging from photonic crystals, integrated circuits, memory storage, sensors, and biological interfacing. Techniques now also exist that allow the manipulation, imaging, and characterization of structures of this scale and even of individual atoms or molecules.

One particular area that has experienced the effects of this rapid growth and development is the semiconductor industry. The past five decades have seen a steady march towards smaller and smaller devices such that the number of transistors per chip doubles every two years, as described by the trend famously known as Moore's Law.[3] This impressive exponential growth in transistor density has led to the rapid growth of computing power and device functionality, an exponential decrease in the cost per function of devices, and has allowed computers to penetrate and transform every aspect of our lives. To continue this development of technology, the Semiconductor Industry Association, in conjunction with other semiconductor associations around the world have developed the International Technology Roadmap for Semiconductors (ITRS). The ITRS is a roadmap that provides an industry-wide consensus of the most current research and developmental milestones that must be satisfied in the next 15 years if the growth described by Moore's Law is to continue. One area of particular importance as highlighted in the ITRS is the fabrication of increasingly narrow and dense nanoscale features for the production of semiconductor devices. Devices produced in the industry are usually referred to by the half-pitch of line patterns used in their fabrication. The 22 nm device generation currently in production (see Figure 1.1) still makes use of a patterning process known as photolithography, but as devices continue to shrink to line half-pitches of 16 or 11 nm, photolithography will need to be replaced by newer processes capable of producing these narrow features. This chapter will first describe the process of photolithography, which has been in use throughout the development of the semiconductor industry, as well as its limitations and why newer technologies are required. Several potential candidates for the next generation of lithography are then introduced, including extreme ultraviolet lithography (EUVL), maskless lithography, nanoimprint lithography (NIL), and directed self-assembly (DSA). The work of this thesis will then be introduced within the context of some of the challenges that need to be overcome for DSA to be used in industry.

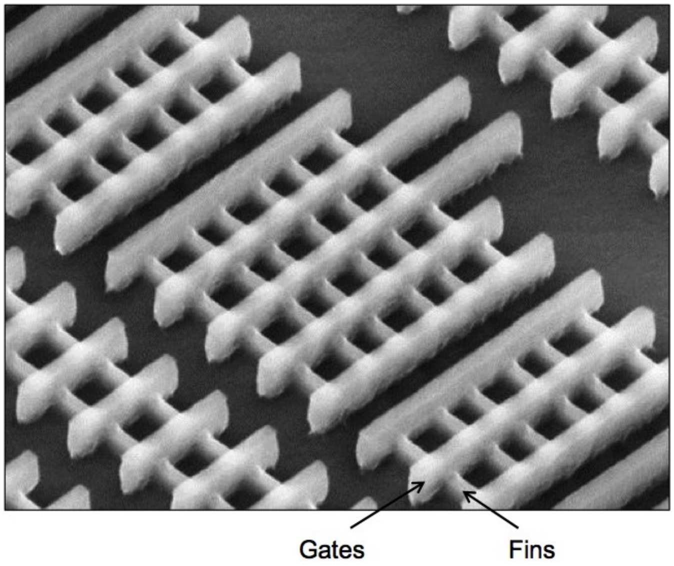

Figure 1.1: Intel's 22 nm tri-gate transistor was introduced into the market in 2011. An SEM of one such device is shown here (scale bars were not provided by the source). Reprinted with permission from ref. [4]. Copyright © 2011 Intel Corporation.

1.1 Photolithography

The impressive advances of the semiconductor industry over the past five decades have depended heavily on developments in photolithography.[5–7] Photolithography is the process where an opaque geometric pattern from an otherwise transparent photomask is projected by ultraviolet (UV) light onto a photosensitive polymer film known as photoresist (Figure 1.2). When photoresist is exposed to UV radiation above a certain dose threshold, chemical changes occur in the film that manifest as local changes in solubility of the polymer in a developer. Two different classes of photoresist may be used in photolithography: positive and negative photoresists. In positive photoresists, UV radiation facilitates the decomposition of the polymer, rendering exposed regions more soluble in the developer; while in negative photoresists, the UV radiation facilitates the cross-linking of photoresist, rendering exposed regions less soluble in the developer. A subsequent development step immerses the

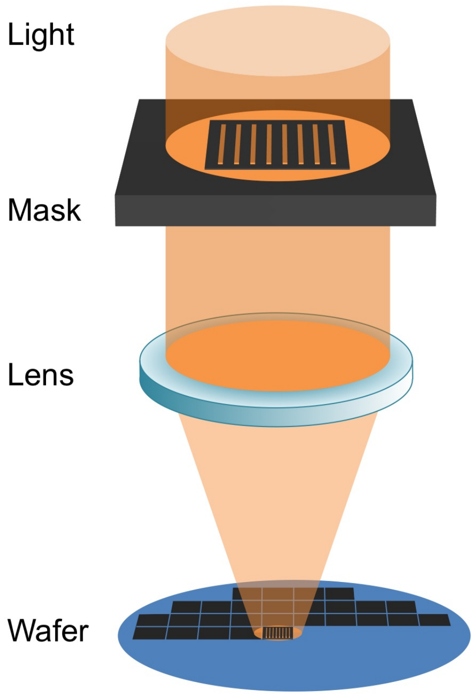

Figure 1.2: In photolithography, a mask pattern is projected by refractive optics onto a thin film of photoresist through UV light. The photoresist pattern is then transferred to the underlying wafer through an etching process.

film in the developer, which removes the soluble portions of the photoresist and leaves behind a geometric pattern corresponding to the one from the photomask. This geometric pattern is then transferred to the underlying material through an etching process, which selectively removes the exposed material not covered by the photoresist. When accompanied by material deposition steps, this simple patterning process may be used repeatedly to build up devices in a layer-by-layer fashion. As computer chips have continued to develop with increasing complexity, more and more photomasks are required to form these devices and connect them into a functional unit. A typical wafer process flow will consist of over 450 different steps and require two to three months to complete.[8]

The process of photolithography relies heavily on refractive optics to project the geometric pattern onto the photoresist. Thus, the ability to pattern small features on a substrate is severely limited by the diffraction of light. The resolution limits of photolithography from diffraction are described by the Rayleigh equation (Equation 1.1.1), where R is the critical dimension; k_1 is the Rayleigh coefficient, which is dependent on processing conditions; λ_o is the wavelength of the light in vacuum; n is the refractive index of the medium above the substrate; and θ is the angular aperture of the lens. The product $n \sin\theta$ is known as the numerical aperture, NA of the optical system.

$$R = k_1 \frac{\lambda_o}{n \sin\theta} \tag{1.1.1}$$

As feature dimensions continued to be reduced, methods to extend the diffraction limits of light were developed to keep up with the stringent specifications required by the industry. From this equation, it is clear that one method of reducing the critical dimension of the system is to reduce the wavelength of light used. Between the 1960s and 1980s, spectral lines from mercury lamps were originally filtered and used to produce 436 nm (G-line) and 365 nm (I-line) light sources. However, with increasing demand for narrower features, systems using excimer lasers such as KrF (248 nm) and ArF (193 nm) were developed and used throughout the early 2000s into the present. With each successive decrease in wavelength, new photoresists had to be developed to be sensitive to the specific wavelengths in use. Attempts were made at reducing the wavelength further using F_2 excimer lasers (157 nm), but because 157 nm light is easily absorbed by air, water, silica, and many other materials, new photoresists and optical systems consisting of high-quality CaF_2 lenses also needed to be developed. Because these technical challenges could not be solved within the time frame set by the ITRS, the reduction in wavelength was not deemed to be worth the investment and the 157 nm iteration was ultimately abandoned in 2004.[5]

Instead, the medium between the lens and the substrate was replaced with water to increase the NA by a factor of around 1.4. This technique became known as immersion lithography, and was able to produce features with half-pitch as low as 40 nm.[3] Immersion lithography was quickly adapted because it was highly attractive economically, allowing the industry to reuse much of the existing tooling infrastructure. Because of the failure to implement F_2 excimer technology, 193 nm immersion lithography is the final iteration of conventional photolithographic processes. As feature half-pitches continue to decrease below 40 nm, next-generation lithography processes are expected to replace the traditional photolithography process. To date, however, these alternative approaches are still unready for implementation into the next generation of production processes. As a result, attempts to push 193 nm immersion lithography further were made by using double-patterning techniques.[3, 6] Several variations of double-patterning exist and their process flows are depicted in Figure 1.3. In standard double-patterning, features are patterned from two separate photomasks, where the features are separated to create patterns with twice the desired pitch. Once the first photomask has been exposed, developed, and etched into the underlying material, a new resist layer is deposited and the second photomask is aligned such that the features form in between the features from the first mask. Because this requires two of each of the coating, exposure, development, and etching steps, other methods of double-patterning have been investigated to reduce the number of steps.

One alternative approach is to use a dual-tone resist, which contains both positive-tone and negative-tone chemistries, and as a result exhibit two solubility transitions at different levels of UV exposure.[9] As the initially insoluble resist is exposed to larger doses of light, the first threshold is reached where the positive-tone component becomes soluble, allowing the resist to dissolve in solvent. As the exposure continues to increase, however, the negative-tone resist becomes cross-linked, preventing further solvation by the developer. Thus, one set of features from underexposed resist, and one set from overexposed resist combine to form density-doubled features by using only one exposure and development step. This method, however, only allows for very simple periodic structures such as line arrays to be doubly-patterned, and would therefore not

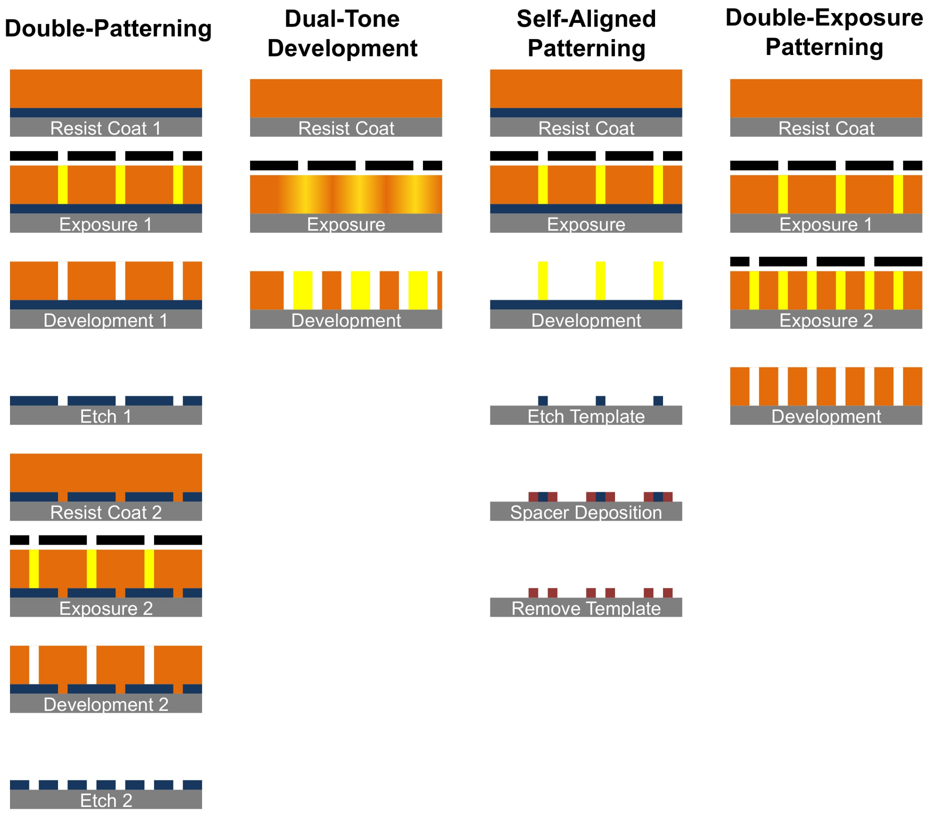

Figure 1.3: Process flows of standard double-patterning, dual-tone development, self-aligned double-patterning, and double-exposure patterning.

be useful for patterning more complex, non-periodic structures.

Another approach is the self-aligned double-patterning approach. In this case, a pattern is transferred to a template material. Spacers of silicon nitride are then added to surround the template material. By subsequently removing the template material, the resulting spacers become a mask with twice the density of the template material. Again, similar to the dual-tone development approach, this process is limited to the formation of periodic patterns because the patterns are defined by the edges of the template material.

One interesting approach is double-exposure lithography. In this approach, two separate patterns are sequentially exposed onto the photoresist to create features with double the density. The photoresist is then developed once to produce a combination of both patterns. This approach is the most challenging of all the methods described above because sub-threshold exposure of the photoresist from the first layer affects the amount of light required in the second step to bring the photoresist beyond the threshold. Methods must be developed to allow the material to "forget" the sub-threshold from the previous step before the second exposure is implemented. One possible solution is the introduction of a photochromic contrast enhancement layer above the photoresist. The contrast enhancement layer reversibly switches from opaque to transparent in the presence of sufficient UV radiation, allowing only the resist under the transparent regions to be exposed. The opacity is then restored prior to the second exposure step, thus preventing sub-threshold exposure from the two steps from accumulating in the resist and affecting the final pattern. Investigations into materials that would act as good contrast enhancement layers are ongoing.

As the feature densities continue to increase, the need for alternative patterning techniques become increasingly apparent. While double-patterning may be extended to triple-patterning or quadruple-patterning, each additional mask greatly increases the number of steps required in the process. This increases the time required to fabricate these devices, while at the same time decreasing the yield, making the additional steps highly costly for the manufacturing process. Thus, newer technologies are being explored as potential candidates to replace 193 nm immersion photolithography.

1.2 Next-Generation Lithography

The ITRS lists several candidates as replacements or complements for photolithography, including extreme ultraviolet lithography (EUVL), maskless lithography, nanoimprint lithography (NIL), and directed self-assembly (DSA). The following section will discuss these technologies in greater detail.

1.2.1 Extreme Ultraviolet Lithography

One of the alternative technologies that has received heavy industry investment is EUVL.[3, 10, 11] To push the diffraction limits of light, extreme-UV light is generated from plasma sources with temperatures reaching up to 100,000 K. The favoured source materials are from gaseous tin compounds, which are good emitters of radiation at 13.5 nm. Two methods of generating this plasma are Laser Produced Plasma (LPP), where a CO_2 laser pulse is used to generate the high-temperature plasma; and Discharge Produced Plasma (DPP), where a low-temperature plasma is compressed into a high-temperature plasma through the use of a magnetic field. While both methods are still viable options for EUVL, both also struggle in maintaining sufficient brightness for high wafer throughput. Based on the manufacturing throughput standard of 100 wafers per hour, a power source capable of producing >180 W is required to process wafers containing photoresists with a sensitivity of 10 mJ/cm^2. To date, this remains the greatest hurdle to overcome if EUVL is to take its place as an alternative for next-generation lithography.[3]

With the introduction of 13.5 nm light as the illumination source, vast changes must be made to the optics and masks. Because no material is sufficiently transparent for light at this wavelength, the refractive optics in conventional lithography systems cannot be used. Instead, the system is replaced by reflective optics, which make use of Bragg reflectors. These mirrors are made from alternating multilayers of molybdenum and silicon. Similarly, masks for EUVL are reflection masks with a base consisting of the alternating molybdenum and silicon layers. Absorbing material is then deposited on the mask and the geometric pattern is reflected onto the wafer with a size reduction factor of 4 or 5. A challenge associated with this reflective system that must be overcome is the problem of defects and heat. As the optics are exposed to extreme-UV radiation, the absorbed heat leads to diffusion of the silicon and molybdenum or to reactions on the mirror surface to produce surface roughness. All these effects lead to a decrease in the reflectivity of the optics, lowering the maximum contrast possible in the system. In the masks, these temperature

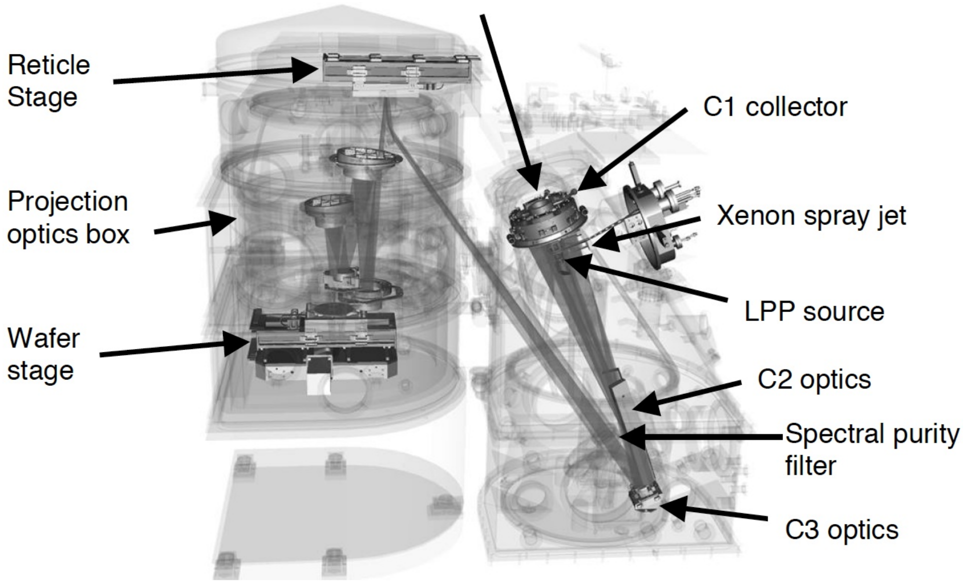

Figure 1.4: Cross section of an LPP EUVL system with a Xenon plasma source, reflective optics and mask, and wafer. Reprinted with permission from ref. [12]. Copyright © 2003 Society of Photo Optical Instrumentation Engineers.

changes also lead to thermal expansion, which could result in distortions in the mask patterns. Defects on the mask substrate or in the multilayers also pose significant problems in the patterning process and constitute the second greatest hurdle that must be overcome in EUVL.

Once the light has passed from the illumination source through the optics and mask, it must then interact with the photoresist films on the wafers. Due to the absorption of 13.5 nm light by air, this entire system must also be enclosed in a high-vacuum environment. Thus, the resists must also be compatible with this environment. The chemically amplified resists commonly used in immersion lithography consist of many small-molecule additives that may outgas in the high-vacuum environment and contaminate the optics. In addition to this, optimization of the resist sensitivity to 13.5 nm light, feature resolution, and feature line edge roughness (LER) are all areas that must be addressed. While significant progress has been made in these areas, LER continues to be a challenge listed in the ITRS that must be addressed.[3]

1.2.2 Maskless Lithography

Maskless lithography is a form of lithography, which as the name suggests, does not require a photomask to transfer a pattern onto the substrate. Instead, the pattern is written onto a resist one pixel at a time with a focused beam of energetic particles. The approach is able to break the diffraction limit of light through the use of particles such as electrons or ions, since these particles have much shorter wavelengths (λ) than light, as described by the de Broglie Equation (Equation 1.2.1). In the equation, h is Plank's constant, m is the mass of the particle, and E is the energy of the beam.

$$\lambda = \frac{h}{\sqrt{2mE}} \tag{1.2.1}$$

The most common form of maskless lithography is electron beam lithography (EBL), which operates similar to a typical scanning electron microscope (SEM).[13] Electrons are extracted from an electron source and accelerated across a high voltage through an anode to form a beam with energy ranging from 10 to 100 keV. The beam of electrons enters a column of electromagnetic lenses which transforms it into a highly focused beam with a narrow diameter on the order of 1 nm by the time it reaches the substrate. The beam is deflected by pairs of scanning coils or deflector plates to different positions on the substrate during the patterning process. For the beam to remain in focus, the deflection of the beam must remain within a range of a few hundred microns. This range is known as a write field, and for patterns larger than a write field, the patterns must be split into several write fields. For each write field, the substrate must be repositioned with mechanical stage movements, and consecutive write fields must be properly aligned with each other in a process known as stitching.

As the electron beam impinges on the resist material, some of the electrons interact with the resist, resulting in chemical changes similar to the ones observed in photolithography. Typical resists include hydrogen silsesquioxane (HSQ), which is a negative-tone resist that forms silica-like features upon exposure; and poly(methyl methacrylate) (PMMA), which is a positive-tone resist that becomes soluble in the developer upon exposure to the electron beam. The majority of the electrons, however, are deflected in different directions and scattered within the resist. The resulting volume of exposed resist is known as an interaction volume and is much larger than the original beam diameter. The shape and depth of this interaction volume controls the resolution limits of the process through the proximity effect, and is highly dependent on the energy of the beam and the substrate material. Besides the shape of the interaction volume, the duration of beam exposure and resist sensitivity are also important parameters to control during the writing process. EBL has been demonstrated to form structures with dimensions and pitch less than 10 nm.[14]

One of the major limitations of EBL is the serial nature of the writing process. Because only one electron beam is available for pattern transfer, the process is much too slow to match the 100 wafers per hour throughput required by industry. This throughput issue is being addressed by MAPPER Lithography through the introduction of a multi-beam system (see Figure 1.5).[15, 16] The system design consists of electron optics capable of splitting a single electron beam into over 13,000 parallel electron beams that may each be simultaneously deflected independent of each other. The system is expected to produce high-resolution features with as low as 11 nm half-pitch at a rate of 10 wafers per hour. A technology demonstrator with 110 parallel beams was built as a proof of concept and was shown to be able to produce patterns with a half-pitch of 22 nm. The machines capable of patterning 10 wafers per hour are still in development at the time of writing of this thesis.

Besides the use of electrons, ion beams may also be used as direct-write techniques. The use of focused ion beams may be used to further increase the resolution of patterned features.[17] Because ions are much heavier than electrons, they tend to have significantly lower scattering, thus reducing the influence

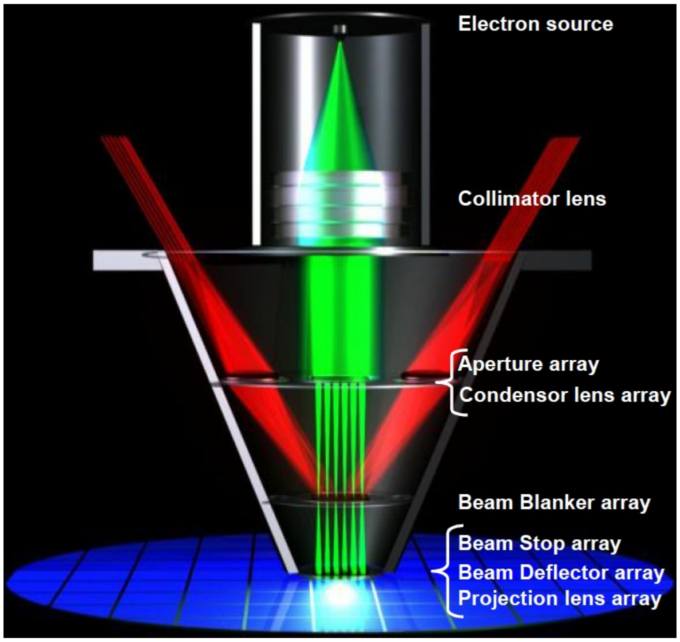

Figure 1.5: Schematic of the MAPPER EBL system demonstrating how a single electron beam splits into multiple beams for parallel writing. Reprinted with permission from ref. [15]. Copyright © 2008 Society of Photo Optical Instrumentation Engineers.

of the proximity effect in resist exposure. Focused ion beams may also be used to write patterns directly onto the substrate by direct ion bombardment. However, similar to EBL, focused ion beams also experience long write times due to their serial nature.

1.2.3 Nanoimprint Lithography

In NIL, surface nanoscale features on a polymer stamp are replicated onto a substrate through mechanical contact.[18] The process is divided into the imprinting, demolding, and etching steps (Figure 1.6). During imprinting, the stamp is brought into intimate contact with the substrate and a resist. The resist is displaced by the stamp features by squeeze flow and capillary forces to conform to the features of the stamp before solidifying. By adjusting the

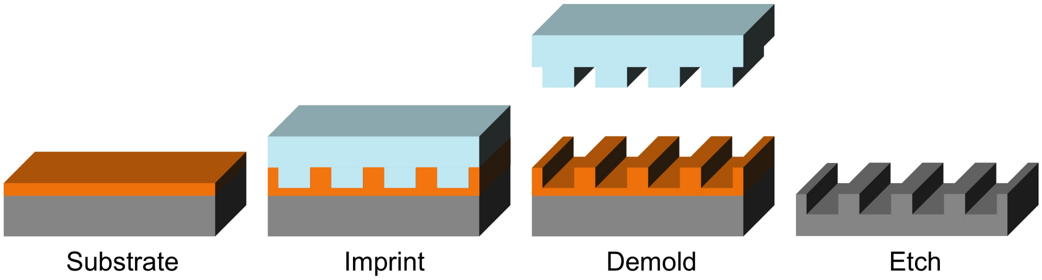

Figure 1.6: Schematic of the NIL patterning process as a substrate is passed through the imprinting, demolding, and etching steps.

features of the stamp, NIL could also be used to produce 3-dimensional reliefs in the resist. In the subsequent demolding step, the stamp is removed from the already solidified resist to produce free-standing structures that may then be used as an etch mask. During this step, the stamp and resist are subject to friction and adhesive forces that have the potential to damage the stamp or the resist. To minimize these problems, robust anti-adhesive coatings such as fluorinated silanes are commonly used for lowering surface energies. The ability to demold the stamp without damage, degradation, or contamination of the stamp is key, as failure to do so leads to defects in subsequent imprinting steps.

There are many different variations of NIL, but most methods fall into two categories depending on the method of resist solidification: thermal NIL and UV-NIL. In thermal NIL, the resist is a polymer film that is heated around 50 to 70 °C above the glass transition temperature of the film (more on glass transitions in Chapter 2), which transforms the film into a viscous liquid capable of conforming to the features of the stamp. The stamp is pressed into the film by a hard platen and a soft layer to equalize the pressure across the stamp. During the imprint step, the thickness of the resist film and the stamp feature width are critical in determining the amount of force required by the stamp to deform the resist. This process is governed by Stefan's equation (Equation 1.2.2), which describes the force (F) required to press a film of thickness h and viscosity η with a cylindrical feature of radius r at a rate of $\frac{dh}{dt}$.[19] After the imprinting is complete, the substrate is then cooled to temperatures around 20 °C below the glass transition to resolidify the resist and allow the stamp to be demolded.

$$F = \frac{3\pi r^4}{2h^3}\frac{dh}{dt}\eta \tag{1.2.2}$$

In contrast to thermal NIL, UV-NIL occurs entirely at room temperature. Instead of using polymer films as the resist, liquid films or droplets of precursors are used. Because of the low viscosity of the resist, only very low pressures are required, and the stamp may either be allowed to sink into the resist or is held at a constant position above the substrate as the voids between the stamp and substrate are filled by resist. While the liquid precursor fills these voids through capillary action to form a continuous resist, care must be taken to avoid the trapping of air in the voids, which could lead to missing or deformed structures. The back side of the stamps are integrated with a UV source, and subsequent exposure cross-links the precursors to form a solid relief of the stamp before it is removed. Resist materials for UV-NIL are designed for high cure rates, minimal shrinkage, and high etch-selectivity in subsequent etch steps that transfer the pattern from the resist to the underlying substrate.

NIL is an attractive patterning approach because it is a parallel and high-throughput process, capable of high-resolution patterning with a relatively low cost of ownership. While it is a candidate for next-generation lithography, NIL is also increasingly being used for patterning applications where following Moore's Law is not as important. It has great potential in applications such as data storage, optical displays, or even in sensor or biochip technologies. The NIL company Molecular Imprints has recently developed tools capable of patterning features for patterning hard disk drives, light-emitting diodes and semiconductor devices with 22 nm half-pitch lines. The largest obstacle preventing NIL from becoming a next-generation lithography process, however, is defect control. While small amounts of patterning produce excellent results,

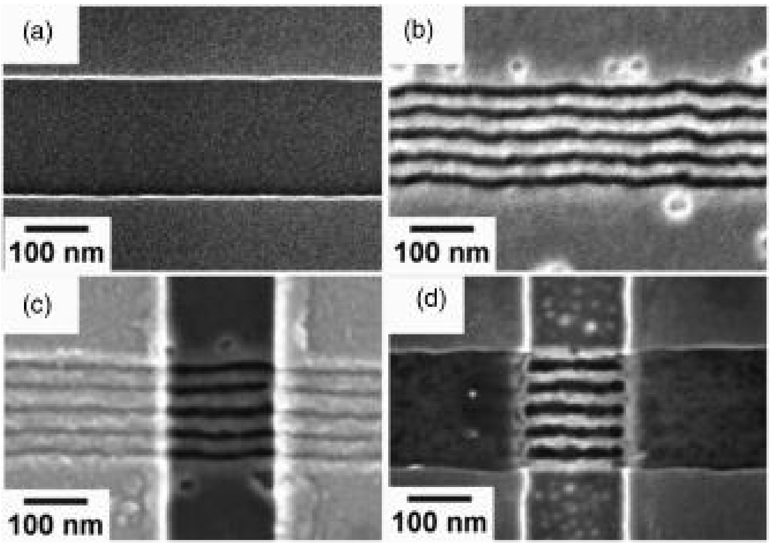

Figure 1.7: The fabrication of a silicon multi-nanowire transistor patterned using BCP DSA. The transistor channel was first lithographically patterned (a) and subdivided using BCP DSA (b). A second lithographic layer was deposited to mask the drain and source regions (c), and the device was completed after a subsequent silicon etch (d). Reprinted with permission from ref. [20]. Copyright © 2005 AIP Publishing LLC.

repeated stamp usage over multiple wafers demonstrate a dramatic increase in pattern defects as the stamps begin to degrade.

1.2.4 Directed Self-Assembly

The use of block copolymer (BCP) self-assembly is another promising method for next-generation lithography. BCPs have the ability to self-assemble into arrays of nanosized domains on the order of 10 to 50 nm which can then be converted into nanostructures, as will be described extensively in Chapter 2.[21–23] This low-cost process has been demonstrated to produce structures for devices including silicon nanowire transistors and bit patterned media (see Figures 1.7 and 1.8).[20, 24] Several other potential uses of BCP self-assembly as listed by the ITRS include lowering feature LER, tuning via diameters in integrated circuits, density multiplication for memory array patterning, and

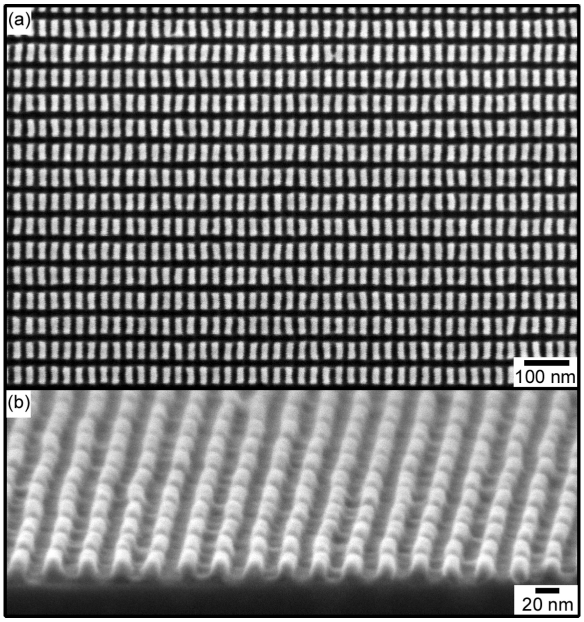

Figure 1.8: Plan view (a) and tilted (b) SEM images of bit patterned media templated by BCP DSA. Reprinted with permission from ref. [24]. Copyright © 2011 American Chemical Society.

density multiplication for logic.[3]

One limitation for this patterning technique, however, is the difficulty in controlling defects during the self-assembly process. For DSA to be a viable option for next-generation lithography, the defect densities must be <0.01 defects/cm^2. Through the use of pre-patterned chemical guiding patterns, significant progress was made recently to reduce the defect densities below 25 defects/cm^2.[25] Though this is still far from the 0.01 defects/cm^2 standard set by industry, the introduction of defect-tolerant architectures may be able to relax this standard and close the gap.[26] Besides the defect limitations, there are limitations on the complexity and density of the structures due to self-assembly.

Another limitation of BCP self-assembly is that the ability for BCPs to self-assemble decreases with polymer size. Thus, the fabrication of dense nanopatterns is also a challenge. This thesis explores different techniques that may be used to increase the density of patterned nanostructures and add complexity to the resulting structures. To begin the discussion, chapter 2 introduces the basic concepts of polymer chemistry and BCP self-assembly. The chapter then describes various techniques that have been developed to control the self-assembly, ordering, and transfer of BCP domains to free-standing nanostructures. In chapter 3, the concept of using bilayer cylinder BCP domains to push the density limits of BCP-patterned nanostructures is investigated. Chapter 4 then describes how various processing parameters—including solvent swelling, surface energy, and plasma—may be used to tune the dimensions of these density-doubled nanostructures. Chapter 5 then explores how a multi-step patterning approach may be used to create dense and interesting patterns not normally possible with single-step patterning. Finally, chapter 6 concludes with a summary of the results and a discussion of future directions for research.

References

[1] What is nanotechnology? National Nanotechnology Initiative. [Online]. Available: http://www.nano.gov/

[2] R. P. Feynman, "There's plenty of room at the bottom," *Engineering and Science*, vol. 23, no. 5, pp. 22–36, 1960.

[3] "International technology roadmap for semiconductors 2012 update," Semiconductor Industry Association, San Jose, CA, Tech. Rep., 2012. [Online]. Available: http://www.itrs.net

[4] Intel 22 nm technology. Intel Corporation. [Online]. Available: http://www.intel.com/content/www/us/en/silicon-innovations/intel-22nm-technology.html

[5] C. G. Willson and B. J. Roman, "The future of lithography: SEMATECH litho forum 2008," *ACS Nano*, vol. 2, no. 7, pp. 1323–1328, 2008.

[6] R. H. French and H. V. Tran, "Immersion lithography: Photomask and wafer-level materials," *Annual Review of Materials Research*, vol. 39, no. 1, pp. 93–126, 2009.

[7] D. P. Sanders, "Advances in patterning materials for 193 nm immersion lithography," *Chemical Reviews*, vol. 110, no. 1, pp. 321–360, 2010.

[8] M. Quirk and J. Serda, *Semiconductor Manufacturing Technology.* Upper Saddle River, NJ: Prentice-Hall Inc., 2001.

[9] S. J. Holmes *et al.*, "Edge lithography as a means of extending the limits of optical and nonoptical lithographic resolution," *Proceedings of SPIE*, vol. 3678, pp. 348–357, 1999.

[10] B. Wu and A. Kumar, "Extreme ultraviolet lithography: A review," *Journal*

of Vacuum Sciences & Technology B, vol. 25, no. 6, pp. 1743–1761, 2007.

[11] V. Bakshi, *EUV Lithography.* Bellingham, WA: SPIE Press, 2009.

[12] W. P. Ballard *et al.*, "System and process learning in a full-field, high-power EUVL alpha tool," *Proceedings of SPIE*, vol. 5037, pp. 47–57, 2003.

[13] J. I. Goldstein *et al.*, *Scanning Electron Microscopy and X-Ray Microanalysis*, 3rd ed. New York, NY: Springer, 2003.

[14] A. E. Grigorescu and C. W. Hagen, "Resists for sub-20-nm electron beam lithography with a focus on HSQ: State of the art," *Nanotechnology*, vol. 20, no. 29, pp. 292 001(1–31), 2009.

[15] E. Slot *et al.*, "MAPPER: High throughput maskless lithography," in *Proceedings of SPIE*, vol. 6921, 2008, pp. 69 211P(1–9).

[16] M. J. Wieland *et al.*, "Throughput enhancement technique for MAPPER maskless lithography," in *Proceedings of SPIE*, vol. 7637, 2010, pp. 76 371Z(1–11).

[17] K. Gamo, "Nanofabrication by FIB," *Microelectronic Engineering*, vol. 32, no. 1-4, pp. 159–171, 1996.

[18] H. Schift, "Nanoimprint lithography: An old story in modern times? A review," *Journal of Vacuum Sciences & Technology B*, vol. 26, no. 2, pp. 458–480, 2008.

[19] S. Franssila, *Introduction to Microfabrication*, 2nd ed. Chichester, UK: John Wiley & Sons, 2010.

[20] C. T. Black, "Self-aligned self assembly of multi-nanowire silicon field effect transistors," *Applied Physics Letters*, vol. 87, no. 16, pp. 163 116(1–3), 2005.

[21] S. Darling, "Directing the self-assembly of block copolymers," *Progress in Polymer Science*, vol. 32, no. 10, pp. 1152–1204, 2007.

[22] J. Bang *et al.*, "Block copolymer nanolithography: Translation of molecular level control to nanoscale patterns," *Advanced Materials*, vol. 21, no. 47, pp. 4769–4792, 2009.

[23] H.-C. Kim, S.-M. Park, and W. D. Hinsberg, "Block copolymer based nanos-

tructures: Materials, processes, and applications to electronics," *Chemical Reviews*, vol. 110, no. 1, pp. 146–177, 2010.

[24] R. Ruiz, E. Dobisz, and T. R. Albrecht, "Rectangular patterns using block copolymer directed assembly for high bit aspect ratio patterned media," *ACS Nano*, vol. 5, no. 1, pp. 79–84, 2011.

[25] C. Bencher *et al.*, "Self-assembly patterning for sub-15nm half-pitch: A transition from lab to fab," *Proceedings of SPIE*, vol. 7970, pp. 79 700F(1–9), 2011.

[26] J. R. Heath *et al.*, "A defect-tolerant computer architecture: Opportunities for nanotechnology," *Science*, vol. 280, no. 5370, pp. 1716–1721, 1998.

2

Basics of Block Copolymer Self-Assembly

The purpose of this chapter is to provide a brief introduction to BCP self-assembly and to describe some of the important developments of BCP self-assembly in the context of nanostructure fabrication. The chapter will begin with an introduction to the basic concepts and terminology used in polymer science. Following this introduction, the chapter will delve into the concept of self-assembly, especially as it applies to BCPs. The chapter will then move on to describe the complexities of BCP self-assembly in thin films, and some of the methods that have been developed to control the ordering of the self-assembly process. Finally, the chapter will end with a discussion on how these self-assembled patterns may be transformed into physical nanostructures for different applications.

2.1 Polymer Basics

Polymers are an important class of materials that are ubiquitous in our lives. They exhibit a diversity of physical or chemical properties that may be tuned through modification of the molecular structure. Polymers may be lightweight, hard, strong, or flexible; they may contain special thermal, electrical, and optical properties; or they may sometimes even be responsive to changes in the environment. As a result, they are used as structural components in construction materials like concrete and wooden beams; their lightweight and heat resistant properties make them ideal materials for different parts in the aerospace industry; they are used extensively for communications through optical fibres, cell phones, computers, books, and newspapers; they are found in clothing, fabrics and carpets; they have been used in energy storage applications such as lithium polymer batteries; and they are the primary component in many consumer products and toys.[1] In fact, polymers are the very basis of life itself, as all of the structural components, information storage, and complex machinery found in functioning living organisms depend on polymers such as proteins, polysaccharides, and polynucleotides. While humans have been using and manipulating natural polymeric materials throughout all of history, interest and an understanding of polymers did not develop significantly until the discovery of the vulcanization of natural rubber. The discovery of this process allowed for many man-made products including toys, furniture, and clothing to be produced for the first time. Over time, other synthetic polymer materials were developed including nylon 66, polystyrene (PS), polytetrafluoroethane (PTFE), polyethylene (PE), and polyisoprene (PI). The usage of synthetic polymers has grown to the extent that in the United States alone, over 100 billion pounds of synthetic polymers are consumed each year.[1]

Derived from the Greek words for many (*poly*) and units (*meros*), the word *polymer* describes any large molecular compound consisting of many basic repeating units. These building blocks may be identical as in the case of homopolymers, or they may be different as in the case of copolymers. The simplest way for these building blocks or monomers to be assembled is to connect them in a linear chain. However, as shown in Figure 2.1, polymers may also form more complex configurations such as circular polymers, branched polymers, star-shaped polymers, or even large cross-linked networks. Such variations in configuration are important because they affect the mechanical properties of the polymer. Several attributes of polymers are particularly important in the self-assembly of BCPs, and will therefore be explained in greater detail in the following sections.

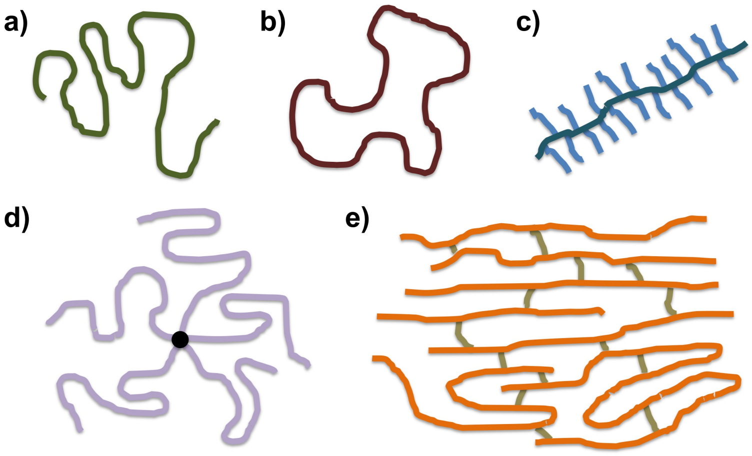

Figure 2.1: Polymers may take on a variety of configurations including linear (a), circular (b), branched (c), star-shaped (d), or large network structures (e).

2.1.1 Chain Sizes

One of the most important factors influencing a polymer's physical properties is its size or length. Short-chain polymers behave like small molecules, but as more monomers are added to form larger polymers, greater chain entanglement and intermolecular forces lead to higher polymer melting temperatures, mechanical strength, and viscosity. There are several parameters that describe a polymer's length. One such parameter is the degree of polymerization (N), which describes the number of monomeric units used to form a polymer chain.

A more common measure of polymer size is the molar mass of a polymer, which describes the mass of a single polymer chain. Polymer melts are composed of polymer chains with a distribution of molar mass that is dependent on the synthesis method of the polymer.[2] As a result, when describing the polymers in a particular melt, it is important not only to describe the average molar mass, but also the distribution of the molar mass. Different averages of the molar mass may be used, but two common ones are the number average molar mass (M_n), and the weight average molar mass (M_w).

The M_n is defined as shown in Equation 2.1.1, where n_i is the number fraction of molecules with molar mass M_i. Most of the thermodynamic properties of a polymer film, including the density, specific heat capacity, and refractive index, are dependent on M_n. Several ways of measuring M_n include osmometry and end-group analysis or radioactive labelling, since osmotic pressures and the number of end-groups are dependent on the number of molecules present, and not the size.

$$M_n = \frac{\sum_i M_i n_i}{\sum_i n_i} \tag{2.1.1}$$

The M_w is defined as shown in Equation 2.1.2, where w_i is the weight fraction of molecules with molar mass M_i. M_w is measured through analysing scattering patterns of laser light, X-rays, or neutrons passed through solutions of polymers. These scattering techniques are sensitive to M_w because scattering intensity is dependent on the molar mass of a polymer.

$$M_w = \frac{\sum_i M_i w_i}{\sum_i w_i} = \frac{\sum_i M_i^2 n_i}{\sum_i M_i n_i} \tag{2.1.2}$$

The polydispersity index (PDI) describes the distribution of polymer chain sizes within the melt. It is calculated by taking the ratio M_w/M_n, and will equal unity for a monodisperse melt of polymer. As polymer melts consist of wider distributions of sizes, the PDI also increases accordingly. This measure of size distribution in a polymer melt is particularly important because some physical properties such as tensile and impact strength are influenced more by the shorter molecules in the melt; properties such as the viscosity are influenced more by medium ranged molecules; and properties such as elasticity are influenced the most by the longest molecules present.[2]

2.1.2 Polymer Conformations

Most long-chain linear polymers have the capacity to assume a great number of conformations due to the large degree of rotational freedom about each single bond in the chain. The near-limitless number of possible configurations allow for statistical methods to be extremely effective in predicting the average behaviour of these chains. The physical properties of these polymers can then be described as functions of this average conformational behaviour. The most widely used parameter describing the conformation of polymer chains is the displacement length.[3] The displacement length (R_D), which describes the root mean square (RMS) end-to-end distance of polymer chains within the melt, is often used to describe the elastic behaviour or the effective size of polymers.

The simplest model to describe polymer conformation is the random walk model, which treats the polymer as N freely jointed, non-interacting rigid Kuhn segments of length a (known as the Kuhn length). If each of these segments are represented by a vector $\vec{a}_k$ with magnitude a, the end-to-end vector $\vec{R}_D$ may be written as follows:

$$\vec{R}_D = \sum_{k=1}^{N} \vec{a}_k \tag{2.1.3}$$

Subsequently, the results in Equation 2.1.4 may be obtained by taking the ensemble average of the displacement length.

$$R_D = a\sqrt{N} \tag{2.1.4}$$

While the displacement length may be used to successfully describe many physical properties of linear polymers, the definition becomes ambiguous if applied to non-linear polymers. In such cases, the radius of gyration (R_g), which describes the RMS distance of a chain element from the centre of mass of the polymer chain, is a much better descriptor of the non-linear polymer conformations.

The radius of gyration of a polymer is defined as shown in Equation 2.1.5, where the position of each monomer is denoted by the vector $\vec{r}$, and the centre of mass of the polymer is denoted by $\vec{r}_{mean}$. For linear polymers, it may be shown that the ensemble average of R_g is related to the displacement length by a factor of $\frac{1}{\sqrt{6}}$ as shown in Equation 2.1.6. Branched polymers will have lower R_g than linear polymers of the same molar mass, since the mass is distributed more to the middle of the chains.

$$R_g^2 = \frac{1}{N}\sum_{k=1}^{N} |\vec{r}_k - \vec{r}_{mean}|^2 \qquad (2.1.5)$$

$$R_{g,linear} = \frac{1}{\sqrt{6}} a\sqrt{N} \qquad (2.1.6)$$

2.1.3 Transition Temperatures

Typical small-molecule materials exist in one of three (solid, liquid, and gas) phases and display sharp thermodynamic phase transitions between each of these phases. At these phase transitions, known as first-order phase transitions, physical properties such as density are discontinuous functions of temperature and pressure.

Due to their large molecular structure, polymers exhibit more complex phase behaviour.[2] For example, because the molar masses of polymers are so large, the evaporation temperature greatly exceeds even the temperature for polymer decomposition. Thus, polymers do not exist in a gaseous state. Polymers generally exist in a partial or complete amorphous state, since they rarely form purely crystalline states. As a result, liquid polymers encounter phase transformations that are very different from small-molecule materials as they are cooled.

In polymers that are fully amorphous, transitions are governed by the kinetics of polymer chains. As an amorphous liquid polymer is cooled, the polymer chains gradually lose their mobility and gain a small degree of short-time stiffness. These changes in polymer mobility are made evident as the polymer melt becomes more rubbery. Rubbery polymers at room temperature such as polybutadiene (PB) can be treated to introduce small amounts of cross-linking, which chemically binds adjacent chains together (as in Figure 2.1e). Small amounts of cross-linking transforms these liquid rubbery materials into elastomers, which behave as solids due to the cross-links but still have the ability to stretch due to the polymer mobility.

As the rubbery polymers continue to cool, they encounter a transition often known as a glass transition temperature (T_g). At this critical transition point, the mobility of the polymer becomes too low for the chains to reorder into the equilibrium density. Because of these kinetic limitations, the polymer specific volume is larger than its equilibrium volume, and there is a change in rate at which the density decreases with temperature.[4] Below T_g, the polymer becomes hard and brittle and the chain mobility is so low that the chains are frozen and cannot slide past each other. The material is considered a glass, and although it is still a liquid, it has extremely high viscosity and hardness. The T_g is a transition that resembles a second-order phase transition because primary quantities like specific volume display an abrupt change in slope instead of a discontinuity. However, the T_g is not a true thermodynamic transition because it is a transition that can be controlled kinetically. The rate of cooling, the pressure, and the average molecular weight of the polymer are all parameters that influence the T_g of a polymer.

Some polymers are capable of forming both amorphous and crystalline regions, and are therefore considered semi-crystalline. These polymers characteristically have high degrees of geometrical regularity, which allows them to form crystals. Thus, in addition to the glass transition temperature, these liquid polymers also exhibit freezing behaviour into crystalline regions as they are cooled. This transformation, which occurs at temperatures above T_g, is a first-order phase transition and thus a discontinuity in specific volume is observed as the polymer is cooled.

2.2 Block Copolymers and Self-Assembly

As mentioned before, polymers may be composed of different combinations of monomer units. The ability to combine different functional units together allows polymers with multiple functionalities to be formed. More importantly, however, the arrangement of different functional components within a polymer can also lead to changes in the polymer chain conformation, which in turn affects the way that the polymer interacts with the environment. This folding and organization of polymers with respect to each other is sometimes known as self-assembly. The most extreme examples of how different sequences of monomer units can affect the overall polymer structure and properties are proteins. In humans, proteins consist of 20 different amino acid building blocks that combine into different sequences to give each protein its unique structure and function in the biological system. The protein haemoglobin, for example, is a good example of how self-assembly influences the conformation of polymers to form functional transporters of O_2 and CO_2 in many vertebrates. Other proteins self-assemble to form enzymes that catalyse specific reactions in a cell, channels that regulate the concentration of ions within a cell, or motors that are responsible for cellular motion. Similarly, DNA also consists of 4 unique building blocks, which combine to dictate the genetic makeup of an organism and encodes the program for all of its cellular functions.

While nature has proven itself to be extremely adept at using the self-assembly of complex polymers to store information, to self-replicate, and to regulate and perform cellular functions necessary for life; humans have a long way to go before we can even begin to match the complexity of design and function displayed in nature. However, even our elementary understanding of simple copolymer systems and their self-assembly can lead to the development of highly useful technologies. One type of copolymer that is particularly interesting in self-assembly and has been studied rather extensively is the linear BCP. Linear BCPs may be thought of as a collection linear homopolymer chains (or blocks) of different composition connected together sequentially at the ends. They are commonly denoted by listing all of the homopolymer block components sequentially, and separating each block with a "-*b*-". Thus, a copolymer consisting of a PI block and a PB block is denoted as PI-*b*-PB. The simplest form of a BCP is a diblock copolymer (diBCP), which consists of two distinct homopolymer chains covalently bonded together. To minimize the free energy of the system, similar blocks from BCPs tend to aggregate together and self-assemble to form a polymer melt with chemically distinct microdomains.

One of the important early uses for BCPs was as thermoplastic elastomers (TPEs), which exhibit rubber-like elastic behaviour while also being easily processable as a thermoplastic.[5] Kraton polymers, which are styrene-based BCPs with butadiene or isoprene blocks, are great examples of TPEs, and have been used commercially for components in automobiles since the 1970s.[6] The low T_g of the PB or PI blocks gave these TPEs their elastic behaviour, while the high T_g PS blocks phase-separated into glassy phases effectively acting as cross-links that helped to maintain the shape of the polymer. To mold the polymer into a different shape, the temperature of the polymer was simply raised above the T_g of the styrene blocks, allowing the polymer to reconfigure the styrene domain structures and be molded into the desired shape. Thus, unlike other elastomers, TPEs required no chemical cross-linking process, and so the polymers could be repeatedly and reversibly processed. Besides their use as easily processable TPEs, BCPs were also used as adhesives, emulsifiers, or coatings.[7] Another application for BCPs that has received significant attention recently is for the lithographic patterning of nanostructures on surfaces. This application was first discussed in the early 1990s, and holds great promise due to the inherent ability for BCPs to self-assemble into periodic arrays of patterns with dimensions ranging from 10 to 50 nm.[8, 9]

To gain an appreciation for why BCPs self-assemble into different structures, one must first understand how polymers behave in solutions. Thus, in this section, the Flory-Huggins theory of polymer solutions will be introduced. Following the discussion on Flory-Huggins theory, a brief overview of some of the concepts specific to BCP self-assembly in bulk and in thin films will be presented.

2.2.1 Flory-Huggins Theory of Polymer Solutions

Due to their large molecular weights, the behaviour of polymers in solution differ greatly from that of small-molecule solutes. A theoretical description of the behaviour of polymers in solutions was developed by Flory and Huggins in 1942,[7, 10, 11] and is briefly described below. The approach involves a statistical mechanical model consisting of interacting molecules within a lattice.

First, consider two pure small-molecule phases A and B made up of x_{Am} molecules of A (solvent) and x_{Bm} molecules of B (solute), within a filled lattice of $x_o = x_{Am} + x_{Bm}$ sites, as shown in Figure 2.2. Given that the entropy of a system can be described by Equation 2.2.1, where k_B is the Boltzmann constant, and Ω is the number of arrangements, the entropy of the pure phase prior to mixing is 0. Upon mixing, the entropy of mixing (ΔS_{mix}) may then be described as in Equation 2.2.2, using the Stirling approximation. ϕ_A and ϕ_B are the volume fractions of A and B, respectively ($\phi_A + \phi_B = 1$), assuming the volume of each molecule is approximately equal to the volume of a lattice cell.

$$
\begin{aligned}
S &= k_B \ln \Omega && (2.2.1) \\
\Delta S_{mix} &= k_B \ln \frac{(x_{Am} + x_{Bm})!}{x_{Am}! x_{Bm}!} \\
\Delta S_{mix} &= -k_B [x_{Am} \ln \frac{x_{Am}}{x_{Am} + x_{Bm}} + x_{Bm} \ln \frac{x_{Bm}}{x_{Am} + x_{Bm}}] \\
\Delta S_{mix} &= -k_B [x_{Am} \ln \phi_A + x_{Bm} \ln \phi_B] && (2.2.2)
\end{aligned}
$$

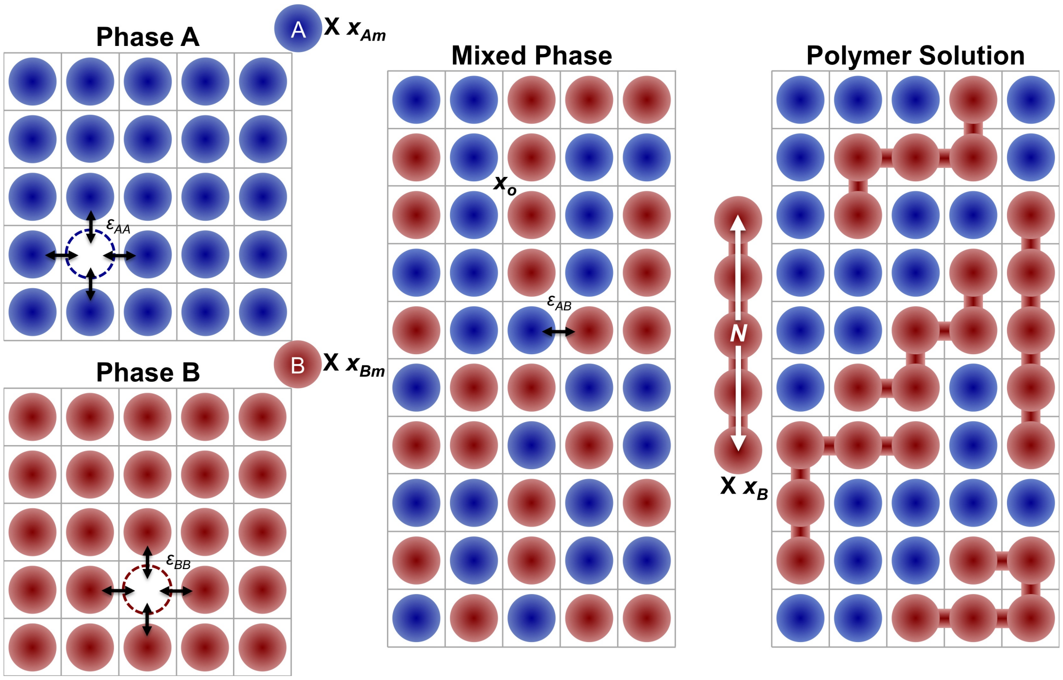

Figure 2.2: When x_{Am} and x_{Bm} molecules of A and B are mixed from two pure phases, A-A and B-B bonds with energies ε_{AA} and ε_{BB}, respectively, must be broken so that A-B bonds with energy ε_{AB} may be formed. Linear polymers behave in much the same way except the individual molecules are linked up in a chain.

Besides the change in entropy of the system during mixing, there is also a change in enthalpy of the system. During mixing, molecules of A and B must be removed from their respective pure phases, breaking the A-A and B-B bonds and reforming A-B bonds. The change in energy resulting from combining the two pure phases into a mixture is described by Equation 2.2.3, where n_{AB} is the number of A-B bonds formed, and ε_{AA}, ε_{BB}, ε_{AB} are the energies of the A-A, B-B, and A-B bonds. If n_{AB} is estimated as the number of A molecules multiplied by the bonds per molecule (z) and the fraction of neighbouring molecules which are B, the equation may be rewritten as shown in Equation 2.2.4. A dimensionless parameter (χ_{AB}) also known as the Flory-Huggins parameter, is introduced to describe the degree of incompatibility between A and B.

$$\begin{aligned}
\Delta H_{mix} &= n_{AB}[\varepsilon_{AB} - \frac{1}{2}(\varepsilon_{AA} + \varepsilon_{BB})] \qquad (2.2.3)\\
\Delta H_{mix} &= \frac{z x_{Am} x_{Bm}}{x_{Am} + x_{Bm}}[\varepsilon_{AB} - \frac{1}{2}(\varepsilon_{AA} + \varepsilon_{BB})]\\
\Delta H_{mix} &= \chi_{AB} k_B T x_{Am} \phi_B \qquad (2.2.4)\\
\chi_{AB} &= \frac{z[\varepsilon_{AB} - \frac{1}{2}(\varepsilon_{AA} + \varepsilon_{BB})]}{k_B T}
\end{aligned}$$

Now, consider a solution of two polymers, where x_{Am} molecules are connected into x_A linear polymer chains, each with degree of polymerization N_A ($x_{Am} = N_A x_A$), and where x_{Bm} molecules are similarly connected into x_B linear polymer chains, each with degree of polymerization N_B ($x_{Bm} = N_B x_B$). Under these conditions, additional constraints are imposed on the system, forcing monomers of the same chain to be adjacent to each other. Through these constraints, the entropy of mixing may be modified to become Equation 2.2.5. This equation is similar to Equation 2.2.2 except x_{Am} and x_{Bm} are replaced with x_A and x_B, which differ by factors of N_A and N_B, respectively. Thus, as the monomers A and B are increasingly polymerized (larger N_A and N_B), the entropy of the system decreases.

$$\begin{aligned}
\Delta S_{mix} &= -k_B[x_A \ln \frac{N_A x_A}{N_A x_A + N_B x_B} + x_B \ln \frac{N_B x_B}{N_A x_A + N_B x_B}]\\
\Delta S_{mix} &= -k_B[x_A \ln \phi_A + x_B \ln \phi_B] \qquad (2.2.5)
\end{aligned}$$

The free energy of mixing of a polymer in solution (ΔF_{mix}) as described in Equation 2.2.6, may be written in terms of both the entropy and enthalpy changes in the system during mixing. By substituting Equations 2.2.5 and 2.2.4, ΔF_{mix} may be written in terms of the χ_{AB} parameter, the degrees of polymerization N_A and N_B, and the volume fractions of A and B (Equation 2.2.7).

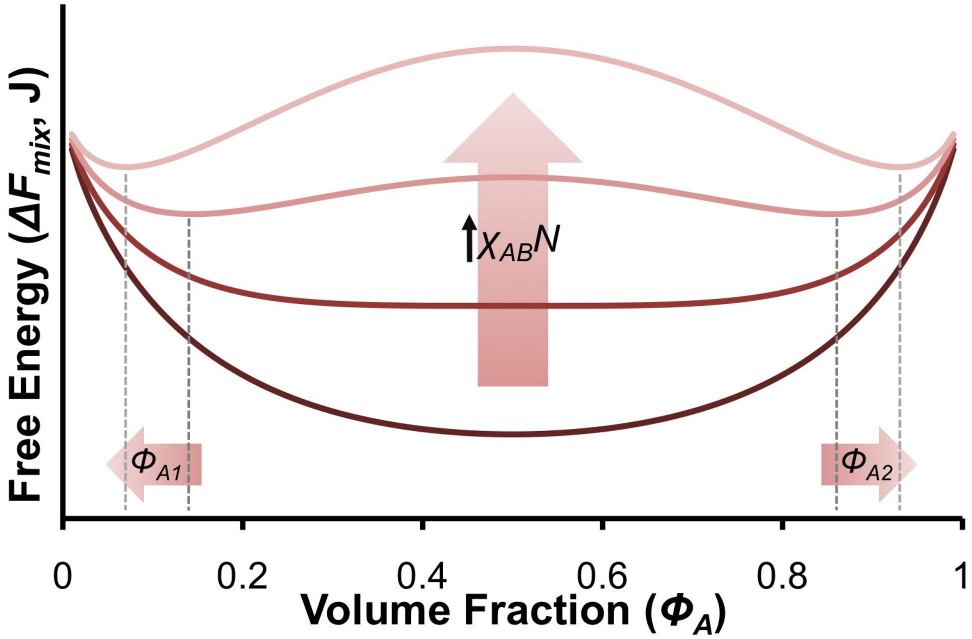

Figure 2.3: The free energy of mixing (ΔF_{mix}) is plotted with respect to the volume fraction of A (ϕ_A) for polymers with similar chain lengths ($N_A = N_B = N$). As the $\chi_{AB}N$ values increase, two minima in ΔF_{mix} appear, which allows phase separation to be a viable route to minimizing the system free energy.

$$\begin{aligned}\Delta F_{mix} &= \Delta H_{mix} - T\Delta S_{mix} && (2.2.6)\\ \Delta F_{mix} &= \chi_{AB}k_BTx_{Am}\phi_B + k_BT[x_A \ln \phi_A + x_B \ln \phi_B] \\ \frac{\Delta F_{mix}}{x_o k_B T} &= \chi_{AB}\phi_A\phi_B + \frac{\phi_A}{N_A}\ln \phi_A + \frac{\phi_B}{N_B}\ln \phi_B && (2.2.7)\end{aligned}$$

The behaviour of a mixture of two different polymers may be described through plotting ΔF_{mix} with respect to the volume fractions of A (see Figure 2.3). Assuming that the two polymers have similar chain lengths ($N_A = N_B = N$), and that the temperature is held constant, the product $\chi_{AB}N$ may be varied to alter the ΔF_{mix}, and thus also the behaviour of the polymer mixture. For low values of $\chi_{AB}N$, the ΔF_{mix} exhibits only one minimum at equal volume fractions of A and B. In such a case, the lowest free energy attainable for a system with any ϕ_A is to have one homogeneous phase with ϕ_A. As the product $\chi_{AB}N$ increases, however, the ΔF_{mix} develops into two local minima at different volume fractions. In these polymer systems, two free energy local minima exist at $\phi_A = \phi_{A1}$ and at $\phi_A = \phi_{A2}$. For polymer melts with $\phi_A < \phi_{A1}$ or $\phi_A > \phi_{A2}$, the lowest free energy state still corresponds to one homogeneous phase with volume fraction ϕ_A. Polymer melts with $\phi_{A1} < \phi_A < \phi_{A2}$, however, may phase separate into mixtures of ϕ_{A1} and ϕ_{A2} phases. Since the free energy of both ϕ_{A1} and ϕ_{A2} phases are lower than that of ϕ_A, the phase-separated arrangement of polymers is favoured over the existence of one homogeneous phase. As the product $\chi_{AB}N$ increases, the two phase compositions ϕ_{A1} and ϕ_{A2} rapidly approach pure A and pure B, respectively. This means that the compositions of the two phases become increasingly distinct as $\chi_{AB}N$ is increased.[*]

Thus, using this information about free energy, and assuming constant temperature, a phase diagram for the mixing of two polymers A and B may be constructed as shown in Figure 2.4.[12] Two lines, known as the spinodal and binodal lines, denote the boundary of the phases. The binodal line traces the volume fractions of the free energy minima as $\chi_{AB}N$ is increased, and denotes the boundary where phase separation is thermodynamically favoured. Outside the curve, the solutions formed remain disordered, but within the curve, phase separation becomes possible. The spinodal line traces the boundary of volume fractions where $\frac{\partial^2 \Delta F_{mix}}{\partial \phi_A^2} < 0$, and denotes where phase separation occurs spontaneously. Within the spinodal curve, phase separation occurs as random fluctuations in ϕ_A are quickly amplified and spontaneously separate into ϕ_1 and ϕ_2 through spinodal decomposition. Outside of the spinodal curve, the mixture remains metastable due to kinetic limitations, and phase separation occurs through the nucleation and growth mechanism.[†]

---

[*] Polymer mixtures with $N_A \gg N_B$ will also behave similarly, except the ΔF_{mix} of the ϕ_{A2} minimum will be lower than that of the ϕ_{A1} minimum. As $\chi_{AB}N$ is increased, the ϕ_{A1} phase will also approach a pure phase much more quickly than ϕ_{A2}.

[†] Polymer mixtures with $N_A \gg N_B$ produce similar phase diagrams, except the curves are asymmetrical.

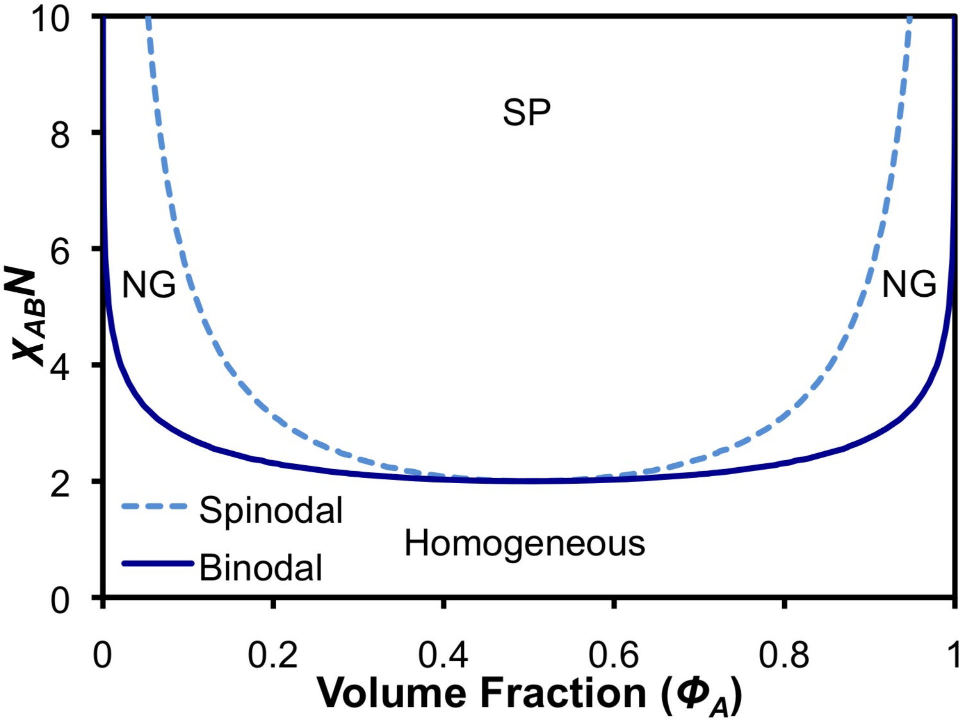

Figure 2.4: Phase diagram of a binary homopolymer blend. For low $\chi_{AB}N$, one homogeneous phase exists. When the binodal curve is crossed, phase separation is thermodynamically favoured. At first, this phase separation occurs through nucleation and growth (NG) due to limitations in the kinetics. When the spinodal curve is crossed, however, phase separation may occur spontaneously through spinodal decomposition (SP).

2.2.2 Self-Assembly in Bulk Diblock Copolymers

The results derived from the Flory-Huggins theory of polymer solutions are useful in understanding the self-assembly of bulk diBCP melts as well. Bulk diBCP melts may be thought of as a blend of two homopolymers with the extra constraint of having each A homopolymer covalently linked to a B homopolymer. Thus, these diBCP melts follow similar trends as those observed for a binary mixture of homopolymers. As the $\chi_{AB}N$ of the polymer melt is increased, the BCP melt remains as a homogeneous mixture until it reaches the transition point where phase separation is favoured. This transition, known as the order-disorder transition (ODT), is dependent on the volume fraction of the polymer. The minimum $\chi_{AB}N$ for the ODT occurs when the volume fractions of both blocks are identical. As the $\chi_{AB}N$ increases past the ODT point, the compositions of the two thermodynamically favoured phases become more and more distinct, asymptotically approaching pure A and pure B. This is the extent of the similarities between the phase separation of a binary homopolymer blend and a diBCP melt.

The extra constraints to self-assembly in a diBCP melt lead to limitations in the arrangement of polymers in the melt. Firstly, there is a limitation in the size of the phase-separated domains. Because each A block must be attached to a corresponding B block, the size of the A domains and B domains is strongly related to the length of the A blocks and B blocks, respectively. Secondly, there is also a limitation in the positioning of the junctions between A blocks and B blocks. These junctions must all be located at the interfaces between the phase-separated domains if the free energy of the system is to be minimized. Finally, chain stretching also occurs during the phase separation, especially at higher $\chi_{AB}N$ as the compositionally pure phase-separated domains increasingly limit the available positions for the two blocks. Early experiments demonstrated that these limitations force the phase-separated domains to assume arrangements such as parallel lamellae, hexagonally-packed cylinders, or spheres with body-centred cubic packing. Later, experiments also demonstrated the existence of a bicontinuous network, known as a gyroidal phase. Points where one phase transitions into another are known as order-order transitions (OOT).

Various theoretical models have been developed to predict the locations of OOTs and ODTs in bulk BCP melts. These theoretical descriptions of BCP thermodynamics historically fell into two distinct limits: the strong segregation limit, and the weak segregation limit.[13, 14] In the strong segregation limit, $\chi_{AB}N$ was assumed to be large such that the blocks segregated into two distinct pure phases with very narrow interfaces with respect to the domain dimensions. Polymer chain-stretching effects at these sharp interfaces were explicitly accounted for in this limit. Helfand and co-workers were among the first to develop a self-consistent field theory in this regime to describe the transitions between lamellar, cylindrical, and spherical BCP domains.[7, 15] However, the study most associated with the strong segregation limit was performed by Semenov, who estimated the polymer free energies at the asymptotic limit $\chi_{AB}N \rightarrow \infty$.[16] At the other extreme was the weak segregation limit, where $\chi_{AB}N$ was just large enough for phase separation, but where the volume fraction of polymers vary more gradually in space. At this limit, it was assumed that no changes in polymer conformation took place. Most of the work at this limit was inspired by Liebler, who constructed a Landau expansion of the polymer free energy with respect to polymer composition.[17] Over time, with the development of computational power and theoretical methods, self-consistent field theories that spanned across both the strong and weak segregation limits were developed.[18] It is through these models that BCP phase diagrams such as the one in Figure 2.5 are created. From these models, it is known that the minimum $\chi_{AB}N$ for self-assembly to occur is 10.5.

As shown in Figure 2.5, the type of structures observed in the bulk film are highly dependent not only on the $\chi_{AB}N$, but also on the volume fraction of the blocks. As indicated in the figure, when the BCP blocks are highly asymmetric, spheres (S) of the minority block inside a majority block matrix are observed. However, as the length of the blocks become more comparable, minority-block cylinder (C) and gyroidal (G) structures are observed. When the two blocks are approximately symmetric, the structures become parallel lamellae (L). As to be expected, the BCP phase diagram constructed through theoretical modelling is similar in shape to the phase diagram for binary homopolymer blends in Figure 2.4. The phase diagram constructed through experimental results also bears striking resemblance to the diagram constructed from the theoretical model. The differences in the phase diagrams, especially the presence of a perforated lamellar (PL) phase, have been mainly attributed to kinetic limitations in the system.[19]

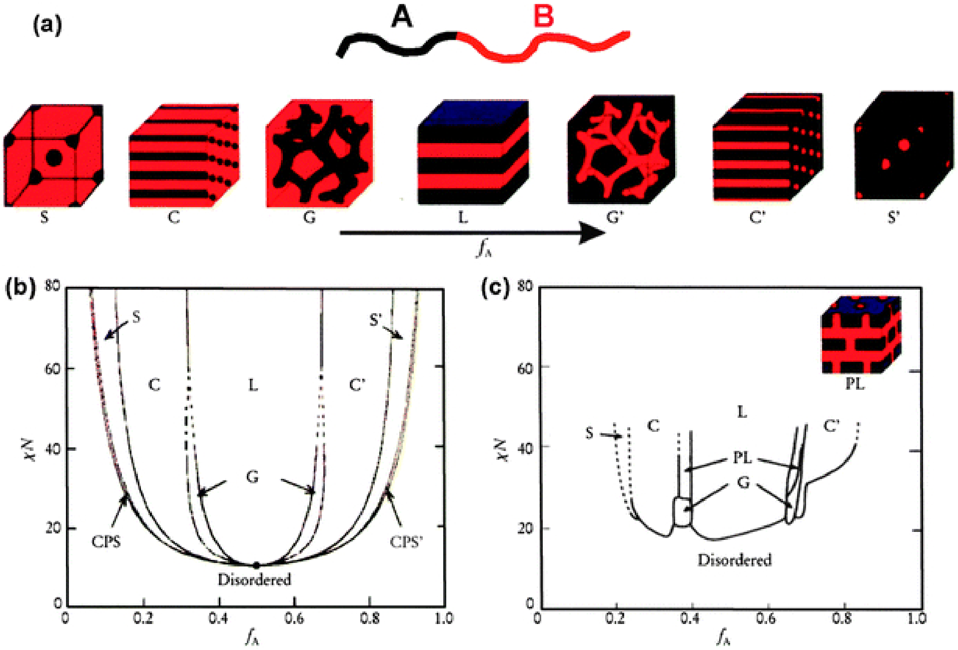

Figure 2.5: As the volume fraction of block A increases, various domain morphologies are favoured (a). The conditions required for each of these conditions are plotted on the phase diagrams below. Phase diagrams of bulk BCPs computed through theoretical models (b) and constructed through experimental results (c) are displayed. Reprinted with permission from ref. [19]. Copyright © 1999 AIP Publishing LLC.

2.2.3 Self-Assembly in Thin Films

The self-assembly of thin-film BCPs is held as a promising pathway for nanostructure fabrication. Unlike bulk BCPs, the self-assembly of thin-film BCPs are governed by an additional set of boundary constraints that contribute to added complexities and the formation of additional phases. The constraint of one dimension of the melt into a finite thickness reduces the symmetry of the system, introducing the concept of structure orientation. In addition to these dimensional constraints, the energetics of interaction at the two surfaces of the film (the air/BCP and BCP/substrate interface) also govern the self-assembly process and can alter the orientation of the resulting nanostructures depending on the specific application. For example, lamellar features parallel to the substrate surface may be used as diffusion barriers or optical coatings, while perpendicular cylindrical features may be used for nanoporous filters.

In general, the interfacial energies between the blocks and each of the film surfaces will differ due to differences in the chemical composition. As a result, one block usually preferentially wets each of the surfaces to minimize the surface energy at the interface. This preferential wetting at the interfaces also results in the favouring of structures forming parallel to the substrate, as observed in early studies of lamellar-forming BCPs.[20, 21] In these examples of lamellar-forming PS-*b*-PMMA systems on bare silicon, the polar PMMA blocks preferentially wet the native oxide at the BCP/substrate interface, while the non-polar PS blocks preferentially lined the air/BCP interface. As the BCP films self-assembled, the ordered structures parallel to the surface continued to propagate towards the centre of the films until all the structures in the films were oriented parallel to the surfaces.[21] The resulting films were asymmetric systems of parallel lamellar structures with discrete thicknesses or terraces equal to $(n + \frac{1}{2})L$, where n was any integer, and L was the characteristic period of the BCP (Figure 2.6a).

The energetics at the BCP/substrate and air/BCP interfaces could also be altered by the introduction of polymer layers. For example, random copolymers of PS-PMMA with tunable monomer compositions were synthesized and grafted onto the substrate prior to BCP film deposition to create BCP/substrate interfaces that were selective for PS, PMMA, or non-selective for both blocks.[22] If, for example, a pure PS layer was grafted at the BCP/substrate interface, then both air/BCP and BCP/substrate surfaces would be selective for the same block, resulting in a symmetric system of parallel lamellar structures with discrete thicknesses nL (Figure 2.6b). The introduction of a non-selective polymer surface layer resulted in the formation of perpendicular lamellar structures (Figure 2.6c).[23, 24] Because the air/BCP interface remained selective, however, the perpendicular lamellar structures did not propagate through the entire film thickness, and instead were interrupted by parallel lamellae near the air/BCP interface. Thin polymer films could be introduced above the

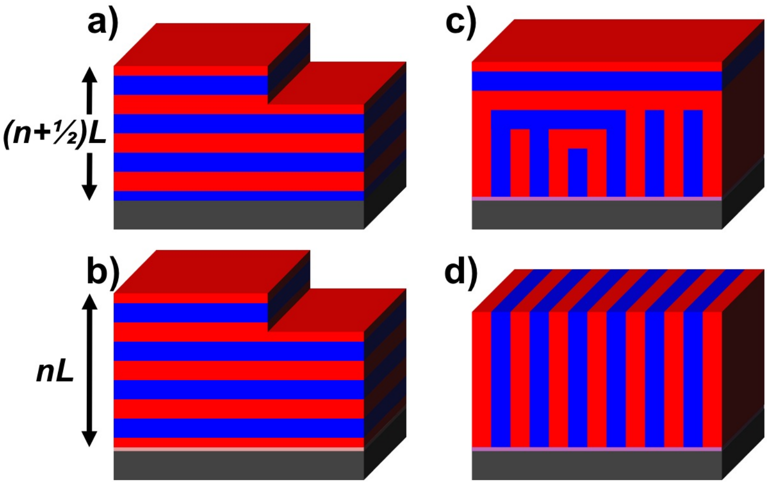

Figure 2.6: The orientation of lamellar patterns in BCP thin films depend on the surface conditions at the air/BCP and the BCP/substrate interfaces. Surfaces that are selective for different blocks (a) or the same block (b), will lead to discretized film thicknesses with step sizes equal to the characteristic period L. When the BCP/substrate interface is non-selective, no discretization of thickness occurs, but the air/BCP interface will consist of either parallel or perpendicular lamellae depending on whether the interface is selective (c) or non-selective (d) for a block.

BCP sample prior to the BCP self-assembly to alter the energetics at the air/BCP interface. If the film was non-selective, the BCP film was allowed to self-assemble into perpendicular lamellae that propagated across the entire thickness of the film (see Figure 2.6d).[25–27]

Thin-film self-assembly of cylinder-forming BCPs was significantly more complex than the lamellar structures observed above.[28–30] Besides the formation of perpendicular or parallel cylinders, other phases such as lamellar or perforated lamellar structures were observed in theoretical and experimental studies depending on the surface energies and the film thicknesses. To fully describe the intricate behaviour of the cylinder-forming systems (in this case, BCPs with 2:1 block volume fractions), a phase diagram was constructed to denote the phase transitions with respect to the surface energies (assuming both interfaces were identical) and the BCP film thickness (Figure 2.7).

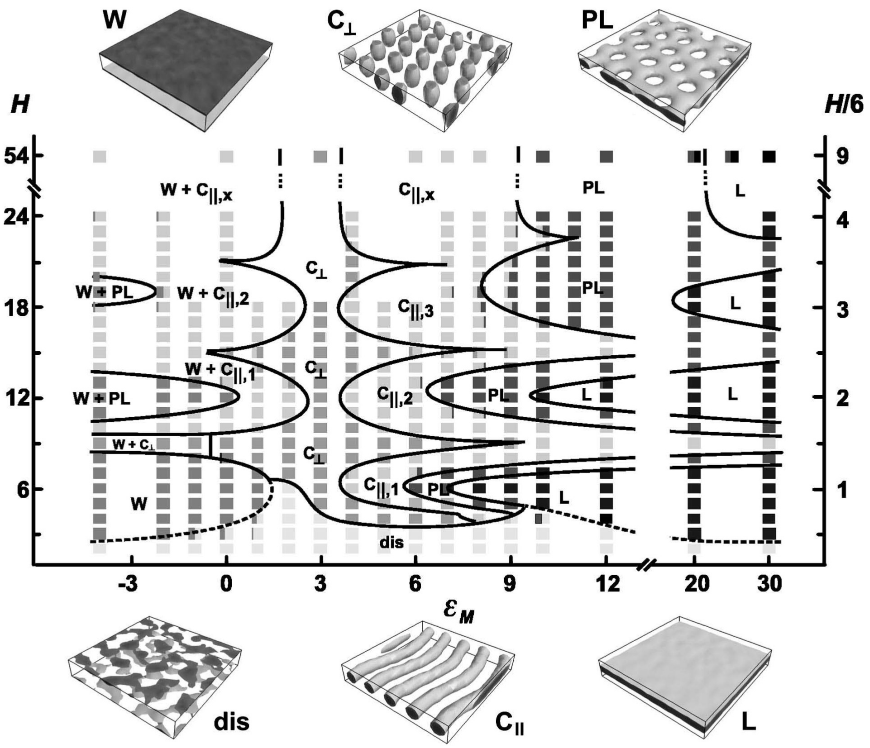

Figure 2.7: A phase diagram of BCPs with a 2:1 block ratio. The phases are highly dependent on the film thickness (H) and the surface energy (ε_M). Adapted with permission from ref. [28]. Copyright © 2004 AIP Publishing LLC.

As shown in the phase diagram, if the surface was selective for the minority block ($\varepsilon_M < 0$), wetting layers (W) were formed on the surfaces, and either planar lamellar (L) or parallel cylinders ($C_{\|}$) were observed within the middle film. As the surfaces became slightly selective for the majority block ($\varepsilon_M \sim 3$), perpendicular cylinders ($C_{\perp}$) began to be favoured. These structures then gave way to parallel cylinders, perforated lamellae (PL), and lamellae (L) as the surfaces became increasingly selective for the majority block ($\varepsilon_M > 0$). As the film thickness increased, parallel cylinders were observed more than their perpendicular equivalents at integer multiples of the cylinder layer thickness. Generally, films at these discrete thicknesses were also more energetically favourable, so during the self-assembly process, films not at these discrete thicknesses locally deformed to form regions with these discrete

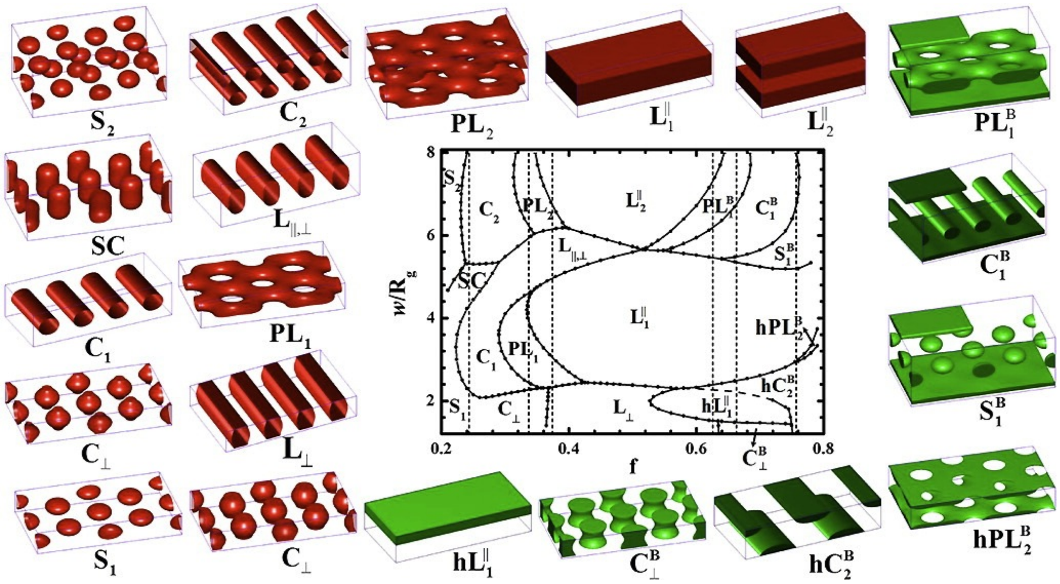

Figure 2.8: A phase diagram of BCPs as the film thickness and volume fraction of blocks varies. For ease in visualization the schematics displayed around the periphery show only the minority blocks in a red-green BCP. The surface energies are fixed and selective towards the green block. Reprinted with permission from ref. [31]. Copyright © 2013 American Chemical Society.

thicknesses.[29]

Recently, Li *et al.* used self-consistent field theory calculations to construct a phase diagram with respect to the film thickness and block volume fractions of a BCP (Figure 2.8).[31] In the calculations, $\chi N = 20$, and the surface was set to be selective for the block represented in green. The dotted lines in the phase diagram indicated the phase boundaries of a bulk BCP melt. The phase diagram clearly demonstrated the added complexity of the system due to the imposition of film thickness constraints. The use of these structures, especially the multilevel parallel cylinders in the C_2 phase, will be described in greater detail in Chapters 3 and 4.

2.3 Block Copolymer Ordering

As described in Chapter 1, significant interest has developed over the DSA of BCPs for next-generation semiconductor manufacturing. However, for DSA to become a viable manufacturing process, significant improvements must be made in the area of BCP structure ordering and defect control. Precise registration and orientation of both line or dot patterns templated by these films are necessary for proper alignment and connection with features patterned in subsequent layers. The ITRS stipulates that defect densities must be as low as <0.01 defects/cm^2 before DSA may be considered to be a manufacturing option. Additionally, the time required for BCPs to reach these low densities must also be less than 4 min to fit within the processing framework of the industry. The following section will first introduce parameters used in describing BCP order, and will then continue by describing various techniques that have been used in controlling the ordering process such as improving the self-assembly kinetics, introducing order-inducing fields, or modifying the surface or lateral confinement.

2.3.1 Correlation Lengths and Defect Densities

Two very common 2-dimensional nanopattern systems that are produced with BCP assembly are line or hexagonally-packed dot patterns. Line structures are observed when BCP lamellae align perpendicular to the substrate or when BCP cylinders align parallel to the substrate. Similarly, hexagonally-packed dots are observed when BCP cylinders align perpendicular to the substrate, or when BCP spheres are formed. Ideally, these systems have a high degree of translational and orientational invariance such that the self-assembly occurs in a simple and predictable manner. This invariance or order in the system is quantified by the translational and orientational correlation lengths, which describe the characteristic distance from an arbitrary point where the structure positions or orientation cease to correlate with those of the reference point. A large correlation length corresponds to an array of structures that approach the order observed in a perfect crystal. For an ideal line system, this corresponds to a parallel array of equally spaced linear lines, while for a dot array, this usually corresponds to a hexagonal array of dot patterns with perfect 6-fold symmetry.

In practical situations, however, defects are always present in the crystal structures of the patterns. These defects, which are disruptions in the overall structural arrangement, cause deviations from the perfect crystal arrangement of the patterns and manifest as either dislocations or disclinations.[32, 33] In the case of lamellar line patterns, at sufficiently low temperatures, the only defects observed are dislocations, which in line arrays, correspond to placement errors in the line structures (see Figure 2.9). Each dislocation is associated with a Burgers vector, which indicates the direction and magnitude of the lattice distortion. Dislocations themselves are usually generated from a perfect crystal structure as pairs with oppositely directed Burgers vectors. In the solid or crystalline phase, these dislocations are bound together to reduce the strain in the system. When sufficient energy is applied to the system, these dislocation pairs are allowed to unbind into individual dislocations, which transform the solid crystalline phase into what is known as a nematic phase (characterized by short-range translational order and quasi-long-range orientational order). As the temperature of the system is increased, more energy in the system allows more dislocations to accumulate in the 2-dimensional system. This continues until another transition known as the dislocation-dissociation transition is attained. At this transition, dislocations dissociate into new defects known as disclinations. In line arrays, disclinations appear in the positive variety (line terminations or dots) or in the negative variety (line junctions). A dislocation may be thought of as a tightly-bound pair of positive and negative disclinations, and as dislocations dissociate into disclinations, the strain on the system is increased and the orientational order of the system is decreased. The further separated a disclination pair is, the greater the distortion induced onto the lattice. The result is an isotropic phase characterized by short-range translational and short-range orientational order. The high defect density causes

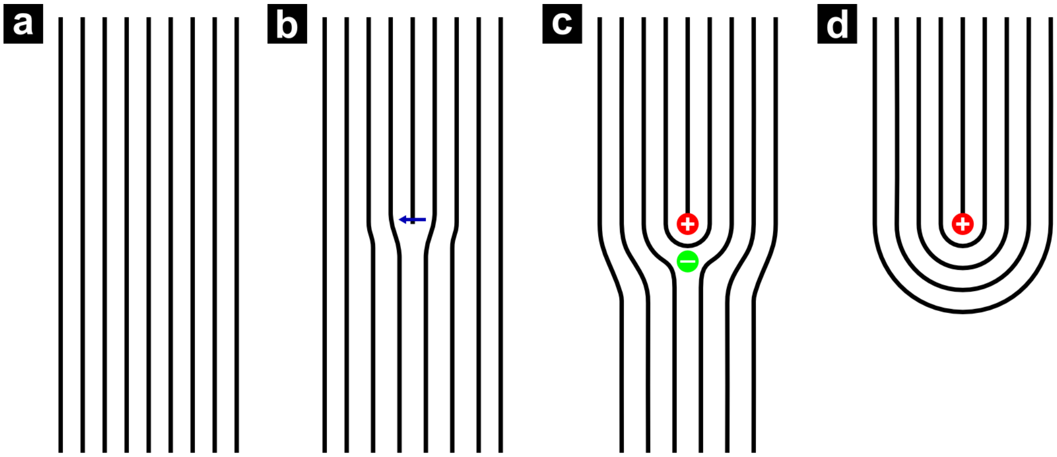

Figure 2.9: Schematics showing a perfect crystal (a), a dislocation (b), a dissociated disclination pair (c), and an individual disclination (d).

the line structures to resemble fingerprint patterns instead of a parallel array of straight lines.[34]

In hexagonally-packed dot patterns, analysis of these patterns are conducted through the use of Voronoi constructions, which takes the perpendicular bisectors of the connections between adjacent sites to construct a polygon to represent each site (see Figure 2.10). In a perfect crystal, all sites are represented by hexagons. Sites represented by 5 or 7-sided polygons are disclination defects. These disclinations pair up to form 5-7 dislocations, which can be eliminated by interacting with another 5-7 dislocation of the opposite direction. As with the line patterns, as the temperature is increased, an increased number of dislocation pairs are formed in the crystal structure. At the transition temperature where the dislocation pairs are separated, a hexatic phase is formed. With further increases in temperature, the disclinations themselves gain enough energy to separate, forming the final isotropic state.

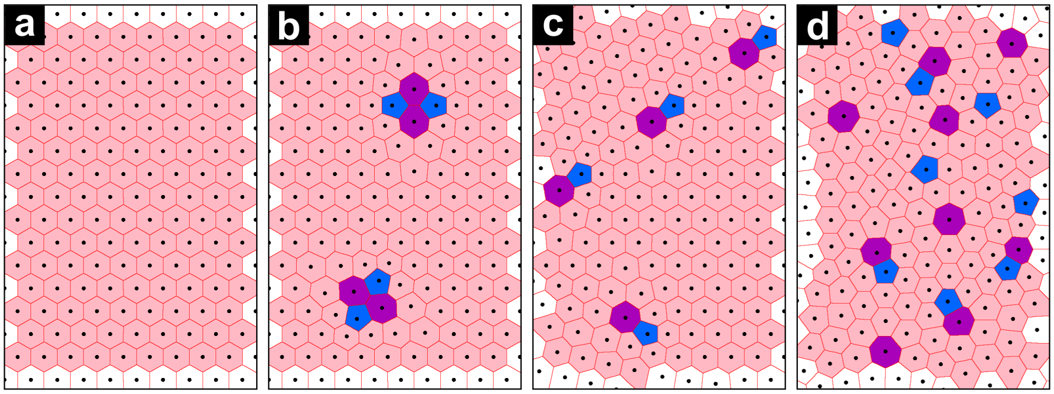

Figure 2.10: Schematics showing Voronoi constructions of a perfect crystal (a), a crystal with dislocation pairs (b), a hexatic phase with separated dislocations (c), and an isotropic phase with isolated disclinations (d). The hexagons are coloured pink, while the pentagon and heptagon defects are coloured blue and purple, respectively.

2.3.2 Reducing Defects By Increasing Mobility

One of the most critical factors determining the order in BCP self-assembly is polymer mobility. For BCP films to be useful in nanofabrication, the self-assembled domains in the films must be stable at room temperature, which dictates that at least one block component must have a T_g above room temperature. Thus, when these BCP films are rapidly deposited onto a substrate through spin casting, the polymer is kinetically trapped in a disordered state and is unable to self-assemble into the thermodynamically favoured configurations. To remediate this problem, polymer scientists have been implementing annealing steps to temporarily increase the mobility of the BCPs, allowing rearrangements into the lowest-energy configurations to occur. The oldest technique to be used for such purposes is thermal annealing, where BCP films are simply heated in a vacuum or inert atmosphere above the T_g of both blocks.[35, 36] As the temperature is raised above the T_g of both blocks, the polymer chains become significantly mobile, allowing self-assembly to occur faster.

While the kinetic limitations of the system are reduced with increased temperature, some thermodynamic limitations begin to manifest at higher temperatures. For example, studies on thermal annealing have shown that the equilibrium defect density of self-assembled nanostructures also increase with temperature.[37] Thus, although the same line or dot patterns may be observed, samples annealed at higher temperatures produce patterns with considerably lower lateral order than samples annealed at lower temperatures. As the temperature of the melts continue to increase, a notable thermodynamic feature characteristic of all BCP melts known as the order-disorder transition temperature (T_{ODT}) is encountered. Above T_{ODT}, which is dependent on the N, ϕ, and χ of the polymer, phase segregation fails to occur and a homogeneous mixture of the blocks is obtained.[38] This critical temperature may be determined using small-angle x-ray scattering (SAXS) measurements by observing the position and spread of diffraction peaks as the temperature is varied.[39] For high degrees of lateral ordering, some groups have first annealed their BCP films above the T_{ODT} because in this disordered state, the thermal history of the BCP is erased.[37, 40, 41] The films were then slowly quenched such that the polymer structures had time to reorganize into structures with lower defect densities at the lower temperatures. Besides the defect density limitations described above, another limitation to consider is the decomposition temperature of a BCP, above which the polymer chain begins to degrade.[42] Annealing must therefore always be conducted below the decomposition temperature, and in cases where the decomposition temperature is below the T_g, alternative approaches to increasing polymer mobility must be used.

Unlike thermal annealing, where the only two parameters in self-assembly affected by temperature are mobility and defect density, solvent annealing is a much more interesting and complex form of anneal that has the potential to affect the mobility of the BCP as well as the structure morphology and orientation. The basic premise of solvent annealing is to expose a BCP film to solvent vapour, which infiltrates and plasticizes the polymer film. This plasticization results in a lower T_g and increased polymer mobility to self-assemble into the thermodynamically favoured configurations.[43–45] Solvent annealing circumvents some of the limitations of thermal annealing and permits polymers with a T_g above the decomposition temperature to self-assemble as well. The effect solvent annealing has on mobility and structure morphology will be discussed in greater detail in Chapters 3 and 4.

While much work has been done to investigate the self-assembly behaviour of BCPs in the presence of different solvents, it was not until the late 1980s that some interesting effects of solvent evaporation from BCP thin films were noted. During that time, several groups observed that if solvents were allowed to evaporate from the BCP thin films immediately after the film casting process, perpendicular lamellar or cylindrical structures with non-equilibrium spacings were observed instead of the expected thermodynamically favoured parallel orientations driven by surface energy minimization.[9, 21, 46] Kim and Libera then found that by controlling the solvent evaporation process to be either faster or slower, both perpendicular and parallel structures could be produced in the respective conditions.[47, 48] The Russell group also discovered that during the solvent evaporation process, the ordered perpendicular structures propagated from the air/BCP interface down to the rest of the film.[49] This suggested that during solvent evaporation, a solvent concentration gradient was established within the film perpendicular to the substrate surface, which guided the growth of BCP structures along this gradient. This concentration gradient may have been small in slow evaporation steps, but for faster evaporation steps the solvent gradient became large enough to guide the self-assembly of BCP structures.[47] It should be noted at this point, however, that if the evaporation was too fast (<1 s), the BCPs did not have time to rearrange, and were thus kinetically trapped in their arrangements.[50, 51] Thus, one common way of performing solvent annealing was to place the BCP film inside a small chamber with a leak, and allow the solvent gradient in the slowly evaporating system to direct the assembly of the BCP. This approach was used successfully by several groups to create highly ordered BCP structures.[49, 52, 53]

While thermal and solvent annealing have both been shown to be effective strategies for increasing polymer mobility, a combination of the two methods

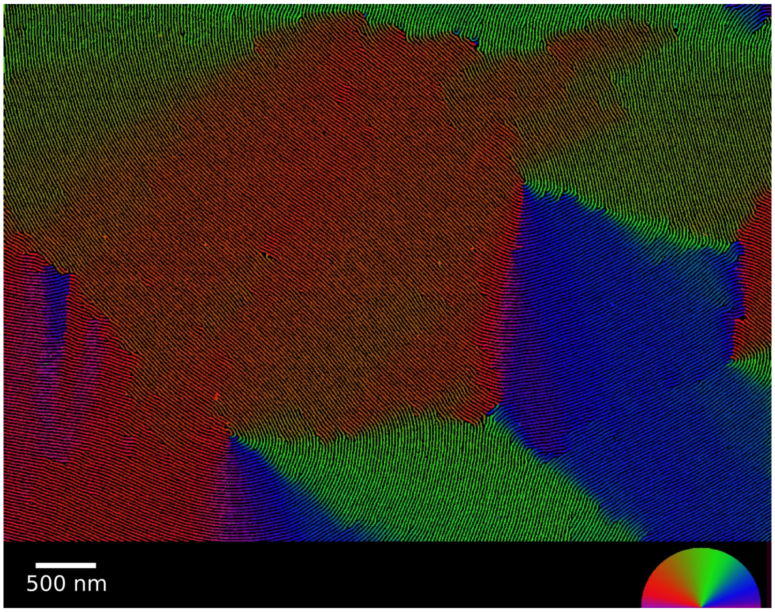

Figure 2.11: A low-magnification SEM demonstrating the high degree of BCP order induced by using the microwave-assisted annealing process for only 60 s. False colour was added to denote different line orientations. Reprinted with permission from ref. [54]. Copyright © 2010 American Chemical Society.

has potential to be even more effective. Recently, we developed a solvent-assisted microwave annealing technique to rapidly order the BCP structures.[54, 55] Films of cylinder-forming polystyrene-*b*-poly(2-vinylpyridine) (PS-*b*-P2VP) or PS-*b*-PMMA on silicon substrates were placed in a sealed chamber containing solvent and exposed to microwaves for times ranging from 2 s to 180 s (Figure 2.11). Ordering of these cylinder-forming BCPs occurred rapidly, and for one polymer, the defect density dropped below 2 defect pairs/μm^2 in a mere 60 s. The work has been replicated by others to create ordered polystyrene-*b*-poly(dimethyl siloxane) (PS-*b*-PDMS) line patterns.[56] Recently, Jung *et al.* also demonstrated another method of solvent-thermal annealing by adding a heating source to a solvent anneal chamber and showed that high degrees of lateral order could be obtained at temperatures below 100 °C.[57]

2.3.3 Controlling Orientation Through External Fields

Increasing the polymer mobility reduces the kinetic limitations on the self-assembly process, allowing structures with lower defect densities to be produced. However, the mobility has no influence over the orientation of the BCP structures. For control over the orientation, the use of external fields has been shown to effectively guide the self-assembly along a preferential direction. Various types of fields have been used including shear forces, temperature gradients, electrical fields, or even the solvent concentration gradients observed during solvent annealing as described above.

One heavily studied area is the use of various shear fields to direct the assembly of BCP lamellar, cylinder, or spherical structures. Shear fields produced from various types of rheometers may be generated by sandwiching BCP films between two heated plates with PDMS rubber pads or viscous PDMS oil to prevent film rupture. These plates then apply pressure on the film and are laterally displaced with respect to each other to generate shear stress in the lateral direction. The shear coordinates with shear ($\vec{v}$), gradient ($\vec{\nabla}$), and vorticity ($\vec{e} = \vec{v} \times \vec{\nabla}$) basis vectors may be defined as shown in Figure 2.12. Depending on the shear fields applied to the polymers, the temperatures of the films, and the block compositions, the microdomains will align along one of these coordinate axes to minimize the stress in the system.

For structure alignment to occur, the BCPs are usually heated to an elevated temperature between T_g and the T_{ODT}, and different shear treatments (steady or oscillating) with different shear rates may be applied for different effects. It is important to note, however, that the T_{ODT} varies with shear rate.[58] Under an oscillating shear, lamellar domains most often align with their surface normals parallel to the vorticity axis. However, under special conditions when the frequency of oscillations exceed a critical frequency (ω_d) at temperatures close to T_{ODT}, domains with surface normals aligned to the gradient axis are favoured instead.[59] Angelescu *et al.* found that with a large enough shear rate, it was also possible to align cylindrical structures along the shear

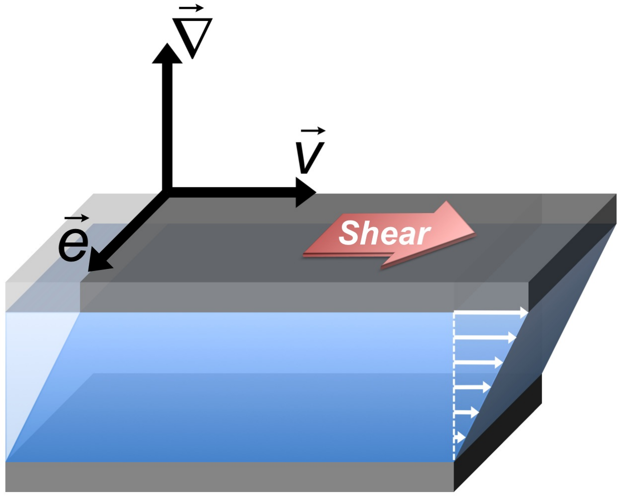

Figure 2.12: When a shear force is applied to a BCP film, a set of coordinates with shear ($\vec{v}$), gradient ($\vec{\nabla}$), and vorticity($\vec{e}$) axes may be defined to describe the orientation of BCP domains.

axis.[60] While films with monolayer spheres cannot be aligned due to a lack of mechanical anisotropy, it was possible to induce high lateral order in bilayers of spheres.[61] This method is quite flexible and may easily accommodate lateral ordering on larger substrates. The method has also been shown to be successful in roll-casting techniques, which may provide a viable route towards large-scale manufacturability.[62, 63]

Similar to the solvent gradients described in the previous section, temperature gradients have also been found to direct the assembly of BCPs. This concept was first explored by Hashimoto *et al.* who employed a moving temperature gradient field laterally across a film surface.[64] The device, which is now known as a zone-heating device consisted of a hot bar with temperature above the polymer T_{ODT} surrounded by gradually cooler regions. By passing the lamellar BCP films through the zone-heating device, ordered lamellar domains grew from the disordered phase along the ordering front, and were aligned with the lamellar planes perpendicular to the direction of the moving temperature gradient.[64, 65] Zone heating may also be applied to cylindrical structures to radically reduce defect densities. In a study where zone heating was applied at temperatures below the T_{ODT}, the cylinder structures were still found to preferentially orient with their long axis along the temperature gradient.[66] The process was found to be faster and more effective at producing lines with high lateral order than conventional thermal anneals. Investigations into oscillating temperature gradients also revealed that defects in lateral cylindrical structures could be reduced further, although it was also noted in this experiment that the cylinder orientation did not correlate with the direction of the temperature gradient.[67] Besides oscillating temperature gradients, very sharp spatial temperature gradients could also be used to form vertically-aligned cylinder structures.[68] Thus, zone annealing has great potential to be used in the large-scale manufacturing of polymer nanostructures through roll-to-roll processing.[69]

When a contrast between the dielectric constants of the two blocks exists, local variations in the dielectric constant may be coupled to an externally applied electric field to direct the orientation of BCP patterns. Alignment of BCPs using electric fields was first explored in seminal work by Amundson *et al.*[70–72] In these experiments, 1.8 V/µm electric fields applied to cooling PS-*b*-PMMA polymers as they crossed the T_{ODT} were shown to direct the growth of lamellar structures perpendicular to the electrode surfaces. The authors also explored the kinetics and defect annihilation mechanisms for lamellae realignment in an electric field at temperatures below the T_{ODT}. Electric fields were later demonstrated by Morkved *et al.* to direct the alignment of cylinder-forming BCPs parallel to the substrate surface (see Figure 2.13).[73] When a 3.7 V/µm electric field ($\vec{E}$) was applied between the pre-patterned planar electrodes on the substrate surface, the cylinders aligned themselves with their long axes parallel to the field lines of the electrodes. The correlation of cylinder orientation to the field lines was found to be directly related to the calculated field strength at the region. Thus, for regions further from the electrodes, defects in the cylinder alignment became more prominent. Electric fields could also be applied perpendicular to the substrate surface but in such cases, stronger fields were required to overcome the interfacial surface energy effects.[74–76] To produce perpendicular cylinders, the BCP films were sandwiched between

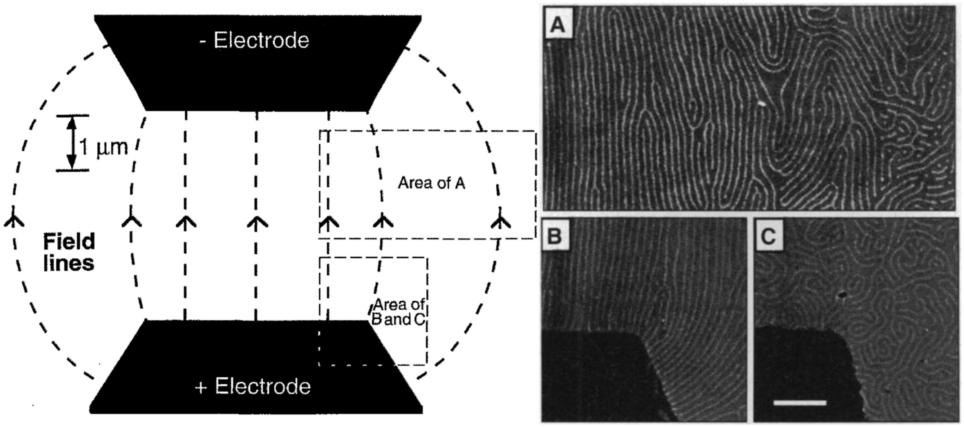

Figure 2.13: Transmission electron microscope (TEM) images of cylindrical BCP domains between 2 planar electrodes. The ordering of BCPs halfway between the electrodes decreases as $\vec{E}$ drops off from left to right (a). Cylinders align along the field lines at the electrode when $\vec{E}$ is on (b), and become randomly oriented when $\vec{E}$ is off (c). Scale bar is 500 nm. Adapted with permission from ref. [73]. Copyright © 1996 AAAS.

two electrodes with Kapton films at each interface of the BCP film. Field strengths greater than 11.5 V/µm were required to completely overcome the surface energy effects to produce purely perpendicular cylinder patterns.

Since these initial investigations, studies have shown that for electric fields perpendicular to the substrate surface, a competition between surface effects and the electric field result, and an electric field must exceed the value E_c as described in Equation 2.3.1 for structures to be completely perpendicular to the substrate surface.[77, 78] $\Delta\gamma$ is the difference in surface energy between the two blocks, ϵ_A and ϵ_B are the permittivities of the two blocks, and h is the film thickness. Thus, if the surface energy difference is too large or if the film is thin, E_c is larger than the dielectric breakdown and perpendicular alignment is not possible. However, if no surface energy differences exist, then no electric field is required for perpendicular structures.

$$E_c \;=\; \Delta\gamma^{1/2}\frac{2(\epsilon_A+\epsilon_B)^{1/2}}{\epsilon_A-\epsilon_B}h^{-1/2} \tag{2.3.1}$$

One problem with electric field alignment of lamellar structures is that the aligned lamellae are free to rotate about the electric field lines to form multiple orientations. This extra degree of freedom may be limited through the application of another field. For example, Olszowka *et al.* combined a solvent field (perpendicular to substrate surface) through solvent annealing in toluene, with electric fields from planar electrodes (parallel to substrate surface) to produce highly ordered perpendicular lamellar patterns.[79]

2.3.4 Graphoepitaxy and Chemical Epitaxy

By controlling the polymer mobility and applying a guiding external field during the self-assembly process, highly ordered BCP features with a predetermined orientation can be formed. However, in patterning applications for the semiconductor industry, slightly more complex patterns with locally varying orientations are often desired. While it may be difficult to produce these small local variations using an external field, techniques that make use of lateral film confinement and locally varying surface chemistry more adeptly produce these types of patterns. These techniques are the subject of discussion below.

Graphoepitaxy

Just as the confinement of a BCP film in one dimension results in the creation of a new parameter of control over the self-assembly, confinement in the lateral dimensions using topographical features from the underlying substrate also allows for additional control over the self-assembly of the films. The use of these surface features (usually produced through top-down approaches such as photolithography, interference lithography, or EBL) to direct the assembly of

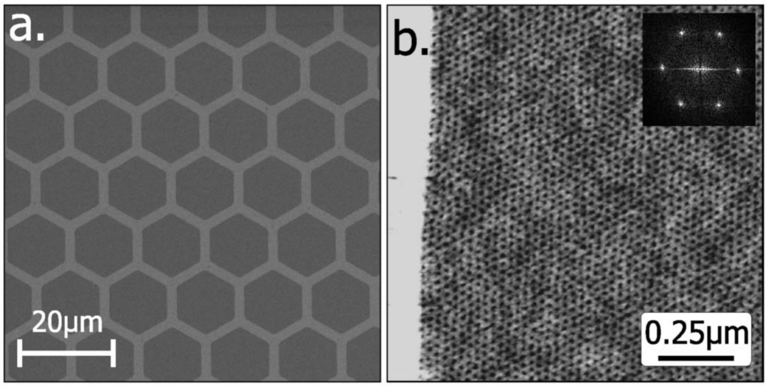

Figure 2.14: (a) Hexagonal wells were patterned using photolithography, as shown in the SEM image. (b) Single-crystal dot patterns were then self-assembled within the wells, as shown in the atomic force microscope (AFM) image and the fast Fourier transform (FFT) in the inset. Reprinted with permission from ref. [83]. Copyright © 2007 The American Physical Society.

BCP films is known as graphoepitaxy.

The lithographically patterned features most commonly used in the graphoepitaxy of both BCP lines and dots are micron-sized trenches or wells.[37, 80–84] In these studies, as the disordered BCP films were annealed, single crystals of the BCP nanostructures began to nucleate at the walls of these trenches and slowly propagated to the centre.[85] The ordering effects were observed not only in narrow trenches, but also in trenches up to several microns in width. In one instance, extremely large single crystals of BCP dot patterns were created using 12 μm-wide hexagonal wells (see Figure 2.14). Beyond these dimensions, however, these single crystals of spheres or lines start to exhibit increasing numbers of defects until the order breaks down at sufficiently large distances from the walls.

Besides the single-crystal nanopatterns, wells of various shapes could also be used to guide the assembly of more complex patterns. For example, circular wells were used to coax cylinder-forming BCPs into assembling concentric rings or spiral patterns (see Figure 2.15).[86, 87] Lamellar-forming BCPs were also shown to form concentric hexagons or densely-packed angled lines through the

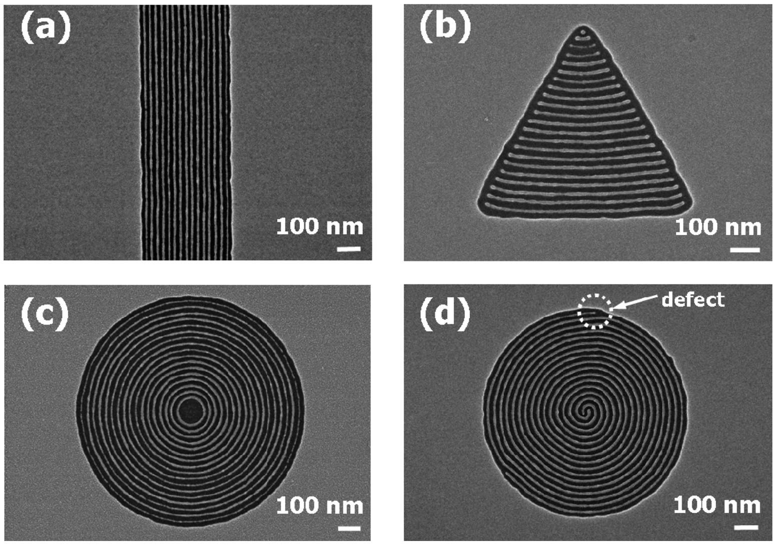

Figure 2.15: Cylindrical BCP patterns may self-assemble to form parallel lines along a trench (a), parallel lines inside triangular wells (b), concentric rings inside a circular well (c), or spiral patterns inside a circular well with defects (d). Reprinted with permission from ref. [87]. Copyright © 2008 American Chemical Society.

guidance of walls written by EBL.[88]

One disadvantage of using wells or trenches for graphoepitaxy is that the walls often take up precious substrate real estate, which decreases the number of patternable elements on the surface. This is an especially important consideration for applications in the semiconductor industry, where the goal is to pack as many devices onto a substrate as possible. A method of graphoepitaxy that minimizes this problem is the use of silica posts patterned by EBL.[89–91] By tuning the spacings, shape, and surface chemistry of these silica posts, the ordering and orientation of BCP dot and line patterns may be independently controlled to create locally varying patterns (see Figure 2.16). Recently, it was shown that silica posts could also be used to direct the formation of cross-hatched line patterns from bilayer cylinder-forming BCPs.[91] The one limitation of this method of graphoepitaxy is its heavy reliance on densely-packed pre-patterned features.

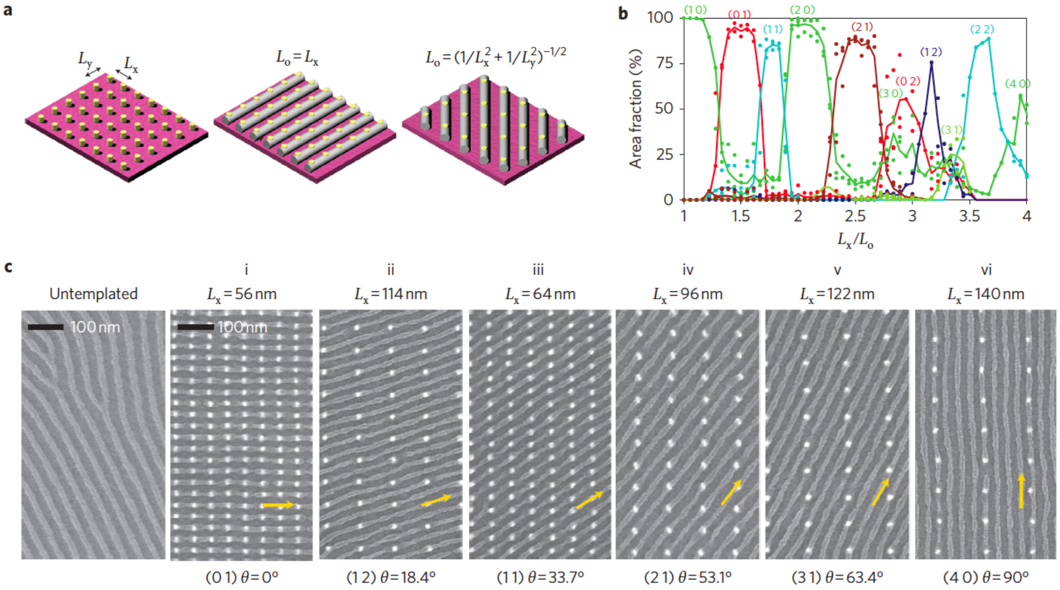

Figure 2.16: (a) A schematic depicting how the spacings in rectangular arrays of posts affect the alignment of cylindrical line patterns. (b) A chart displaying the area fraction of lines with different orientations as L_x/L_y was increased. (c) SEM images of lines aligned along different different directions as the post spacings are varied ($L_x = 1.5L_y$). Reprinted by permission from Macmillan Publishers Ltd: Nature Nanotechnology,[90] copyright © 2010.

Chemical Epitaxy

Besides using lateral confinement to control the assembly of the BCP, another method is to exploit BCP surface energy effects. In the thermodynamic studies described above, the surface energies at the air/BCP and BCP/substrate interfaces were constant in the lateral direction. If instead, the surface energies were allowed to vary in the lateral directions, these lateral variations may be used to guide the self-assembly of BCPs. Seminal work in this area was first conducted by Heier *et al.*, who created micron-sized chemical patterns on a flat gold surface with self-assembled monolayers.[92, 93] Patterned areas with CH_3-terminated groups were first deposited through micro-contact printing, and the unmodified areas were subsequently covered by OH-terminated thiols. Polymer films deposited on these patterned regions formed parallel structures

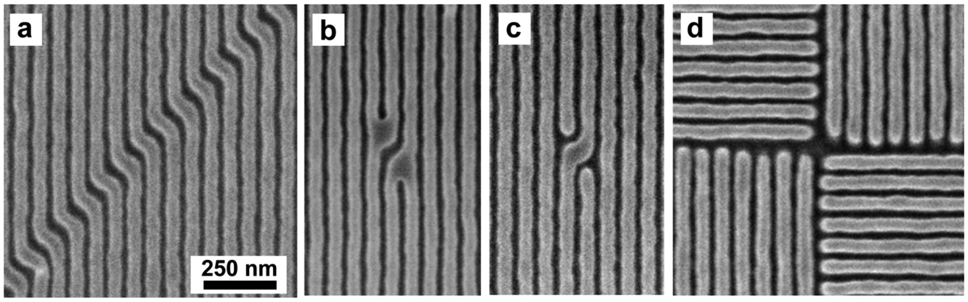

Figure 2.17: BCP structures may be directed to self-assemble into different patterns useful for nanoelectronic fabrication. For example, nested jogs (a), isolated jogs (b,c), and T-junctions (d) may be formed as shown in the SEMs. Reprinted with permission from ref. [96]. Copyright © 2007 American Chemical Society.

over the OH regions and perpendicular structures over the CH_3-terminated regions due to differences in the block selectivity of the surface. Since that time, investigations by other groups have confirmed that surface chemical patterns with similar periodicities as the BCPs cause the BCPs to assemble forming the same pattern. Notable work in this area by the Nealey group demonstrated that not only will BCPs align along simple regular chemical patterns such as lines or dots, but they will also self-assemble to imitate the more complex underlying chemical patterns. As a result, these self-assembled patterns may be used for the patterning of different circuit elements in microelectronic fabrication, such as junctions, jogs, single lines, and angled lines (see Figure 2.17).[94–96]

While the resulting patterns impressively self-assemble to resemble the underlying chemical patterns, this alone does not make the DSA of BCPs ideal for nanoelectronic fabrication, because chemical patterns with the same pitch and dimensions must be patterned on the substrate first. To address this concern, work has been done to use sparser pre-patterns to direct the assembly of BCP structures. So far, chemical patterns with half, a third, or a quarter of the BCP feature density have been shown to be effective in directing the assembly of BCP features with low defect densities.[97–99] Figure 2.18 is a good example demonstrating how BCPs may be used to quadruple the density and improve

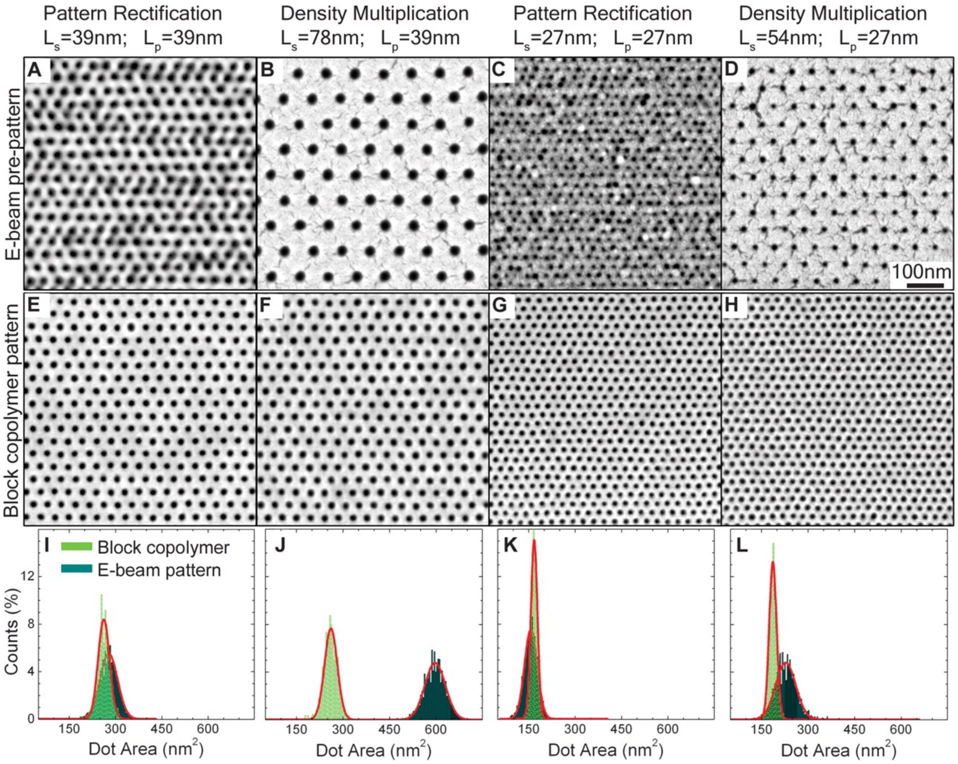

Figure 2.18: Samples of EBL resist were first patterned to form dots with spacings $L_s = 39, 78, 27, 54$ nm (a-d). These chemical pre-patterns were then used to direct the assembly of BCP films with pitches $L_p = 39, 39, 27, 27$ nm, respectively (e-h). The size distribution of both EBL and BCP patterns were then compared (i-l). Reprinted with permission from ref. [97]. Copyright © 2008 AAAS.

the overall consistency and quality of dots patterned by EBL.

2.4 Nanostructure Fabrication

The self-assembly process produces many domains within the BCP films. However, for BCPs to be used in nanostructure fabrication, a process to transform these phase-separated domains into real free-standing nanostructures is required. Several different methods have been developed and used over time, and will be described below.

2.4.1 Block Copolymers for Precursor Localization

BCP micelles have been used in the past as solution-based nanoreactors for the synthesis and stabilization of metal, metal oxide, and metal chalcogenide nanoparticles.[100] Differences in the block solubilities in solution caused the BCPs to form micelles with non-soluble blocks at the core, and soluble blocks at the corona. When the BCPs were chosen such that the core blocks contained functional groups for binding specific metal precursors, these micelle cores became localized sites for the precursors to react. The result was the formation of nanoparticles made of Au, Co, Pd, Fe_2O_3, or CdS, just to name a few.[101–105] Common blocks for the micelle core included P2VP, poly(4-vinylpyridine) (P4VP), or poly(acrylic acid) (PAA), while in aqueous solutions, a common block used for the corona was poly(ethylene oxide) (PEO). This strategy, which was proven successful when used for BCP micelles, could also be applied to self-assembled BCP films.

Two strategies have historically been used to localize solution-based metal precursors within a BCP film: the precursors have either been preloaded into BCP micelles prior to film deposition onto the substrate,[104, 106] or they have been allowed to infiltrate the BCP film through an immersion step after film deposition.[87, 107, 108] Using both of these methods, Aizawa and Buriak produced quasi-hexagonal dot arrays of Au and Ag nanoparticles templated by PS-*b*-P4VP.[107] Au and Ag metal salts were reduced through galvanic displacement with the semiconductor substrate (Si, Ge, InP, and GaAs). To enable electrical contact between the metal and the substrate on Si surfaces, dilute HF was also added to the metal salt solutions to remove the insulating native oxide. The polymer was then removed through ultrasonication. Chai and Buriak were able to extend the utility of this method to cylindrical structures as well (see Figure 2.19).[87, 108] The method was also generalized to include the formation of metal structures such as Pt, Pd, Co, Cu, and Fe. Through conducting AFM, they were able to confirm that these nanowires were indeed solid and continuous metal.

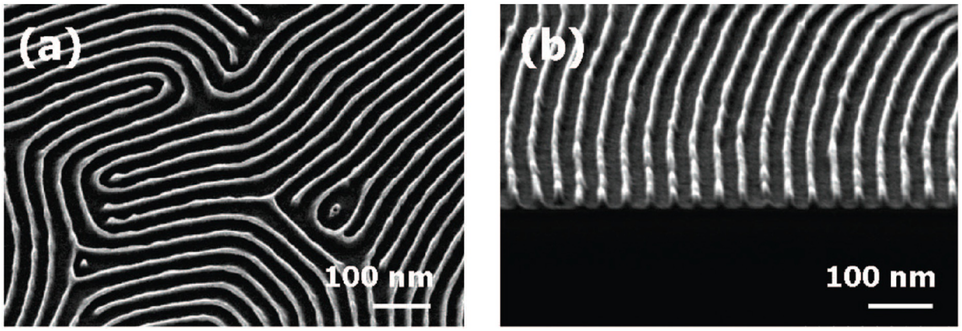

Figure 2.19: Top (a) and tilted (b) SEM images of PS-*b*-P2VP cylinders metallized with Pt and treated with plasma. Reprinted with permission from ref. [87]. Copyright © 2008 American Chemical Society.

Besides solution-based precursors, vapour-phase precursors have also been used to synthesize nanostructured materials. For example, by exposing PS-*b*-PMMA films to tetraethyl orthosilicate (TEOS) and HCl vapour, silica structures that resembled the patterns of the BCP film were created by one group.[109] However, these vapour-phase reactions did not seem to produce very uniform structures. One recently developed method that has produced better results in fabricating metal or metal oxide nanostructures is sequential infiltration synthesis (SIS).[110, 111] As the name suggests the process involves sequentially exposing PS-*b*-PMMA films to different precursor gases. These precursors infiltrate the PS-*b*-PMMA films and react specifically to the carbonyl bonds in the PMMA regions. After a quick purge, the films are exposed to the second precursor gas, which reacts with the first precursors to form metal or metal oxides within the PMMA regions. Through repeated steps, these metal or metal oxides grow to form nanolines or nanodots that resemble the PMMA domains within the BCP film. The method is very similar to the atomic layer deposition (ALD) technique, and may often be performed within ALD machines, but the precursor pressures and step times are much larger and longer than conventional ALD steps.[112] For example, Al_2O_3 structures could be created by alternating between $Al(CH_3)_3$ and H_2O; while TiO_2 structures could be created by alternating between $TiCl_4$ and H_2O.[110] Materials that were more difficult to pattern due to a lack of selective chemistry for

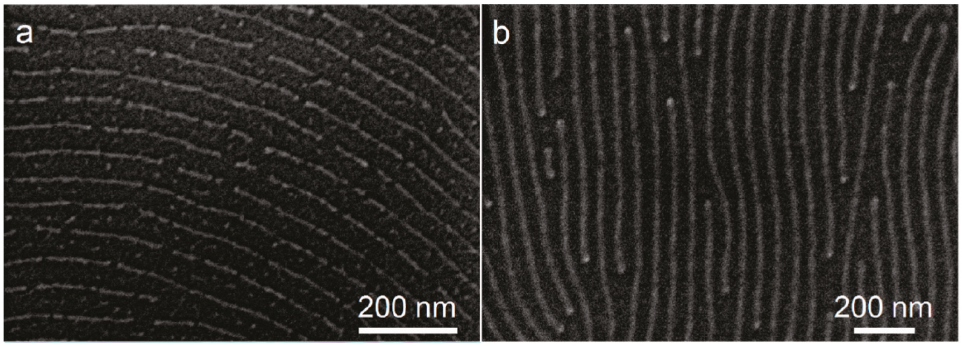

Figure 2.20: SEMs of Al_2O_3 (a) and ZnO (b) line structures templated using cylinder-forming BCPs and the SIS approach. Reprinted with permission from ref. [111]. Copyright © 2011 American Chemical Society.

PS-*b*-PMMA or difficulties in control could be fabricated by first running a few cycles of $Al(CH_3)_3$. The presence of Al was then used to facilitate the fabrication of ZnO, SiO_2, or even W structures (see Figure 2.20).[111] Because the SIS process is self-limiting in nature, highly flexible in precursor choice, and highly controllable due to the cyclic nature, the process offers a great deal of control over structure formation.

Besides directing the growth of new structures, BCP films can also guide the etching of substrates in specific locations. For example, when self-assembled quasi-hexagonal PS-*b*-P4VP films on silicon substrates were immersed in dilute HF or NH_4F solutions, it was demonstrated that the BCP film directed silicon etching only in areas where P4VP blocks were present.[113] The P4VP blocks contained pyridyl groups that acted as Brönsted bases, which directed the etching of quasi-hexagonal pits with hydride terminated surfaces. Unetched surfaces remained hydroxy-terminated. Differences in termination allowed for the pit surfaces or the substrate surfaces to be independently altered with organosilanes, which could then direct the growth of titania or gold nanostructures.[114]

2.4.2 Block Copolymer Films as Masks

Another class of methods for creating nanostructures is to use the BCP film as a protective mask layer for an underlying substrate. In such a process, the BCP film is first deposited above a thin film of the material to be patterned. After the self-assembly process has produced the desired pattern in the BCP film, the film is then subjected to an etch step to selectively remove one of the blocks and leave specific regions in the underlying material layer exposed. One of the most common BCP etching methods is to use O_2 plasma to selectively remove one block. For example, O_2 plasma was applied to PS-*b*-PMMA to create a PS mask for etching silicon nanowires.[115] O_2 plasma, however, is only slightly selective for PMMA, and so a significant portion of PS is also removed during the process. For higher etch selectivity, other polymers such as PS-*b*-PDMS or polystyrene-*b*-polyferrocenylsilane (PS-*b*-PFS) could also be used.[116, 117] The presence of silicon or iron in the PDMS or PFS blocks makes these blocks much more resistant to O_2 plasma etching, which allows for better, more well-defined mask layers.

Besides using polymers with higher etch selectivity, other approaches to modify the film to increase etch selectivity may also be used. For example, treatment of PS-*b*-PMMA films with UV light leads to cross-linking in PS blocks, and scission of bonds within PMMA blocks.[75] After subsequent immersion in acetic acid solution, the PMMA blocks are dissolved away, leaving a free-standing PS mask. In dot-forming PS-*b*-PB and PS-*b*-PI films, one of two treatments may be used to produce either positive or negative masks.[118, 119] By exposing the BCP films to ozone atmosphere, scission of the carbon double bonds in PB or PI blocks allows these segments to be dissolved away in deionized water, leaving behind a nanoporous cross-linked PS mask. The reverse of this pattern may also be produced if instead of ozone exposure, the films are exposed to the heavy metal stain OsO_4. The OsO_4 stain increases the etch resistance of the PB or PI blocks, allowing the production of a hexagonally-packed nanodot mask when the film is subsequently treated with CF_4 plasma. Other approaches such as SIS may also be used to drastically enhance the etch resistance of one block over another. These can then be used as masks for underlying materials such as silicon, indium tin oxide (ITO), or permalloy ($Ni_{0.8}Fe_{0.2}$).[120] It has also been demonstrated that in PS-based polymers with perpendicular PMMA, PEO, P2VP or P4VP cylindrical domains, the introduction of a solvent strongly selective for the cylinder blocks (such as acetone or ethanol) encouraged slight restructuring of the films to form hexagonally-packed nanoporous films without the need for etching.[121, 122]

Once the polymer mask is complete, selected areas of the underlying substrate become exposed to the surrounding environment, and these exposed surfaces can either be etched away or be used as nucleation centres for nanostructure growth. In the former case, the mask material must be carefully selected to be resistant to the etch process. Sometimes, the mask is robust enough to allow direct patterning of the underlying substrate material,[115, 118, 120] but in other cases, the material to be patterned requires an etch that also destroys the BCP mask. In those cases, one or two intermediate layers are required for the patterns to fully transfer onto the material layer. For example, to pattern cobalt magnetic dot arrays, one group used a PS-*b*-PFS film above layers of silicon dioxide, tungsten, and cobalt.[116, 123] Because cobalt, nickel, and iron cannot be etched by a reactive ion etch (RIE) due to a lack of volatile products, ion beam etching must be used instead. Thus, a tungsten layer was added to act as a hard mask for the ion beam etching process. Silicon dioxide was included on top of the tungsten to improve the pattern transfer from the PS-*b*-PFS polymer to tungsten. A CHF_3 plasma was used to transfer the BCP mask pattern onto the SiO_2 film. A CF_4 and O_2 plasma mixture was then applied to transfer the SiO_2 pattern onto the W film. Finally, the W mask was used as a hard mask for Co etching using an ion beam.

BCP masks may also be used to limit interactions of a substrate surface with chemical precursors during nanostructure synthesis. For example, by using masks formed from PS-*b*-PMMA to expose only specific areas on a surface, SiO_2 posts may be grown with the introduction of vapour-phase precursors such as $SiCl_4$ or TEOS.[109, 124] A subsequent CF_4 plasma or calcination step may then be used to remove the BCP film. Similar masks have also been used to form GeSbSe phase-change nanomaterials from solution-phase GeSe and Sb_2Se_3 precursors dissolved in hydrazine.[125] In these experiments, the mask and extraneous GeSbSe were removed through a subsequent lift-off process by ultrasonication in toluene. As in the case with etching, sometimes a mask more robust than the BCP film is required for growth. One such example was the growth of GaAs quantum dots on a GaAs substrate.[126] In this example, a PS-*b*-PI BCP film was used to pattern a SiN_x film to create a hard mask for the underlying GaAs substrate. Once the BCP pattern was transferred to the underlying SiN_x mask, arsine and triethylgallium vapour, which reacted only at exposed GaAs surfaces, was used to grow GaAs quantum dots on the GaAs surface. The SiN_x mask was then removed with buffered oxide etchant.

2.5 Conclusions

In summary, the self-assembly of diBCP melts are governed by the thermodynamics of phase separation between the two distinct blocks. The driving force behind phase separation increases with χN and the BCP domain morphology is determined by the block volume fraction. These BCP melts may also be deposited as thin films on substrates, and in such cases, the melt confinement and the introduction of surface interfaces allow more complex morphologies to be produced. However, for self-assembled BCP films to be of use in semiconductor manufacturing, the domains must be highly ordered and tightly controlled. This may be done through increasing the BCP mobility, introducing external fields to direct the orientation of self-assembled domains, or utilizing pre-patterned surface topography and surface chemistry. Once ordered, the BCP domains must then be transformed into free-standing nanostructures. In general, BCP films may either be used as templates to direct the formation of nanostructures through the localization of solution-phase or vapour-phase precursors, or they may be used as masks to block the etching or growth of an underlying film into free-standing nanostructures.

References

[1] C. E. Carraher, *Introduction to Polymer Chemistry*, 2nd ed. Boca Raton, FL: CRC Press, 2010.

[2] D. van Krevelen and K. te Nijenhuis, *Properties of Polymers*, 4th ed. Oxford, UK: Elsevier, 2009.

[3] P. J. Flory, *Principles of Polymer Chemistry.* Menasha, WI: George Banta Publishing Co., 1953.

[4] J. Mark, *Physical Properties of Polymers Handbook*, 2nd ed. New York, NY: Springer, 2007.

[5] K. E. Kear, *Developments in Thermoplastic Elastomers.* Shropshire, UK: Rapra Technology Limited, 2003.

[6] R. Robotti, “TPEs in automotive applications,” in *Thermoplastic Elastomers: Processing for Performance.* Shropshire, UK: Rapra Technology Ltd., 1989, vol. 2.

[7] E. Helfand, “Block copolymers, polymer-polymer interfaces, and the theory of inhomogeneous polymers,” *Accounts of Chemical Research*, vol. 8, no. 9, pp. 295–299, 1975.

[8] T. L. Morkved *et al.*, “Mesoscopic self-assembly of gold islands on diblock-copolymer films,” *Applied Physics Letters*, vol. 64, no. 4, pp. 422–424, 1994.

[9] P. Mansky, P. M. Chaikin, and E. L. Thomas, “Monolayer films of diblock copolymer microdomains for nanolithographic applications,” *Journal of Materials Science*, vol. 30, no. 8, pp. 1987–1992, 1995.

[10] P. J. Flory, “Thermodynamics of high polymer solutions,” *The Journal of Chemical Physics*, vol. 10, no. 1, pp. 51–61, 1942.

[11] M. L. Huggins, "Some properties of solutions of long-chain compounds," *Journal of Physical Chemistry*, vol. 46, no. 1, pp. 151–158, 1942.

[12] L. M. Robeson, *Polymer Blends: A Comprehensive Review.* Munich, Germany: Carl Hanser Verlag, 2007.

[13] F. S. Bates and G. H. Fredrickson, "Block copolymer thermodynamics — Theory and experiment," *Annual Review of Physical Chemistry*, vol. 41, pp. 525–557, 1990.

[14] F. S. Bates, "Polymer-polymer phase behavior," *Science*, vol. 251, no. 4996, pp. 898–905, 1991.

[15] E. Helfand and Z. R. Wasserman, "Microdomain structure and the interface in block copolymers," in *Developments in Block Copolymers*, I. Goodman, Ed. New York, NY: Applied Science, 1982, vol. 1, pp. 99–125.

[16] A. N. Semenov, "Contribution to the theory of microphase layering in block-copolymer melts," *Soviet Physics JETP*, vol. 61, no. 4, pp. 733–742, 1985.

[17] L. Leibler, "Theory of microphase separation in block copolymers," *Macromolecules*, vol. 13, no. 6, pp. 1602–1617, 1980.

[18] M. W. Matsen and F. S. Bates, "Unifying weak- and strong-segregation block copolymer theories," *Macromolecules*, vol. 29, no. 4, pp. 1091–1098, 1996.

[19] F. S. Bates and G. H. Fredrickson, "Block copolymers — Designer soft materials," *Physics Today*, vol. 52, no. 2, pp. 32–38, 1999.

[20] G. Coulon *et al.*, "Surface-induced orientation of symmetric, diblock copolymers: A secondary ion mass-spectrometry study," *Macromolecules*, vol. 22, no. 6, pp. 2581–2589, 1989.

[21] T. P. Russell *et al.*, "Characteristics of the surface-induced orientation for symmetric diblock PS/PMMA copolymers," *Macromolecules*, vol. 22, no. 12, pp. 4600–4606, 1989.

[22] P. Mansky *et al.*, "Controlling polymer-surface interactions with random copolymer brushes," *Science*, vol. 275, no. 5305, pp. 1458–1460, 1997.

[23] P. Mansky *et al.*, “Interfacial segregation in disordered block copolymers: Effect of tunable surface potentials,” *Physical Review Letters*, vol. 79, no. 2, pp. 237–240, 1997.

[24] P. Mansky *et al.*, “Ordered diblock copolymer films on random copolymer brushes,” *Macromolecules*, vol. 30, no. 22, pp. 6810–6813, 1997.

[25] E. Huang *et al.*, “Using surface active random copolymers to control the domain orientation in diblock copolymer thin films,” *Macromolecules*, vol. 31, no. 22, pp. 7641–7650, 1998.

[26] E. Huang *et al.*, “Neutrality conditions for block copolymer systems on random copolymer brush surfaces,” *Macromolecules*, vol. 32, no. 16, pp. 5299–5303, 1999.

[27] C. M. Bates *et al.*, “Polarity-switching top coats enable orientation of sub-10-nm block copolymer domains,” *Science*, vol. 338, no. 6108, pp. 775–779, 2012.

[28] A. Horvat *et al.*, “Phase behavior in thin films of cylinder-forming ABA block copolymers: Mesoscale modeling.” *The Journal of Chemical Physics*, vol. 120, no. 2, pp. 1117–1126, 2004.

[29] H. P. Huinink *et al.*, “Asymmetric block copolymers confined in a thin film,” *The Journal of Chemical Physics*, vol. 112, no. 5, pp. 2452–2462, 2000.

[30] A. Knoll *et al.*, “Phase behavior in thin films of cylinder-forming block copolymers,” *Physical Review Letters*, vol. 89, no. 3, pp. 35 501(1–4), 2002.

[31] W. Li *et al.*, “Phase diagram of diblock copolymers confined in thin films,” *Journal of Physical Chemistry B*, vol. 117, no. 17, pp. 5280–5288, 2013.

[32] B. I. Halperin and D. R. Nelson, “Theory of two-dimensional melting,” *Physical Review Letters*, vol. 41, no. 2, pp. 121–124, 1978.

[33] D. R. Nelson and B. I. Halperin, “Dislocation-mediated melting in two dimensions,” *Physical Review B*, vol. 19, no. 5, pp. 2457–2484, 1979.

[34] C. Harrison *et al.*, “Mechanisms of ordering in striped patterns,” *Science*, vol.

290, no. 5496, pp. 1558–1560, 2000.

[35] A. Keller, E. Pedemonte, and F. M. Willmouth, "Macro lattice from segregated amorphous phases of a three block copolymer," *Kolloid-Zeitschrift und Zeitschrift für Polymere*, vol. 238, no. 1–2, pp. 385–389, 1970.

[36] R. J. Albalak, E. L. Thomas, and M. S. Capel, "Thermal annealing of roll-cast triblock copolymer films," *Polymer*, vol. 38, no. 15, pp. 3819–3825, 1997.

[37] M. R. Hammond *et al.*, "Temperature dependence of order, disorder, and defects in laterally confined diblock copolymer cylinder monolayers," *Macromolecules*, vol. 38, no. 15, pp. 6575–6585, 2005.

[38] C. D. Han, J. Kim, and J. K. Kim, "Determination of the order-disorder transition temperature of block copolymers," *Macromolecules*, vol. 22, no. 1, pp. 383–394, 1989.

[39] N. Sakamoto and T. Hashimoto, "Order-disorder transition of low molecular weight polystyrene-*block*-polyisoprene. 1. SAXS analysis of two characteristic temperatures," *Macromolecules*, vol. 28, no. 20, pp. 6825–6834, 1995.

[40] E. W. Cochran, D. C. Morse, and F. S. Bates, "Design of ABC triblock copolymers near the ODT with the random phase approximation," *Macromolecules*, vol. 36, no. 3, pp. 782–792, 2003.

[41] G. E. Stein *et al.*, "Thickness dependent ordering in laterally confined monolayers of spherical-domain block copolymers," *Macromolecules*, vol. 40, no. 16, pp. 5791–5800, 2007.

[42] Z. Di *et al.*, "Structural rearrangements in a lamellar diblock copolymer thin film during treatment with saturated solvent vapor," *Macromolecules*, vol. 43, no. 1, pp. 418–427, 2010.

[43] R. J. Albalak, M. S. Capel, and E. L. Thomas, "Solvent swelling of roll-cast triblock copolymer films," *Polymer*, vol. 39, no. 8-9, pp. 1647–1656, 1998.

[44] S. Park *et al.*, "Lateral ordering of cylindrical microdomains under solvent vapor," *Macromolecules*, vol. 42, no. 4, pp. 1278–1284, 2009.

[45] M. Y. Paik *et al.*, “Reversible morphology control in block copolymer films *via* solvent vapor processing: An *in situ* GISAXS study,” *Macromolecules*, vol. 43, no. 9, pp. 4253–4260, 2010.

[46] C. S. Henkee, E. L. Thomas, and L. J. Fetters, “The effect of surface constraints on the ordering of block copolymer domains,” *Journal of Materials Science*, vol. 23, no. 5, pp. 1685–1694, 1988.

[47] G. Kim and M. Libera, “Morphological development in solvent-cast polystyrene-polybutadiene-polystyrene (SBS) triblock copolymer thin films,” *Macromolecules*, vol. 31, no. 8, pp. 2569–2577, 1998.

[48] G. Kim and M. Libera, “Kinetic constraints on the development of surface microstructure in SBS thin films,” *Macromolecules*, vol. 31, no. 8, pp. 2670–2672, 1998.

[49] S. H. Kim *et al.*, “Highly oriented and ordered arrays from block copolymers *via* solvent evaporation,” *Advanced Materials*, vol. 16, no. 3, pp. 226–231, 2004.

[50] J. Peng *et al.*, “Morphologies in solvent-annealed thin films of symmetric diblock copolymer,” *The Journal of Chemical Physics*, vol. 125, no. 6, pp. 064 702(1–8), 2006.

[51] J. K. Bosworth *et al.*, “Control of self-assembly of lithographically patternable block copolymer films,” *ACS Nano*, vol. 2, no. 7, pp. 1396–1402, 2008.

[52] S. Ludwigs *et al.*, “Self-assembly of functional nanostructures from ABC triblock copolymers,” *Nature Materials*, vol. 2, no. 11, pp. 744–747, 2003.

[53] Y. S. Jung *et al.*, “A path to ultranarrow patterns using self-assembled lithography,” *Nano Letters*, vol. 10, no. 3, pp. 1000–1005, 2010.

[54] X. Zhang *et al.*, “Fast assembly of ordered block copolymer nanostructures through microwave annealing,” *ACS Nano*, vol. 4, no. 11, pp. 7021–7029, 2010.

[55] X. Zhang *et al.*, “Rapid assembly of nanolines with precisely controlled spacing from binary blends of block copolymers,” *Macromolecules*, vol. 44, no. 24, pp.

9752–9757, 2011.

[56] D. Borah *et al.*, "Sub-10 nm feature size PS-*b*-PDMS block copolymer structures fabricated by a microwave-assisted solvothermal process," *ACS Applied Materials & Interfaces*, vol. 5, no. 6, pp. 2004–2012, 2013.

[57] W. I. Park *et al.*, "Directed self-assembly with sub-100 degrees celsius processing temperature, sub-10 nanometer resolution, and sub-1 minute assembly time," *Small*, vol. 8, no. 24, pp. 3762–3768, 2012.

[58] K. A. Koppi, M. Tirrell, and F. S. Bates, "Shear-induced isotropic-to-lamellar transition," *Physical Review Letters*, vol. 70, no. 10, pp. 1449–1452, 1993.

[59] K. A. Koppi *et al.*, "Lamellae orientation in dynamically sheared diblock copolymer melts," *Journal de Physique II*, vol. 2, no. 11, pp. 1941–1959, 1992.

[60] D. E. Angelescu *et al.*, "Macroscopic orientation of block copolymer cylinders in single-layer films by shearing," *Advanced Materials*, vol. 16, no. 19, pp. 1736–1740, 2004.

[61] D. E. Angelescu *et al.*, "Shear-induced alignment in thin films of spherical nanodomains," *Advanced Materials*, vol. 17, no. 15, pp. 1878–1881, 2005.

[62] R. J. Albalak and E. L. Thomas, "Microphase separation of block copolymer solutions in a flow field," *Journal of Polymer Science, Part B: Polymer Physics*, vol. 31, no. 1, pp. 37–46, 1993.

[63] R. J. Albalak and E. L. Thomas, "Roll-casting of block copolymers and of block copolymer-homopolymer blends," *Journal of Polymer Science, Part B: Polymer Physics*, vol. 32, no. 2, pp. 341–350, 1994.

[64] T. Hashimoto *et al.*, "The effect of temperature gradient on the microdomain orientation of diblock copolymers undergoing an order-disorder transition," *Macromolecules*, vol. 32, no. 3, pp. 952–954, 1999.

[65] J. Bodycomb *et al.*, "Single-grain lamellar microdomain from a diblock copolymer," *Macromolecules*, vol. 32, no. 6, pp. 2075–2077, 1999.

[66] B. C. Berry *et al.*, "Orientational order in block copolymer films zone annealed

below the order-disorder transition temperature," *Nano Letters*, vol. 7, no. 9, pp. 2789–2794, 2007.

[67] D. E. Angelescu *et al.*, "Enhanced order of block copolymer cylinders in single-layer films using a sweeping solidification front," *Advanced Materials*, vol. 19, no. 18, pp. 2687–2690, 2007.

[68] G. Singh *et al.*, "Tuning molecular relaxation for vertical orientation in cylindrical block copolymer films *via* sharp dynamic zone annealing," *Macromolecules*, vol. 45, no. 17, pp. 7107–7117, 2012.

[69] G. Singh *et al.*, "Large-scale roll-to-roll fabrication of vertically oriented block copolymer thin films," *ACS Nano*, vol. 7, no. 6, pp. 5291–5299, 2013.

[70] K. Amundson *et al.*, "Effect of an electric field on block copolymer microstructure," *Macromolecules*, vol. 24, no. 24, pp. 6546–6548, 1991.

[71] K. Amundson *et al.*, "Alignment of lamellar block copolymer microstructure in an electric field. 1. Alignment kinetics," *Macromolecules*, vol. 26, no. 11, pp. 2698–2703, 1993.

[72] K. Amundson *et al.*, "Alignment of lamellar block copolymer microstructure in an electric field. 2. Mechanisms of alignment," *Macromolecules*, vol. 27, no. 22, pp. 6559–6570, 1994.

[73] T. L. Morkved *et al.*, "Local control of microdomain orientation in diblock copolymer thin films with electric fields," *Science*, vol. 273, no. 5277, pp. 931–933, 1996.

[74] T. Thurn-Albrecht *et al.*, "Overcoming interfacial interactions with electric fields," *Macromolecules*, vol. 33, no. 9, pp. 3250–3253, 2000.

[75] T. Thurn-Albrecht *et al.*, "Nanoscopic templates from oriented block copolymer films," *Adv. Mater.*, vol. 12, no. 11, pp. 787–791, 2000.

[76] T. Thurn-Albrecht *et al.*, "Ultrahigh-density nanowire arrays grown in self-assembled diblock copolymer templates," *Science*, vol. 290, no. 5499, pp. 2126–2129, 2000.

[77] Y. Tsori and D. Andelman, “Thin film diblock copolymers in electric field: Transition from perpendicular to parallel lamellae,” *Macromolecules*, vol. 35, no. 13, pp. 5161–5170, 2002.

[78] T. Xu *et al.*, “Electric field alignment of symmetric diblock copolymer thin films,” *Macromolecules*, vol. 37, no. 7, pp. 2625–2629, 2004.

[79] V. Olszowka, L. Tsarkova, and A. Böker, “3-dimensional control over lamella orientation and order in thick block copolymer films,” *Soft Matter*, vol. 5, no. 4, pp. 812–819, 2009.

[80] R. A. Segalman, H. Yokoyama, and E. J. Kramer, “Graphoepitaxy of spherical domain block copolymer films,” *Advanced Materials*, vol. 13, no. 15, pp. 1152–1155, 2001.

[81] D. Sundrani, S. B. Darling, and S. J. Sibener, “Guiding polymers to perfection: Macroscopic alignment of nanoscale domains,” *Nano Letters*, vol. 4, no. 2, pp. 273–276, 2004.

[82] J. Y. Cheng, A. M. Mayes, and C. A. Ross, “Nanostructure engineering by templated self-assembly of block copolymers,” *Nature Materials*, vol. 3, no. 11, pp. 823–828, 2004.

[83] G. E. Stein *et al.*, “Single-crystal diffraction from two-dimensional block copolymer arrays,” *Physical Review Letters*, vol. 98, no. 8, pp. 086 101(1–4), 2007.

[84] R. Ruiz *et al.*, “Local defectivity control of 2D self-assembled block copolymer patterns,” *Advanced Materials*, vol. 19, no. 16, pp. 2157–2162, 2007.

[85] R. A. Segalman, A. Hexemer, and E. J. Kramer, “Effects of lateral confinement on order in spherical domain block copolymer thin films,” *Macromolecules*, vol. 36, no. 18, pp. 6831–6839, 2003.

[86] Y. S. Jung, W. Jung, and C. A. Ross, “Nanofabricated concentric ring structures by templated self-assembly of a diblock copolymer,” *Nano Letters*, vol. 8, no. 9, pp. 2975–2981, 2008.

[87] J. Chai and J. M. Buriak, “Using cylindrical domains of block copolymers to self-assemble and align metallic nanowires,” *ACS Nano*, vol. 2, no. 3, pp. 489–501, 2008.

[88] T. Yamaguchi and H. Yamaguchi, “Two-dimensional patterning of flexible designs with high half-pitch resolution by using block copolymer lithography,” *Advanced Materials*, vol. 20, no. 9, pp. 1684–1689, 2008.

[89] I. Bita *et al.*, “Graphoepitaxy of self-assembled block copolymers on two-dimensional periodic patterned templates,” *Science*, vol. 321, no. 5891, pp. 939–943, 2008.

[90] J. K. W. Yang *et al.*, “Complex self-assembled patterns using sparse commensurate templates with locally varying motifs,” *Nature Nanotechnology*, vol. 5, no. 4, pp. 256–260, 2010.

[91] A. Tavakkoli K. G. *et al.*, “Templating three-dimensional self-assembled structures in bilayer block copolymer films,” *Science*, vol. 336, no. 6086, pp. 1294–1298, 2012.

[92] J. Heier *et al.*, “Thin diblock copolymer films on chemically heterogeneous surfaces,” *Macromolecules*, vol. 30, no. 21, pp. 6610–6614, 1997.

[93] J. Heier *et al.*, “Transfer of a chemical substrate pattern into an island-forming diblock copolymer film,” *The Journal of Chemical Physics*, vol. 111, no. 24, pp. 11 101–11 110, 1999.

[94] S. O. Kim *et al.*, “Epitaxial self-assembly of block copolymers on lithographically defined nanopatterned substrates,” *Nature*, vol. 424, no. 6947, pp. 411–414, 2003.

[95] M. P. Stoykovich *et al.*, “Directed assembly of block copolymer blends into nonregular device-oriented structures,” *Science*, vol. 308, no. 5727, pp. 1442–1446, 2005.

[96] M. P. Stoykovich *et al.*, “Directed self-assembly of block copolymers for nanolithography: Fabrication of isolated features and essential integrated circuit geometries,” *ACS Nano*, vol. 1, no. 3, pp. 168–175, 2007.

[97] R. Ruiz *et al.*, "Density multiplication and improved lithography by directed block copolymer assembly," *Science*, vol. 321, no. 5891, pp. 936–939, 2008.

[98] R. Ruiz, E. Dobisz, and T. R. Albrecht, "Rectangular patterns using block copolymer directed assembly for high bit aspect ratio patterned media," *ACS Nano*, vol. 5, no. 1, pp. 79–84, 2011.

[99] C.-C. Liu *et al.*, "Chemical patterns for directed self-assembly of lamellae-forming block copolymers with density multiplication of features," *Macromolecules*, vol. 46, no. 4, pp. 1415–1424, 2013.

[100] L. M. Bronstein *et al.*, "Metalated diblock and triblock poly(ethylene oxide)-*block*-poly(4-vinylpyridine) copolymers: Understanding of micelle and bulk structure," *Journal of Physical Chemistry B*, vol. 109, no. 40, pp. 18 786–18 798, 2005.

[101] M. Möller, J. P. Spatz, and A. Roescher, "Gold nanoparticles in micellar poly(styrene)-*b*-poly(ethylene oxide) films — Size and interparticle distance control in monoparticulate films," *Advanced Materials*, vol. 8, no. 4, pp. 337–340, 1996.

[102] O. A. Platonova *et al.*, "Cobalt nanoparticles in block copolymer micelles: Preparation and properties," *Colloid and Polymer Science*, vol. 275, no. 5, pp. 426–431, 1997.

[103] Z. Lu *et al.*, "Palladium nanoparticle catalyst prepared in poly(acrylic acid)-lined channels of diblock copolymer microspheres," *Nano Letters*, vol. 1, no. 12, pp. 683–687, 2001.

[104] B. H. Sohn and R. E. Cohen, "Processible optically transparent block copolymer films containing superparamagnetic iron oxide nanoclusters," *Chemistry of Materials*, vol. 9, no. 1, pp. 264–269, 1997.

[105] M. Moffitt, H. Vali, and A. Eisenberg, "Spherical assemblies of semiconductor nanoparticles in water-soluble block copolymer aggregates," *Chemistry of Materials*, vol. 10, no. 4, pp. 1021–1028, 1998.

[106] S. Bhaviripudi *et al.*, "Block-copolymer assisted synthesis of arrays of metal

nanoparticles and their catalytic activities for the growth of SWNTs," *Nanotechnology*, vol. 17, no. 20, pp. 5080–5086, 2006.

[107] M. Aizawa and J. M. Buriak, "Block copolymer-templated chemistry on Si, Ge, InP, and GaAs surfaces," *Journal of the American Chemical Society*, vol. 127, no. 25, pp. 8932–8933, 2005.

[108] J. Chai *et al.*, "Assembly of aligned linear metallic patterns on silicon," *Nature Nanotechnology*, vol. 2, no. 8, pp. 500–506, 2007.

[109] B. J. Melde *et al.*, "Silica nanostructures templated by oriented block copolymer thin films using pore-filling and selective-mineralization routes," *Chemistry of Materials*, vol. 17, no. 18, pp. 4743–4749, 2005.

[110] Q. Peng *et al.*, "Nanoscopic patterned materials with tunable dimensions *via* atomic layer deposition on block copolymers," *Advanced Materials*, vol. 22, no. 45, pp. 5129–5133, 2010.

[111] Q. Peng *et al.*, "A route to nanoscopic materials *via* sequential infiltration synthesis on block copolymer templates," *ACS Nano*, vol. 5, no. 6, pp. 4600–4606, 2011.

[112] M. Ramanathan *et al.*, "Emerging trends in metal-containing block copolymers: Synthesis, self-assembly, and nanomanufacturing applications," *Journal of Materials Chemistry C*, vol. 1, no. 11, pp. 2080–2091, 2013.

[113] Y. Qiao, D. Wang, and J. M. Buriak, "Block copolymer templated etching on silicon," *Nano Letters*, vol. 7, no. 2, pp. 464–469, 2007.

[114] X. Zhang *et al.*, "Constructing metal-based structures on nanopatterned etched silicon," *ACS Nano*, vol. 5, no. 6, pp. 5015–5024, 2011.

[115] C. T. Black, "Self-aligned self assembly of multi-nanowire silicon field effect transistors," *Applied Physics Letters*, vol. 87, no. 16, pp. 163 116(1–3), 2005.

[116] J. Y. Cheng *et al.*, "Formation of a cobalt magnetic dot array *via* block copolymer lithography," *Advanced Materials*, vol. 13, no. 15, pp. 1174–1178, 2001.

[117] Y. S. Jung and C. A. Ross, "Orientation-controlled self-assembled nanolithog-

raphy using a polystyrene-polydimethylsiloxane block copolymer," *Nano Letters*, vol. 7, no. 7, pp. 2046–2050, 2007.

[118] M. Park *et al.*, "Block copolymer lithography: Periodic arrays of $\sim 10^{11}$ holes in 1 square centimeter," *Science*, vol. 276, no. 5317, pp. 1401–1404, 1997.

[119] P. Mansky *et al.*, "Nanolithographic templates from diblock copolymer thin films," *Applied Physics Letters*, vol. 68, no. 18, pp. 2586–2588, 1996.

[120] Y.-C. Tseng *et al.*, "Enhanced block copolymer lithography using sequential infiltration synthesis," *Journal of Physical Chemistry C*, vol. 115, no. 36, pp. 17 725–17 729, 2011.

[121] T. Xu *et al.*, "Block copolymer surface reconstuction: A reversible route to nanoporous films," *Advanced Functional Materials*, vol. 13, no. 9, pp. 698–702, 2003.

[122] S. Park *et al.*, "Macroscopic 10-terabit-per-square-inch arrays from block copolymers with lateral order," *Science*, vol. 323, no. 5917, pp. 1030–1033, 2009.

[123] J. Y. Cheng *et al.*, "Fabrication of nanostructures with long-range order using block copolymer lithography," *Applied Physics Letters*, vol. 81, no. 19, pp. 3657–3659, 2002.

[124] H.-C. Kim *et al.*, "A route to nanoscopic SiO_2 posts *via* block copolymer templates," *Advanced Materials*, vol. 13, no. 11, pp. 795–797, 2001.

[125] D. J. Milliron *et al.*, "Solution-phase deposition and nanopatterning of GeSbSe phase-change materials," *Nature Materials*, vol. 6, no. 5, pp. 352–356, 2007.

[126] R. R. Li *et al.*, "Dense arrays of ordered GaAs nanostructures by selective area growth on substrates patterned by block copolymer lithography," *Applied Physics Letters*, vol. 76, no. 13, pp. 1689–1691, 2000.

3

Density Doubling of Templated Metal Nanostructures

3.1 Introduction

The versatility of linear diblock copolymers (diBCPs) in patterning periodic nanostructures with dimensions between 10 to 50 nm is well known.[2–5] Lamellar, cylindrical, and spherical structures can be assembled simply by modulating the volume ratio of the templating polymer's two block segments. These structures can then be used to pattern nanolines or nanodots for applications including magnetic storage media,[6–9] flash memory,[10] nanowire transistors,[11] photonic devices,[12, 13] and tissue interfacing.[14, 15]

The BCP self-assembly theory developed by Semenov in the strong segregation limit,[16] predicts that the characteristic period (L) of spherical, cylindrical, or lamellar structures in the strong segregation limit scale with the polymer's degree of polymerization (N), Flory-Huggins parameter (χ), and Kuhn length (a), as described in Equation 3.1.1.

The material in this chapter is based on published work from [1]. In this work, Dr. Xiaojiang Zhang helped with the solvent annealing of around half of the samples swelled in the THF/water mixture; Jeffrey Murphy performed LER and line width measurements and helped produce Figures 3.10b, 3.14, 3.17, 3.18e; Dr. Jinan Chai is credited as being the first to demonstrate the potential of this technique; SAM was performed by the Alberta Centre for Surface Engineering and Science (ACSES); Dr. Xiaojiang Zhang, Jeffrey Murphy, Dr. Kenneth Harris, and Dr. Jillian Buriak all contributed to useful discussions.

$$L \sim aN^{2/3}\chi^{1/6} \tag{3.1.1}$$

Thus, the dimensions and characteristic period of the self-assembled polymer domains may be tuned by varying the length of BCP chains. However, while linear diBCPs have been shown to efficiently create patterns in the 5 to 50 nm size range, self-assembly of structures at either extreme of this range becomes extremely difficult. The following sections will describe recent work in extending the limits of this range.

3.1.1 Above 100 nm Block Copolymer Patterning

The motivation for using BCPs to self-assemble into domains with periods greater than 100 nm has mainly been driven by the desire to fabricate photonic devices or polarisers using self-assembly. Nanostructures with alternating dielectric constants and periods ranging from 100 nm to 200 nm exhibit iridescent behaviour useful for photonic applications in the visible light spectrum.[12] In telecommunications, where near-infrared light is controlled, domain periods of around 250 nm are required.[17] Although extending polymer chain lengths do lead to increased periods as described by Equation 3.1.1, one significant drawback is that these high molecular weight polymers have a high degree of chain entanglement. This entanglement results in significantly reduced chain mobility and high viscosity, even for $T > T_g$.

One strategy that has been employed to extend the periodicity of self-assembled BCP domains is to blend homopolymer chains with moderately large BCPs to swell the domains, thus enlarging the overall spacing of the resulting structures. For example, the blending of a PS-*b*-PI BCP with $M_{n,\mathrm{PS}} = 194$ kg/mol and $M_{n,\mathrm{PI}} = 197$ kg/mol [henceforth denoted as PS(194k)-*b*-PI(197k)] with PS homopolymer resulted in spherical patterns with centre-to-centre spacing of around 180 nm.[17] Ternary blends of the same BCP with equal amounts

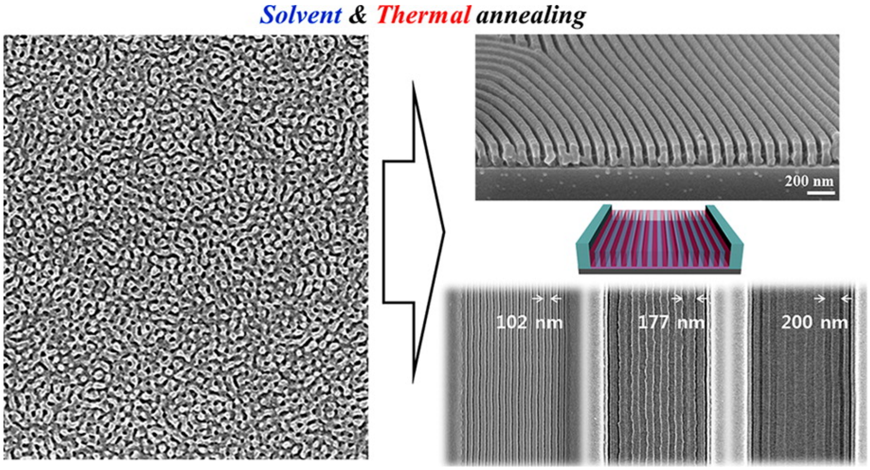

Figure 3.1: Linear diBCPs with large M_n can self-assemble into line structures with periodicities of 102 nm, 177 nm, and 200 nm. Reprinted with permission from ref. [19]. Copyright © 2013 American Chemical Society.

of both PS and PI homopolymers resulted in lamellar patterns with tunable periodicities. As the percentage of homopolymers in the blend increased from 0% up to 60%, the lamellar period could be tuned from 110 nm up to 200 nm.[12] However, the addition of homopolymer dopants to the films tended to introduce defects to the final structures.[18] Homopolymer-rich regions, where the homopolymer had completely segregated from the BCP, were common, and made this technique highly undesirable for fabricating defect-free arrays in this size range.

Recently, a method was developed to facilitate the self-assembly of ultra-high molecular weight linear diBCPs by sequentially combining a non-selective solvent anneal with a thermal anneal.[19] The solvent anneal in THF was found to be effective in reducing the defect densities of the perpendicular lamellar patterns but were also found to reduce the line periodicity according to the dilution approximation.[20] This reduction in periodicity was reversed through a subsequent thermal anneal, which restored the lines to their characteristic spacing without reintroducing defects. The PS-*b*-PMMA polymers had total molecular weights of $M_n = 256, 733, 1000$ kg/mol, and these produced lines with periodicities of 102 nm, 177 nm, and 200 nm, respectively (Figure 3.1).

One other particularly interesting solution to the BCP chain entanglement problem has been the use of comb or brush copolymers. A comb or brush polymer architecture consists of a linear polymer backbone with densely spaced polymer arms. Block comb copolymers are comb polymers with backbones divided into separate blocks, each with unique polymers for their arms. The use of comb copolymers provide two major advantages over linear diBCPs.[18] Firstly, the steric effects of the densely spaced arms lead to a straightening of the backbone, thus causing these polymers to behave more as rigid rods than as coils. These rigid rods avoid much of the entanglement problems experienced by normal linear polymers, and are thus more able to self-assemble into the desired structures. Secondly, the synthesis of these polymers is also a possible pathway towards the production of polymers greater than 1000 kg/mol. This is extremely difficult to do using linear polymers because the time required to synthesize these linear polymers increases dramatically with the length of the chains.

Runge and Bowden synthesized these block comb copolymers by first synthesizing a BCP backbone and then grafting PS arms onto one of the blocks.[18] Polymers with molecular weights in excess of 6000 kg/mol could be synthesized, and could self-assemble into lamellar, cylinder, and spherical morphologies. One polymer with molecular weight of 1260 kg/mol formed cylinders with domain periodicity of 258 nm. By tuning the volume fraction of the blocks, the length of the PS arms, or the length of the backbone; lamellar, cylindrical, and spherical morphologies with controlled periodicity could be formed.[21] Polystyrene-polylactide (PS-PLA) block brush copolymers were also synthesized by Rzayev, and these block brush copolymers self-assembled into structures with domain spacing up to 163 nm.[22] Xia *et al.* developed an alternate method of synthesis for these brush copolymers that did not require grafting polymer arms.[23] Instead, individual macromonomers already containing an attached arm were formed first before they were polymerized (Figure 3.2). As a result, both random and block brush copolymer architectures were possible, leading to slightly different self-assembly arrangements.

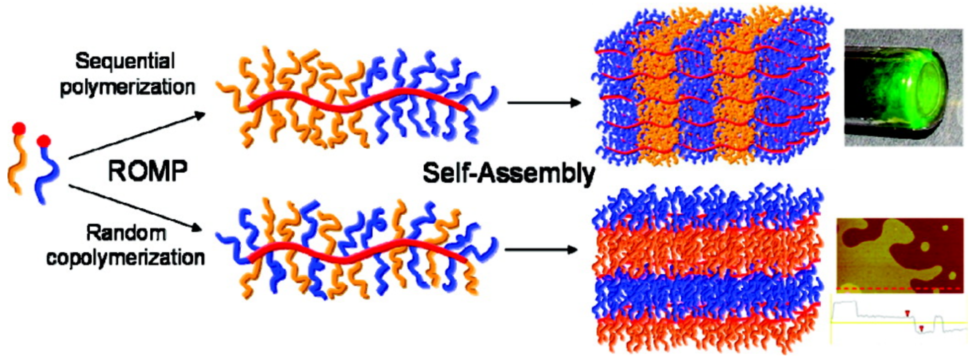

Figure 3.2: Macromonomer precursors were polymerized to form either random or block brush copolymers. These polymers were then self-assembled into lamellar structures. Reprinted with permission from ref. [23]. Copyright © 2009 American Chemical Society.

3.1.2 Sub-10 nm Block Copolymer Patterning

There have also been significant efforts to form BCP structures in the sub-10 nm regime. This has primarily been driven by the requirements of the semiconductor industry to fabricate nanostructures beyond the limits of conventional lithography.[24] However, as described in Chapter 2, for self-assembly into segregated domains to occur, Equation 3.1.2 must hold.[25] Thus, for any given type of linear BCP type, there is a minimum possible domain spacing.

$$\chi N \gtrsim 10.5 \tag{3.1.2}$$

One strategy to reduce the minimum patternable feature size is to increase the χ parameter of the polymer. By doing so, a lower N may be reached before self-assembly ceases to occur. An added benefit to increasing χ is its effect on the width of the interface (b) between two domains after self-assembly, as shown in Equation 3.1.3.[26] A narrow interface, small b, indicates a sharp transition from one domain type to another. This is particularly important in the fabrication of nanolines when the line edge roughness is to be minimized.

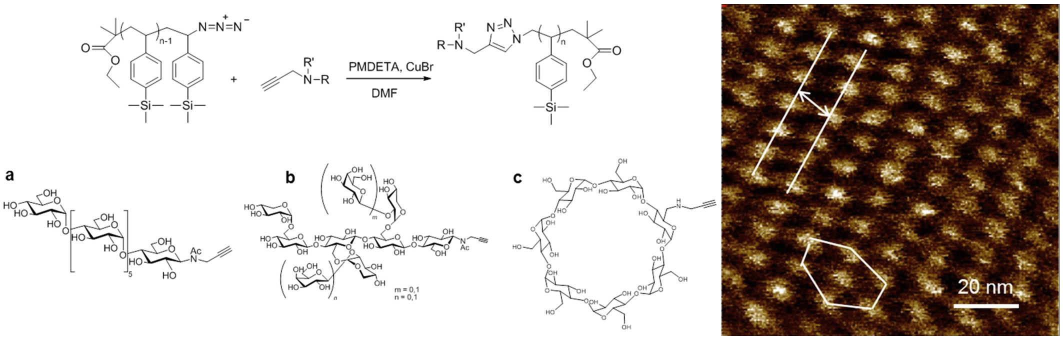

Figure 3.3: The oligosaccharide-silicon-containing BCPs shown in this figure were synthesized and self-assembled into cylinder structures. The BCP displayed in (a) produced dots with 11.4 nm spacing, as shown in the AFM image. Adapted with permission from ref. [32]. Copyright © 2012 American Chemical Society.

$$b = \frac{2a}{\sqrt{6\chi}} \tag{3.1.3}$$

Because of the above mentioned reasons, there has been a gradual shift from polymers such as PS-*b*-PMMA, PS-*b*-PEO, and PS-*b*-PI ($\chi_{\mathrm{PS-PMMA}} = 0.04$,[27] $\chi_{\mathrm{PS-PEO}} = 0.08$,[28] $\chi_{\mathrm{PS-PI}} = 0.09$[28] at room temperature), to polymers with higher χ parameters such as PS-*b*-P2VP and PS-*b*-PDMS ($\chi_{\mathrm{PS-P2VP}} = 0.18$,[29] $\chi_{\mathrm{PS-PDMS}} = 0.27$[28] at room temperature). Sub-10 nm features have recently been produced through the use of polymers such as PS-*b*-PDMS,[30] P2VP-*b*-PDMS,[31] poly(trimethylsilylstyrene)-*b*-polylactide ($\chi_{\mathrm{PTMSS-PLA}} = 0.47$ at room temperature),[32] and oligosaccharide-silicon-containing BCPs.[33] With some of these new polymers, characteristic domain sizes as low as 5 nm have been created, as shown in Figure 3.3.

One other way of tuning the size of self-assembled BCP structures is to alter the architecture of the polymer chains. Cyclic copolymers have been found to exhibit higher glass transition temperatures, lower viscosities, and decreased hydrodynamic volumes when compared to their linear analogues.[34] Poelma *et al.* synthesized these cyclic copolymers by coupling bisalkyne PEO chains with

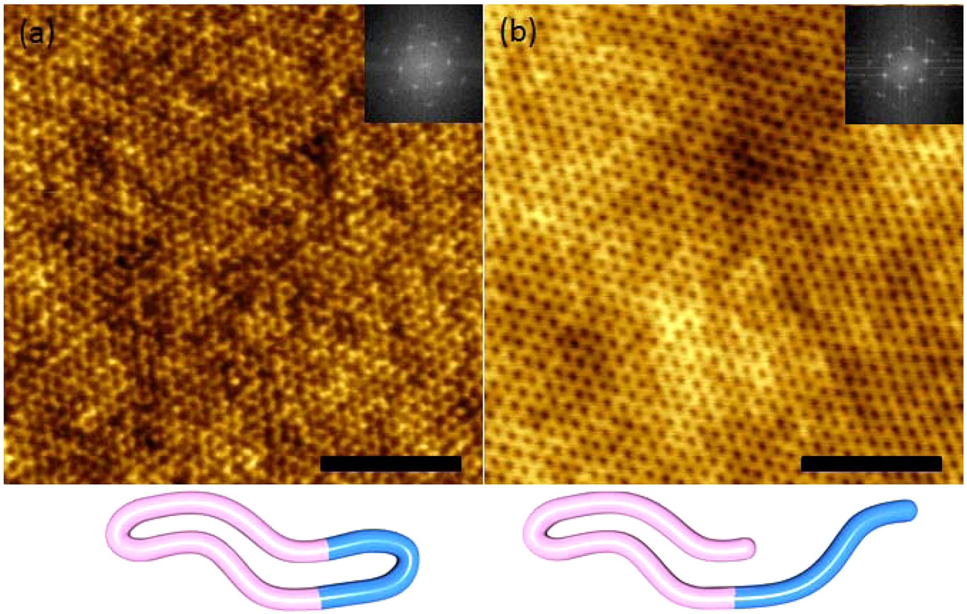

Figure 3.4: AFM images of cyclic copolymers (a) and their linear analogues (b) along with FFTs of the images in the corner. The domain spacing of the cyclic and linear polymers are 20 and 26 nm, respectively. Scale bars are 250 nm. Reprinted with permission from ref. [34]. Copyright © 2012 American Chemical Society.

bisazide PS chains in a highly dilute environment.[34] When these cyclic polymers cPS(13k)-*b*-PEO(5k) were compared with two of their linear analogues PS(13k)-*b*-PEO(5k) and PS(7k)-*b*-PEO(2.7k), it was found that cPS(13k)-*b*-PEO(5k) produced cylinders with spacing of 20 nm, while the linear PS(13k)-*b*-PEO(5k) produced cylinders with spacing of 26 nm. The half-sized linear polymer PS(7k)-*b*-PEO(2.7k), which corresponded to the length of the cyclic copolymer folded in half, was unable to phase-separate into any meaningful structures. Thus, the cyclic architecture of polymers resulted in a 33% reduction in the spacing of the cylinders (Figure 3.4).

3.1.3 Density-Doubled Nanostructures

In this chapter, we demonstrate a simple and efficient approach that is compatible with the above mentioned techniques to further reduce the periodicity of structures templated by a given cylinder-forming polymer. In annealed BCP films containing two layers of parallel horizontal cylinders, cylinders of the upper layer form over the interstices of the cylinders in the underlying lower layer (Figure 3.5a) as described in various studies.[35–38] While each layer of cylinders has a pitch of L, if the three-dimensional assembly of parallel cylinders collapses and the matrix between the cylinders is removed, an array of parallel cylinders with half the original pitch ($L/2$) is formed. This effectively increases the characteristic feature density of a given BCP by a factor of two without requiring multiple steps of polymer pattern transfer.

PS-*b*-P2VP was chosen as the polymer platform to demonstrate the feasibility of this method, and the resulting template was used to pattern metal lines at twice the density normally possible for the polymer. SEM images of platinum lines templated by monolayers and bilayers of cylinders from a PS-*b*-P2VP polymer (Figures 3.5b,c) show that the line pitch is halved from 47 nm to 24 nm for this given polymer. Cross section SEM images (Figure 3.5d) also show that the metal lines resulting from the upper and lower layers could be readily distinguished due to their contrast in the SEM. The stacking behaviour of two layers of hexagonally close-packed dot arrays allows this density doubling approach to be similarly applied to dots,[39] as shown in Figures 3.5e-g.

Density doubling should be generalizable for pattern formation in other BCP systems so long as one block can be selectively removed[40] (in the present case, the PS block). If inherently etch-resistant polymer blocks such as PDMS[30, 41] or PFS[42] are chosen, or if the resulting density-doubled structures are made etch-resistant through further processing steps,[43–45] then these patterns from alternative BCPs could be used as etch masks in subsequent patterning steps.[41]

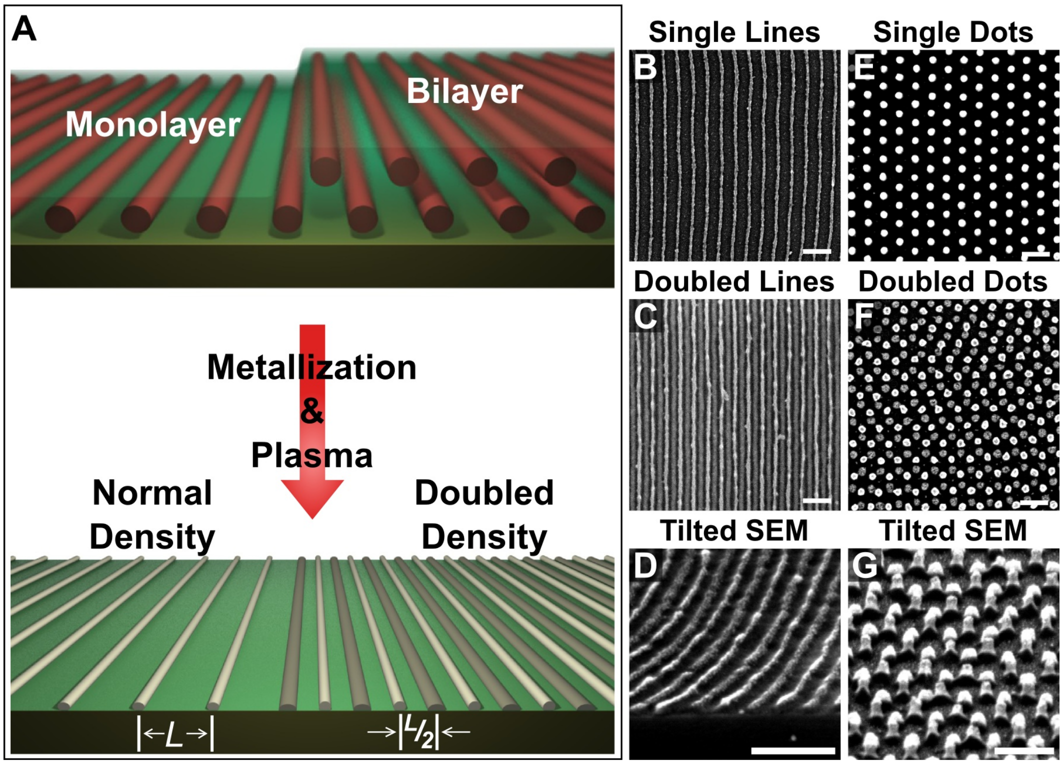

Figure 3.5: (a) A schematic of the self-assembled horizontal cylindrical structures in a polymer film. In areas where only a monolayer of cylinders existed, lines with characteristic spacing of L were observed after the metallization step was performed (b). In areas where bilayers of BCP cylinders existed, the line spacing was halved to $L/2$ (c). The cross-section image (d) demonstrated that both layers of lines were made of clearly identifiable structures, with the top layer lines being slightly brighter and narrower than those from the underlying layer. It was also possible to create double-layer dot patterns (e-g), making it possible to double the densities of dot patterns using this technique. All scale bars are 100 nm. Reprinted with permission from ref. [1]. Copyright © 2011 American Chemical Society.

3.2 Experimental

3.2.1 Materials

Silicon (100) wafers (prime grade, 100 mm diameter, n-type, phosphorous-doped, resistivity ρ = 5–10 $\Omega\cdot$cm) were purchased from University Wafer. 38% HCl (aq) and 30% NH_4OH (aq) were obtained from J. T. Baker; methanol and 30% H_2O_2 were obtained from Fisher Scientific; tetrahydrofuran (THF) and toluene were obtained from Caledon Laboratories Ltd. Ultrapure water with $\rho > 18$ M$\Omega\cdot$cm from a Millipore Milli-Q system was used for all experiments. Six sizes of cylinder-forming PS-*b*-P2VP BCPs were obtained from Polymer Source: PS(125k)-*b*-P2VP(58.5k), PS(56k)-*b*-P2VP(21k), PS(50k)-*b*-P2VP(16.5k), PS(44k)-*b*-P2VP(18.5k), PS(32k)-*b*-P2VP(12.5k), and PS(23.6k)-*b*-P2VP(10.4k). Polystyrene with $M_w = 192$ kg/mol was obtained from Sigma Aldrich. The metallization salts $Na_2PtCl_4\cdot xH_2O$ and $Na_2PdCl_4\cdot 3H_2O$ were obtained from Strem Chemicals.

3.2.2 Sample Preparation

Silicon wafers were diced into 1 × 1 cm squares using the Disco DAD 321 dicing saw. The resulting squares were degreased with methanol in an ultrasonic bath for 15 min and dried with a stream of N_2 gas. Standard RCA I (1:1:6 solution of 30% NH_4OH (aq), 30% H_2O_2, and water at 80 °C) and RCA II (1:1:5 solution of 38% HCl (aq), 30% H_2O_2, and water at 80 °C) cleaning steps were applied sequentially for 15 min each.[46] The substrates were then thoroughly rinsed with water and dried in a N_2 stream.

Cylinder-forming PS-*b*-P2VP was dissolved in toluene overnight at room temperature to form casting solutions. These casting solutions had BCP concentrations ranging from 0.5% w/w to 3% w/w. By spin casting these solutions onto the cleaned silicon squares at speeds of 1000 to 6000 rpm, films of varying thicknesses (h_o) were be formed. The resulting film thicknesses were measured

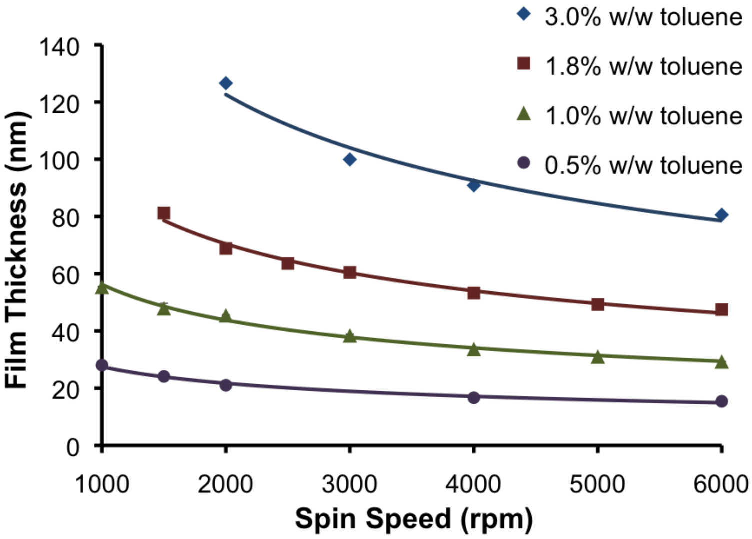

Figure 3.6: Film thicknesses attained at different spin speeds.

using an L116S ellipsometer from Gaertner Scientific. The measurements were made with the incident $\lambda = 632.8$ nm light source reflecting off the sample surface 70° from the normal. Figure 3.6 demonstrates that any h_o ranging from 30 nm to 70 nm could be attained simply by selecting an appropriate casting solution concentration and spin speed.

Due to thin film interference, these BCP films displayed different colours depending on their thickness.[38, 47] For example, 50 nm, 70 nm, or 100 nm films as measured by ellipsometry were observed to be brown, purple, and blue, respectively. The BCP films were uniform in thickness over the majority of the surface, as was confirmed by ellipsometry measurements. However, especially for films cast at lower spin speeds, the film thickness near the edge of the samples tended to increase significantly. Thus, as long as characterization of film and BCP structures were confined to the central regions of these samples, the measured results remained uniform.

3.2.3 Self-Assembly and Metal Templating

Solvent annealing was used as the method for increasing polymer mobility, due to its ability to induce the self-assembly of large polymers into ordered line patterns. Samples were placed in a 3.8 L desiccator system with solvent vapour at room temperature, and sealed for a predetermined duration of time. After completion of the anneals, the chambers were immediately purged with air and the samples were removed. The resulting soft patterns were then fixed through a metallization process, which involved immersing the samples in metal salt solutions [10 mM Na_2PtCl_4 (aq) and 0.9% HCl (aq)] for 3 h, as described in previous work by Chai and Buriak.[43, 44] Prior to immersion in this solution, the horizontal P2VP cylinders are surrounded by a hydrophobic PS matrix, which acts as a barrier between the P2VP blocks and the metal anionic complexes.[43] However, P2VP is highly sensitive to pH, and in sufficiently acidic conditions, it begins to swell due to the protonation of its pyridyl groups. Studies have shown that P2VP microgel particle diameters can swell up to 5 or 6 times the original size diameter when pH is lowered below its $\mathrm{p}K_a$ of 4.5.[48, 49] Thus, immersion of these BCP films in 0.9% HCl (aq) causes the P2VP cylinders to swell. However, due to the lateral confinement by the surrounding glassy PS matrix, these blocks are forced to pierce the PS overlayer, forming mushroom-capped perforations on the surface, and thus allowing contact between the swelled P2VP blocks and the anionic metal complexes in solution (Figure 3.7).[43] Access of the water phase to the P2VP block allows for anionic metal complexes such as $[PtCl_4]^{2-}$ to be electrostatically bound to the positively charged protonated pyridyl groups. After this 3 h metallization process, the sample was treated with a 25 s O_2 plasma in the Plasmalab Etch system at 50 mTorr and 30 W RF power. This plasma treatment served to remove the surrounding PS matrix and also to reduce the P2VP-metal salt complexes into platinum metal nanolines. Once the nanostructures were fixed by the plasma treatment, they were then examined inside a Hitachi-4800 SEM.

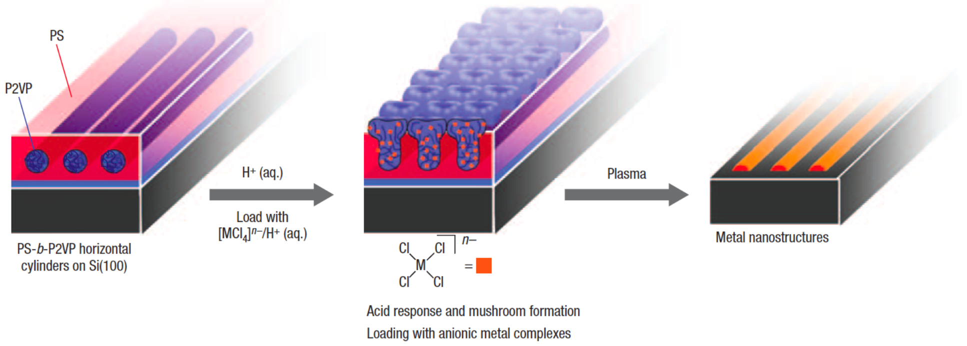

Figure 3.7: P2VP blocks exposed to acidic conditions swell and perforate the overlying PS layer, allowing loading of anionic metal salts into the P2VP blocks. A subsequent plasma step reduces these complexes into metal nanostructures. Reprinted by permission from Macmillan Publishers Ltd: Nature Nanotechnology,[43] copyright © 2007.

3.3 Density-Doubled Structures

Density-doubled line patterns were obtained for PS-*b*-P2VP polymers of various molecular weights by annealing $h_o = 40$ nm films in a 10:1 mixture of THF and water (22 mL of solvent with a surface area of 65 cm^2) for 20 h. As shown in the SEM images in Figure 3.8, the pitch of these density-doubled lines grew with the molecular weight of the templating BCP. For comparison, the line pitches of solvent annealed monolayer and bilayer regions were compared with the monolayer pitches obtained from thermal annealing in Table 3.1. The results showed that the pitches of lines templated from bilayer cylinders were around half that of lines templated from monolayer cylinders. It was also important to note that for the two largest polymers, thermal annealing at 180 °C for 50 h was not enough to obtain line patterns. This highlights the importance of using solvent annealing for larger polymers.

As shown in Figure 3.8, lines templated from the two different layers of cylinders were visibly distinct from each other. Lines templated from the upper BCP layer were brighter and slightly narrower than those templated from the bottom BCP layer, possibly due to greater loading of the metal ion precursor

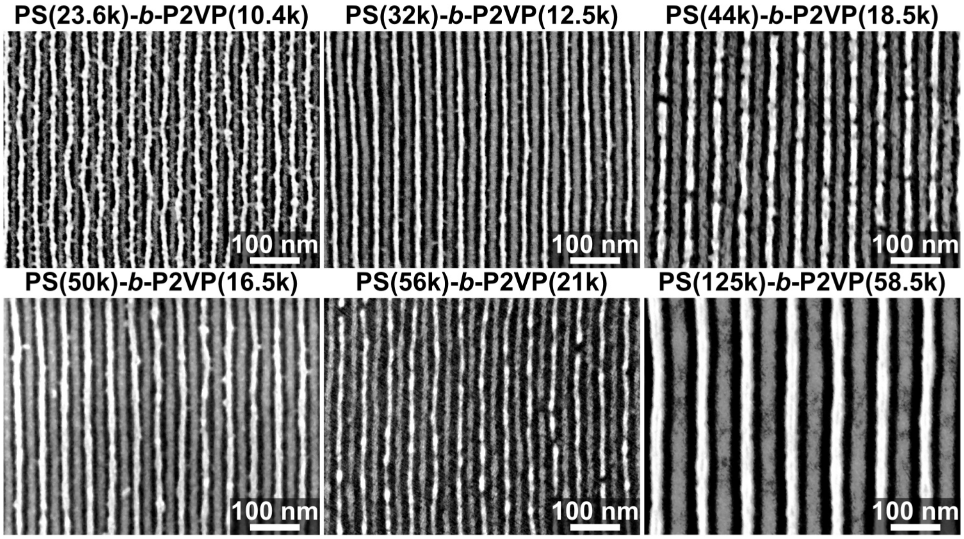

Figure 3.8: Six SEM micrographs of metal line patterns formed using the bilayer approach for various molecular weights of PS-*b*-P2VP. The samples were each annealed with vapour from a 10:1 THF/water mixture for 20 h and subjected to a Pt metallization and plasma step. Adapted with permission from ref. [1]. Copyright © 2011 American Chemical Society.

Table 3.1: Line Spacings for Polymers after Annealing

Polymer	Line Pitches & Standard Deviations (nm)		
	Thermal Anneal	Solvent Anneal Monolayer	Solvent Anneal Bilayer
PS(125k)-*b*-P2VP(58.5k)	Dots	84 ± 2	41 ± 5
PS(56k)-*b*-P2VP(21k)	Dots	50 ± 4	25 ± 1
PS(50k)-*b*-P2VP(16.5k)	45 ± 5[a]	48 ± 3	24 ± 1
PS(44k)-*b*-P2VP(18.5k)	49 ± 7	52 ± 1	26 ± 1
PS(32k)-*b*-P2VP(12.5k)	40 ± 9	43 ± 4	21 ± 2
PS(23.6k)-*b*-P2VP(10.4k)	30 ± 6	35 ± 4	17 ± 3

[a] Mixture of dots and horizontal lines; line spacing from the horizontal lines is shown.

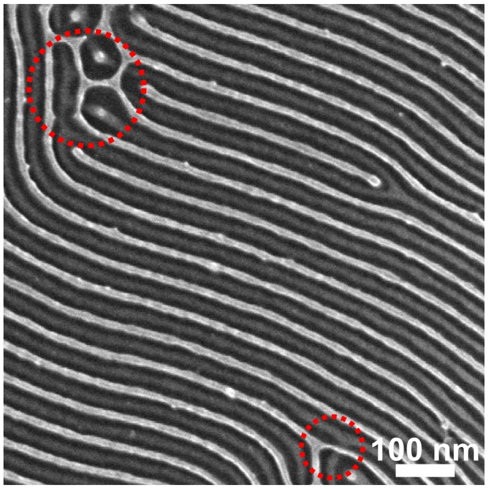

Figure 3.9: Images displaying disordered regions of density-doubled metal line patterns are used to determine whether lines are templated by upper or lower layer cylinders.

in the upper layer. To determine whether the lines originated from the top or bottom layers of cylinders, defect regions such as the one in Figure 3.9 were examined for line overlap. The brighter lines were consistently found to cross over the dimmer lines, suggesting that the brighter lines originated from the top layer, while the dimmer lines originated from the underlying layer.

LER and line width measurements were performed on a selection of these BCP samples annealed in the THF/water mixtures. These measurements were performed by calculating the average point-to-point deviation of a line edge from the corresponding model edge.* The LER was evaluated for line segments at least 15 μm long, and 3σ values were reported. The measured LER values ranged from 2.0 nm [PS(32k)-*b*-P2VP(12.5k)] to 4.3 nm [PS(50k)-*b*-P2VP(16.5k)] for bright lines, and 2.2 nm to 5.4 nm for dark lines from the same samples. The data showed that dark lines templated from the lower BCP layer were somewhat rougher (2% to 44% greater LER values) than lines

---

*Pixels belonging to the lines were distinguished from background pixels by their brightness and isolated with the help of a threshold function. The effect of noise and pixelation on the LER measurements was minimized by using high-resolution (2560 x 1920 pixels) SEM images obtained at 300,000 magnification with 40 s scan times. Thus, in these images, 1 nm was approximately 6 pixels long.

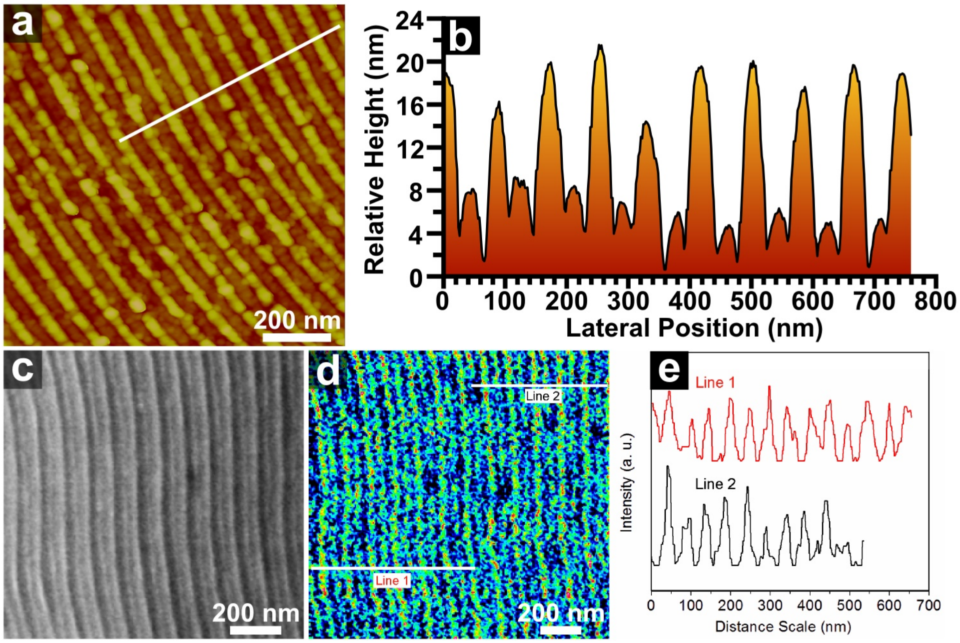

Figure 3.10: Metallized density-doubled line patterns templated by PS(125k)-*b*-P2VP(58.5k) were characterized by AFM and SAM after plasma treatment. (a,b) The AFM map and line scan of the sample showed that both layers were present. The SEM image (c) with corresponding Auger map (d) and line scans (e) of a sample metallized with palladium demonstrated that both layers were metallized. Adapted with permission from ref. [1]. Copyright © 2011 American Chemical Society.

templated from the upper layer, but all of the measured LER values were found to be similar to LER values in contemporary structures fabricated by EBL.[50]

Further characterization using AFM and scanning Auger mapping (SAM) was performed on PS(125k)-*b*-P2VP(58.5k) polymer samples annealed in the THF/water mixture after plasma treatment (Figure 3.10). AFM was used to determine the height profile of the sample, and the line scan obtained in (a) confirmed that lines templated from the top layer were around 10 nm higher than those templated from the lower layer. SAM was also used to determine whether metallization had occurred in both layers of cylinders. For a stronger Auger signal, the polymer was metallized using solutions of palladium salt in-

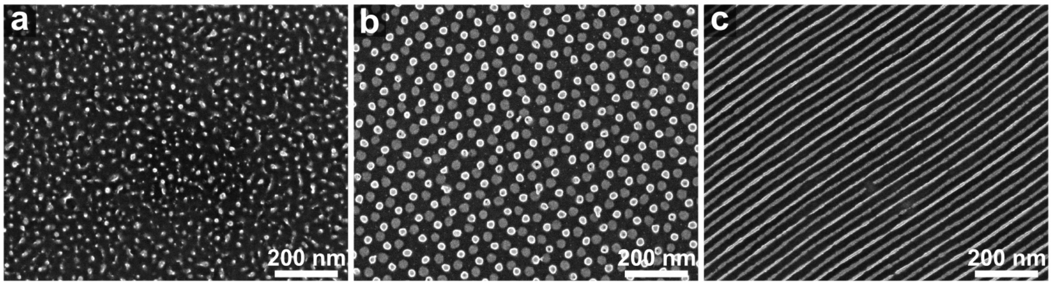

Figure 3.11: PS(125k)-*b*-P2VP(58.5k) films were annealed in a 3.8 L desiccator with 20 mL of neat THF. SEMs of the Pt-metallized structures demonstrate the evolution from randomized dots in the as cast film (a), to bilayers of hexagonally close-packed spherical domains after 24 h (b), and finally to density-doubled lines after 72 h (c).

stead of platinum. The SEM image (b) and corresponding Auger electron map (c) of a metallized sample after plasma treatment revealed that line patterns from both layers were indeed metallized.[†]

Density-doubled dot patterns could also be made using PS(125k)-*b*-P2VP(58.5k). This was found only to be possible through annealing the polymer in the presence of neat THF. When a 40 nm film was placed in the 3.8 L desiccator system with 20 mL (12 cm^2) of neat THF, the disordered structures in the as-cast film slowly evolved into highly ordered density-doubled dot patterns after 24 h (Figure 3.11). However, if the anneal was continued to 72 h, the dot patterns were transformed into density-doubled line patterns. Thus, the density-doubled dot patterns were likely only kinetic intermediate structures, and were not the final equilibrium patterns of the polymer.

[†] Auger electrons at different energies were collected by the detectors, and a map of the (P-B)/B signal of Pd MNN at 325 eV was created. This image pushes the resolution limits of SAM.

3.4 Nanostructure Evolution

The progress of a solvent anneal has in the past been expressed in terms of the anneal duration. However, the anneal duration is a limited measure of anneal progress because it is highly dependent on many parameters including the solvent chamber geometry, ambient temperature, and the solvent type. As a result, the time required for a film to attain the desired structures through self-assembly changes with each system. For higher reproducibility, a more reliable metric for the progress of an anneal is required. To fully appreciate all the intricacies of the solvent annealing system and understand how these parameters affect the progress of a typical solvent anneal, one must first understand the dynamics of a typical solvent anneal.

3.4.1 Theoretical Derivations

The earliest solvent anneals consisted of an inverted container of volume V enclosing the sample and solvent in liquid phase, as shown in Figure 3.12. A mass was often placed on top of the apparatus to reduce the leakage of solvent from under the edge of the container. The enclosed chamber allowed the solvent vapour to increase within the chamber, which in turn increased the infiltration of solvent in the sample film. This absorbed solvent swelled and plasticized the polymer network, sufficiently increasing the mobility of polymer chains to self-assemble into thermodynamically favourable configurations. The amount of solvent infiltrating the polymer film is highly dependent on the solvent vapour pressure in the chamber.[51] Thus, a relation describing the solvent vapour pressure within the chamber would be highly desirable.

Assuming constant chamber volume and temperature, the ideal gas law (Equation 3.4.1) predicts that the time derivative of solvent vapour pressure ($\frac{dP}{dt}$) must vary with the time derivative of the amount of solvent vapour in the chamber ($\frac{dn}{dt}$). The amount of solvent vapour in the chamber is dependent on the molar flux of solvent vapour produced at the liquid/vapour interface

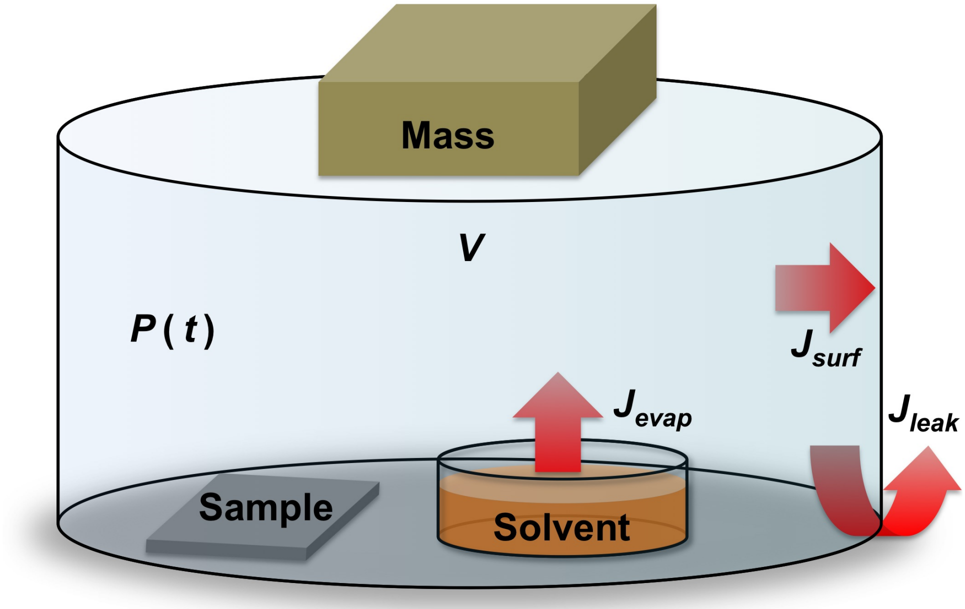

Figure 3.12: Sample placed under inverted container of volume V with a solvent having surface area A_{evap}. Solvent vapour pressure, $P(t)$, is a function of evaporation flux, J_{evap}; adsorption flux, J_{surf}; and leak flux, J_{leak}. A mass can be placed on the chamber to reduce solvent vapour leakage.

(J_{evap}), the molar flux of vapour adsorbing onto surfaces inside the chamber (J_{surf}), and the molar flux of vapour diffusing out of the chamber (J_{leak}). Given the liquid-vapour interfacial area (A_{evap}), inner chamber surface area (A_{surf}), and area for vapour leakage (A_{leak}), the time derivative for the number of solvent vapour molecules may be replaced to form Equation 3.4.3.

$$PV = nRT \tag{3.4.1}$$

$$\frac{dP}{dt}V = \frac{dn}{dt}RT \tag{3.4.2}$$

$$\frac{dP}{dt} = \frac{RT}{V}(A_{evap}J_{evap} - A_{surf}J_{surf} - A_{leak}J_{leak}) \tag{3.4.3}$$

A simple approximation describing the kinetics of solvent evaporation and condensation at the liquid/vapour interface is the Hertz-Knudsen formula.[52] Assuming uniform temperature and quasi-equilibrium conditions exist such that the condensation and evaporation constants at the interface are the same, the solvent flux at the liquid/vapour interface may be described as in Equation 3.4.4, where σ is the evaporation constant, N_A is Avogadro's number, m is the mass of one solvent molecule, and P_{sat} is the saturated vapour pressure of the solvent. As the equation suggests, the solvent flux at the liquid/vapour interface is composed of a forward evaporation rate, which is dependent on the solvent properties and temperature (P_{sat}); and a reverse condensation rate, which is dependent on the solvent partial pressure $P(t)$.

$$J_{evap} = \sigma\sqrt{\frac{N_A}{2\pi mRT}}(P_{sat} - P(t)) \tag{3.4.4}$$

A similar equation may also be applied to determine the flux of solvent molecules adsorbing onto the inner chamber surfaces. As is the case in Equation 3.4.4, the flux of solvent molecules on the chamber surface consists of both a forward adsorption term and a reverse desorption term. However, since a non-observable amount of solvent accumulates on the chamber surface during an anneal, the difference between adsorption and desorption rates is negligibly small. Thus, solvent sorption effects were ignored to simplify the model system.

The leak rate of solvent vapour from the chamber may be described by Fick's first law of diffusion (Equation 3.4.5). Rewriting the concentration gradient in terms of the solvent vapour pressure inside $[P(t)]$ and outside (P_{out}) the chamber, the equation can then be further reduced to Equation 3.4.7 by assuming $P_{out} = 0$.

$$\begin{aligned} J_{leak} &= -D_s \frac{dC(x)}{dx} && (3.4.5) \\ J_{leak} &= \frac{D_s}{RTx}(P(t) - P_{out}) && (3.4.6) \\ J_{leak} &= \frac{D_s}{RTx}P(t) && (3.4.7) \end{aligned}$$

Thus, by combining these parameters and simplifying assumptions with Equation 3.4.3, we obtain Equation 3.4.8. The equation may be further simplified by replacing many of the terms with constants representing the evaporation rate (k_{evap}) and the leak rate (k_{leak}).

$$\begin{aligned} \frac{dP}{dt} &= \frac{A_{evap}\sigma}{V}\sqrt{\frac{N_A RT}{2\pi m}}(P_{sat} - P(t)) - \frac{A_{leak}D_s}{Vx}P(t) && (3.4.8) \\ \frac{dP}{dt} &= \frac{1}{V}[k_{evap}(P_{sat} - P(t)) - k_{leak}P(t)] && (3.4.9) \\ k_{evap} &= A_{evap}\sigma\sqrt{\frac{N_A RT}{2\pi m}} \\ k_{leak} &= \frac{A_{leak}D_s}{x} \end{aligned}$$

Solving the differential equation with initial vapour pressure of 0 Pa, we obtain an equation describing the changes to vapour pressure over time (Equation 3.4.10).

$$\begin{aligned} P(t) &= \frac{P_{sat}}{1 + \frac{k_{leak}}{k_{evap}}}(1 - e^{-\frac{k_{evap}+k_{leak}}{V}t}) && (3.4.10) \\ P(t = 0) &= 0 \end{aligned}$$

During solvent annealing, the solvent vapour pressure initially increases rapidly; however, over time this increase slows down until a plateau is reached (Figure

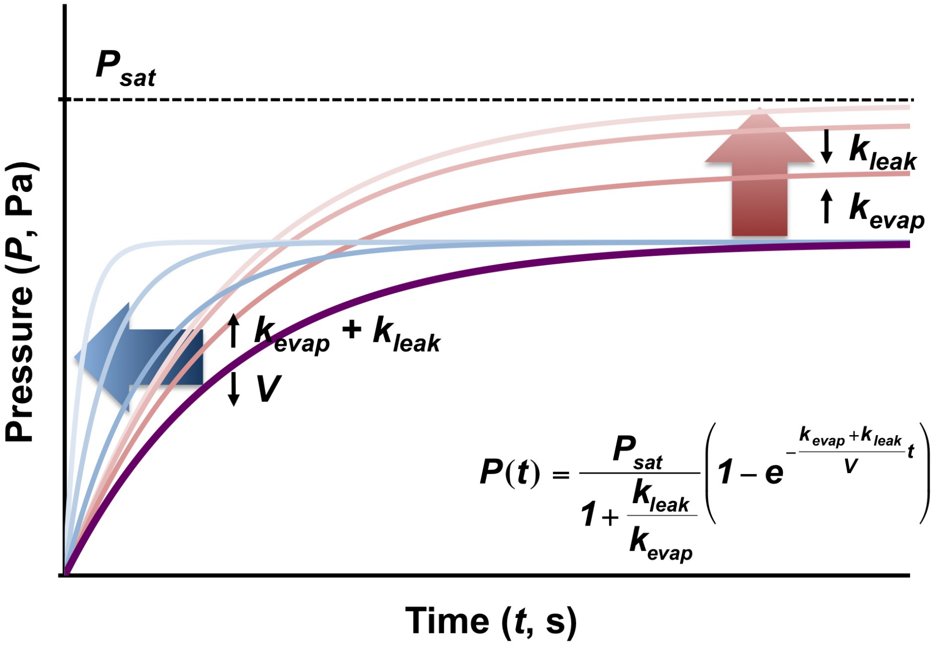

Figure 3.13: Graph of solvent vapour concentration over time. The plateau can be raised by increasing the surface area of the liquid/vapour interface with respect to the vapour leakage. The plateau can be reached sooner if the volume is small compared to the liquid/vapour interface and leakage rate.

3.13). The position of the plateau depends on the saturated vapour pressure (P_{sat}), as well as on the ratio between the leak rate and evaporation rate ($\frac{k_{leak}}{k_{evap}}$). For a higher plateau, evaporation rate may be increased with respect to the leak rate by increasing the liquid-vapour surface area of the solvent. However, a maximum in solvent vapour pressure occurs at the vapour pressure of the solvent when the evaporation rate greatly exceeds the leak rate. Equation 3.4.10 also predicts that as the volume of the chamber is increased with respect to evaporation rate and leak rate, the time required to attain the plateau becomes extended. Thus, if a desired vapour pressure is to be attained quickly for solvent annealing, it is advantageous to use a small chamber.

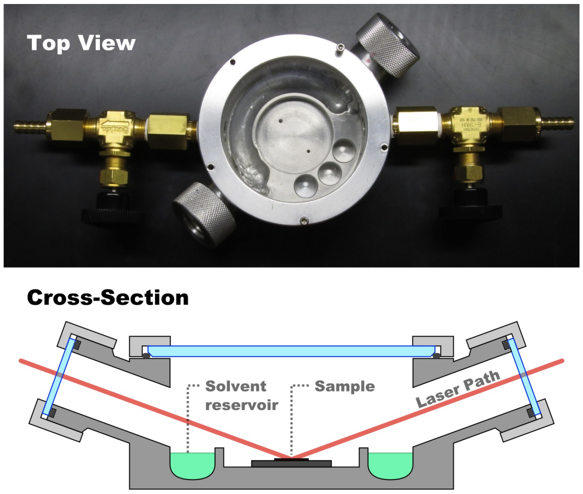

Figure 3.14: Aluminum annealing chamber designed for compatibility with *in situ* ellipsometry measurements. A glass window in the lid allows the samples to be viewed during an anneal procedure, and the extensions on either side are fitted with quartz windows to allow the polarized ellipsometer beam to pass through and reflect from the sample. The sample was placed in the center, and the wells around the perimeter were used to hold solvent. The chamber was sealed with Kalrez o-rings for minimum leakage of solvent vapour.

3.4.2 *In Situ* Ellipsometry

As the solvent vapour pressure increases inside the anneal chamber, some of the solvent infiltrates the polymer film, causing it to swell. Thus, by measuring the thickness of the film during the anneal, the volume fraction of solvent inside the film may be determined. A custom aluminum chamber was built to accommodate *in situ* ellipsometry measurements of film thickness to monitor film swelling (Figure 3.14). The BCP sample was placed in the centre recess of the chamber, and wells for holding solvent were drilled around the periphery of the recess. The surface areas for each of the wells were 1.3 cm^2, and the approximate surface area of the large crescent was 13 cm^2. The cylindrical extensions on either side of the chamber were tilted at 70° to the normal of the sample surface and fitted with quartz windows. This allowed the incident polarized laser beam to pass perpendicular to the quartz windows and reflect off the surface of the sample. A large glass window was also used as a lid on

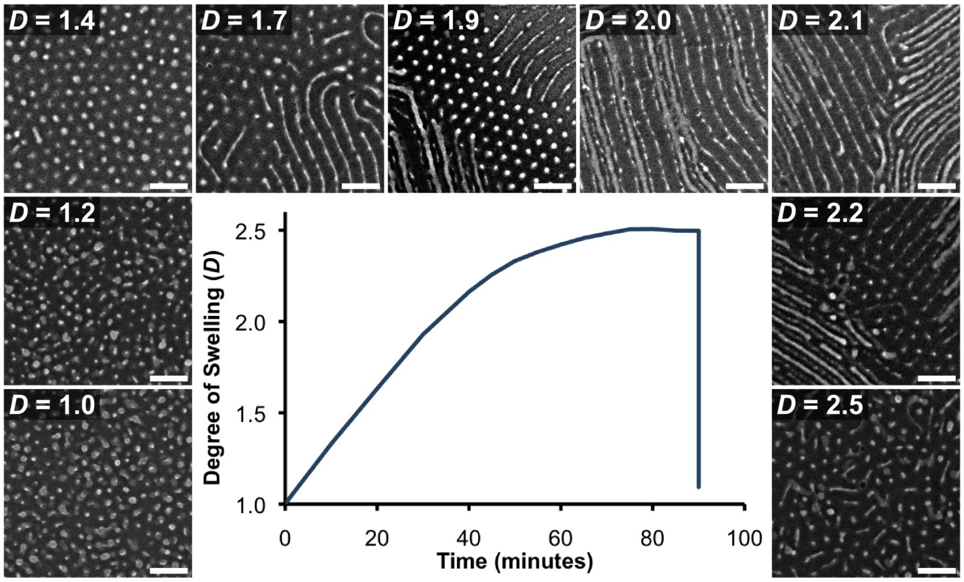

Figure 3.15: The time evolution of PS(50k)-*b*-P2VP(16.5k) film thickness throughout a typical 90 min annealing process for a h_o = 45 nm film swelled in neat THF. Representative SEM images of metallized structures templated from identical BCP films, swelled to various thicknesses, are found around the periphery. These SEM images depict the typical structures observed and their evolution during the anneal process. All scale bars are 100 nm.

top to facilitate sample alignment and also to allow *in situ* optical microscopy. Kalrez o-rings were used at all the windows to reduce unwanted solvent vapour leakage. A chamber volume of 160 mL allowed for solvent anneals to be complete within 90 min.

The anneal progress of a PS(50k)-*b*-P2VP(16.5k) film, with initial thickness h_o = 45 nm, was investigated in the presence of neat THF for a duration of 90 min. 1 mL of THF was placed into a well with a total liquid-vapour interfacial area of 1.3 cm^2. The o-ring for the lid of the chamber was also removed to increase solvent vapour leakage and prevent excessive swelling of the film. During a typical anneal, as shown in the graph in Figure 3.15, solvent was absorbed by the BCP film, causing a swelling behaviour that closely resembled the rise in vapour pressure described in Figure 3.13. Besides tracking the film thickness, the evolution of BCP structures as the film swelled was also investigated by subjecting identical film samples to identical annealing conditions before terminating the anneal at different target thicknesses (h_s). The chamber was then opened and immediately purged with air, causing the film to relax back to its original thickness. This relaxation process caused the BCP structures to collapse uniaxially perpendicular to the substrate plane.[53, 54] The samples were then metallized using the procedure described in Section 3.2 and characterized in the SEM.

To understand why the structures evolved with the degree of swelling ($D = h_s/h_o$), one must refer back to the phase diagram of confined BCP films (Figure 2.8). As shown in the phase diagram, the type of structure that self-assembles in the film depends not only on the volume fractions of the BCP, but also on the film thickness. During the solvent anneal, solvent molecules in the film plasticize the polymer network, increasing the mobility of polymer chains.[51] However, more importantly, the infiltration of solvent also leads to swelling of the film, which change the boundary conditions of the film, leading to the formation of different structures.[37] If the solvents are selective for one block over another, there is also a slight change in volume fraction. In this investigation, the volume fractions remain the same because the solvent THF is non-selective for both PS and P2VP. Thus, as D increases, the polymer chains become mobile, and depending on the thickness, different structures become thermodynamically favoured. In the case of PS(50k)-*b*-P2VP(16.5k), which has 75% PS and 25% P2VP volume fractions, the phase diagram predicts that hexagonal dot patterns ($C_\perp$) eventually give way to monolayer horizontal cylinders (C_1), which then pass through a short hexagonally close-packed perpendicular cylinder phase (SC), before transitioning into bilayer horizontal cylinders (C_2).

When the results in Figure 3.15 were compared to these predictions, many similarities were observed. For example, as the swell progressed, the disordered micelles in the as-cast films ($D = 1.0$) were slowly converted into quasi-hexagonal dot patterns ($D = 1.4$), and then into monolayer lines ($D = 1.7$). At this point, the results seemed to diverge from the model because instead of converting back into dot patterns (SC phase), the monolayer lines immediately transformed into bilayer lines ($D = 1.9$).[‡] However, it is known that certain thicknesses of film are more energetically favourable than others: namely, thicknesses promoting horizontal monolayer and bilayer line patterns.[35] Since D was sufficiently large, the polymer films had the mobility to reconstruct into terraced monolayer and bilayer cylinder regions to lower the total free energy of the system, thus largely bypassing the SC phase. At the interfaces between these terraces, however, the films must still gradually increase from a monolayer to a bilayer thickness. Thus, as shown at $D = 1.9$, hexagonally close-packed dot patterns from the SC phase were observed between the monolayer and bilayer line regions. As the swell continued, the ratio of bilayer to monolayer regions also increased to match the increase in average film thickness. This persisted until around $D = 2.0$, where only density-doubled line patterns were observed. At $D = 2.5$, the line patterns suddenly disappeared and were replaced by disordered micelles similar to those observed in as-cast films. At this point it was likely that the film had become so saturated with solvent that it began behaving like a dilute BCP solution. The subsequent purge step was then also too rapid for the polymers to reassemble into any reasonably ordered patterns.

For further evidence that the changes in the nanostructures described above were dependent on D, solvent anneals were performed under different swelling conditions and terminated at a target D of 1.4 and 2.0 (Figure 3.16). For very fast solvent anneals, 2 mL of neat THF was placed in the 13 cm^2 crescent of the aluminum chamber, and the anneal was carried out for 3 and 7 min to attain $D = 1.4$ and $D = 2.0$, respectively (Figures 3.16a,d). For moderately fast solvent anneals with 1 mL of THF in a well with surface area of 1.3 cm^2, the same D were attained in 15 min and 44 min, respectively (Figures 3.16b,e). For extremely slow anneals, 1 mL of a 34% (w/w) PS homopolymer solution in neat THF was used as the solvent in a well with 1.3 cm^2 surface area. According to Raoult's law, the vapour pressure of a component in solution is

---

[‡] These bilayer regions featured density-doubled lines, but many of the lower layer lines were missing. This was likely due to poor metallization, as will be described in Section 3.5.

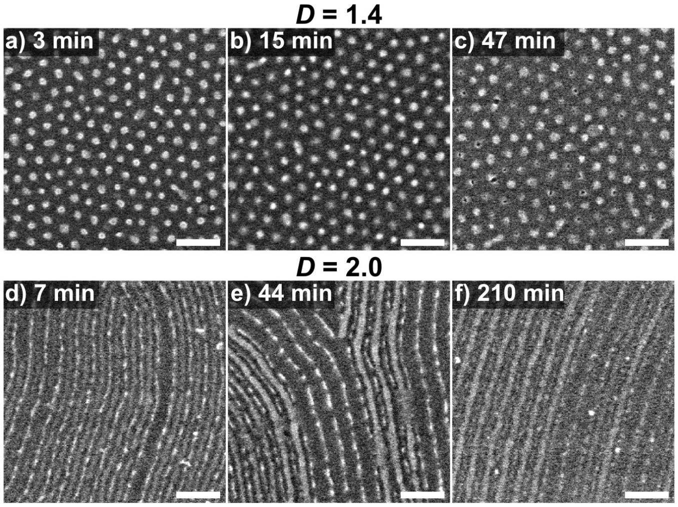

Figure 3.16: Identical BCP films thickness were swelled to the same target D for different durations by adjusting the solvent evaporation rate within the anneal chamber. The films were then metallized and examined in the SEM. Films swelled to $D = 1.4$ were annealed for 7 min (a), 15 min (b), or 45 min (c); while films swelled to $D = 2.0$ were annealed for 7 min (d), 44 min (e), or 210 min (f). All scale bars are 100 nm.

directly dependent on the mole fraction of the component present in solution. Thus, by forming a solution with PS homopolymer, the vapour pressure of THF inside the chamber was lowered. PS homopolymer was used due to the fact that the vapour pressure of PS homopolymer is negligibly low. Thus, unlike other cosolvents such as water, the PS would not interfere with the annealing process. The addition of the PS-diluted solvent caused the target D to be reached in 47 min and 210 min (Figures 3.16c,f). As demonstrated in the SEMs, dot patterns were observed in all three cases where $D = 1.4$. Similarly, line patterns were observed in all three cases where $D = 2.0$. This strongly suggested that the nanostructure morphologies were dependent more on the final thickness and D of the BCP film than on the anneal duration.

3.5 THF/Water Mixtures

As the sample films approached various degrees of swelling, dot patterns quickly gave way to both monolayer and density-doubled line patterns. The observed line patterns, as displayed in Figure 3.15, were often rough and discontinuous. Regions with density-doubled lines often alternated between two very distinct types of lines. The first group of lines were always narrow, rough, and highly discontinuous; while the second group of lines always appeared between lines from the first group, were always thicker and more continuous than the first group, but were often also missing.

It was hypothesized that these defects may have been a result of the metallization step. As demonstrated in Figure 3.7, P2VP block swelling during the metallization step results in surface perforations as cylinders in the film are swelled. If the upper cylindrical structures are too narrow, however, the swelling action causing them to pierce the PS overlayer may also redistribute them in such a way that they are no longer continuous. Even if enough P2VP is present in the upper layer cylinders, the swelling may cause some of the material to redistribute to the perforations, leading to narrower but taller line structures with access to the film surface. The bottom layer lines, on the other hand, are much harder to metallize than the top layer due to the fact that they have more PS insulating them from the outside metallic solution. However, as soon as a pathway from the ionic solution to the P2VP blocks is established, the entire cylinder becomes a channel for metal ions, and thus the entire line is metallized.

To address these problems, a small amount of water was added to the THF solvent. It was expected that since water is a solvent that is selective for P2VP blocks, this would lead to a swelling of the P2VP blocks during self-assembly, producing slightly wider line features. A 10:1 (v/v) ratio of THF to water mixture was used for annealing the PS-*b*-P2VP BCP films. 41 nm thick PS(50k)-*b*-P2VP(16.5k) BCP films were sealed in the aluminum chamber with 1 mL of the mixture placed inside the 13 cm^2 crescent for 90 min. The

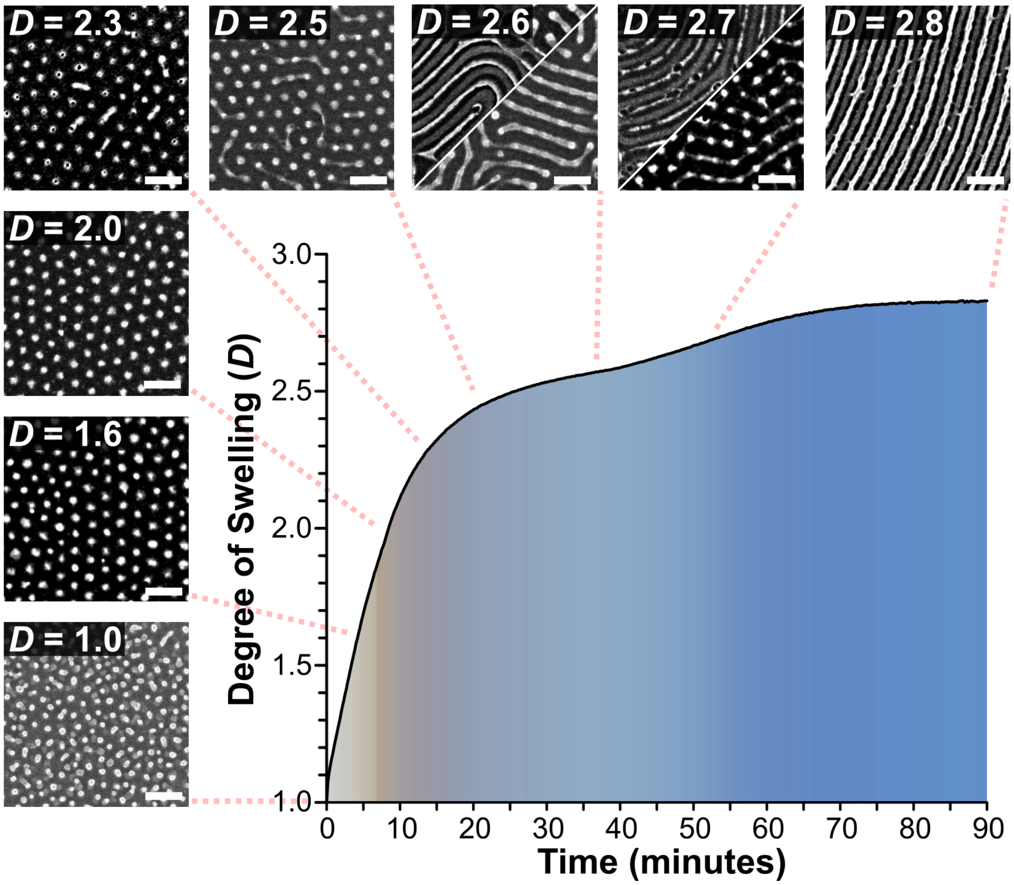

Figure 3.17: The time evolution of film thickness throughout a typical 90 min annealing process for a $h_o = 41$ nm film is shown in the plot, with the colour beneath the line matching the visually observed film colour at corresponding stages during the anneal. Representative SEM images of metallized structures templated from identical BCP films, swelled to various thicknesses, are found around the periphery. These SEM images depict the typical structures observed and their evolution during the anneal process. All scale bars are 100 nm. Reprinted with permission from ref. [1]. Copyright © 2011 American Chemical Society.

resulting swell curve and self-assembled structures were displayed in Figure 3.17. Similar to the anneals with neat THF, disordered patterns slowly became quasi-hexagonal dot patterns, which were consistently observed from $D = 1.6$ to $D = 2.5$. As the films continued to swell to $D = 2.7$, the dots connected with adjacent dots to form short line patterns with periodic bulges, similar to the "necks" observed in previous studies.[55] Density-doubled line patterns were also present at a few locations, but were not prevalent until $D = 2.8$, where they were observed uniformly covering the entire sample. The density-doubled lines that were produced in films swelled with the THF/water mixture were much more continuous and thicker than those from films annealed with neat THF. In addition, no lines templated by the lower layer cylinders were missing, suggesting that the addition of water during the solvent anneal also allowed the polymer films to metallize much more easily than films annealed with neat THF. Thus, this was the solvent used in producing the density-doubled line structures in Section 3.3.

3.6 Varying Film Thicknesses

To explore the dependence of structure morphology on the initial BCP film thickness, PS(50k)-*b*-P2VP(16.5k) samples with initial thicknesses of 33 nm and 52 nm were also annealed with the 10:1 THF and water mixture for up to 90 min and compared to annealed films initially 41 nm thick (Figure 3.18a-c). One major difference in the thinner 33 nm films was the presence of both monolayer line structures and density-doubled line structures on the same sample, suggesting that an insufficient amount of polymer was present for full density-doubled line coverage. One example of an interface between a monolayer line and density-doubled line region is displayed in the SEM in Figure 3.18a. AFM images at an interface before metallization and plasma (Figure 3.18d) showed that the density-doubled region was 14 nm higher than the monolayer region. For films with initial thicknesses of 52 nm, it was observed that the BCP structures were never able to advance beyond the dot

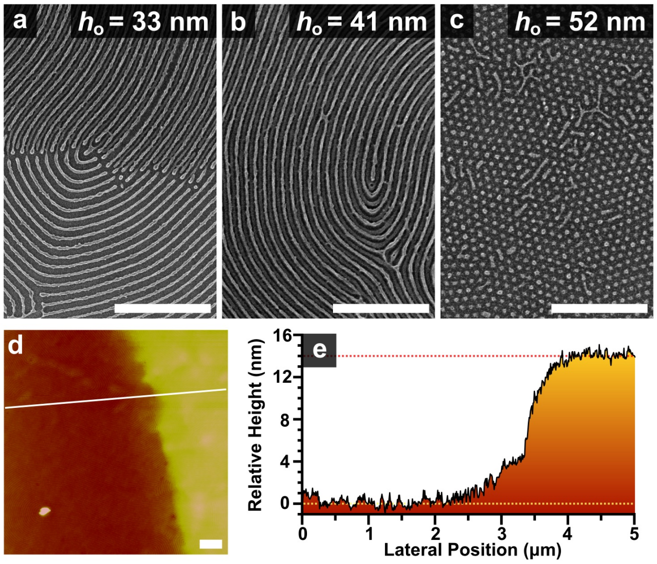

Figure 3.18: (a-c) SEM images of metallized structures templated from different initial BCP film thicknesses after annealing for 90 min with the 10:1 THF/water mixture. (d) 5 µm x 5 µm AFM image of a terrace edge in a h_o = 33 nm film after the anneal but before the metallization process. A line scan (position indicated by the white line) shows that the step height is approximately 14 nm (e). All scale bars are 500 nm. Adapted with permission from ref. [1]. Copyright © 2011 American Chemical Society.

phases within 90 min. These observations indicated that the initial thickness of a film also affects the ability for density-doubled lines to be formed. Thus, for density-doubled lines to be produced in a homogeneous fashion over the entire surface, there exists an ideal initial film thickness of around 41 nm for this particular BCP.

3.7 Temperature and Film Swelling

Both the swell curves displayed in Figures 3.15 and 3.17 were similar in shape to the solvent vapour pressure curves described in Figure 3.13. Upon closer inspection, however, it was observed that the curves also contained some small peaks and valleys that were not predicted in the vapour pressure curves. These

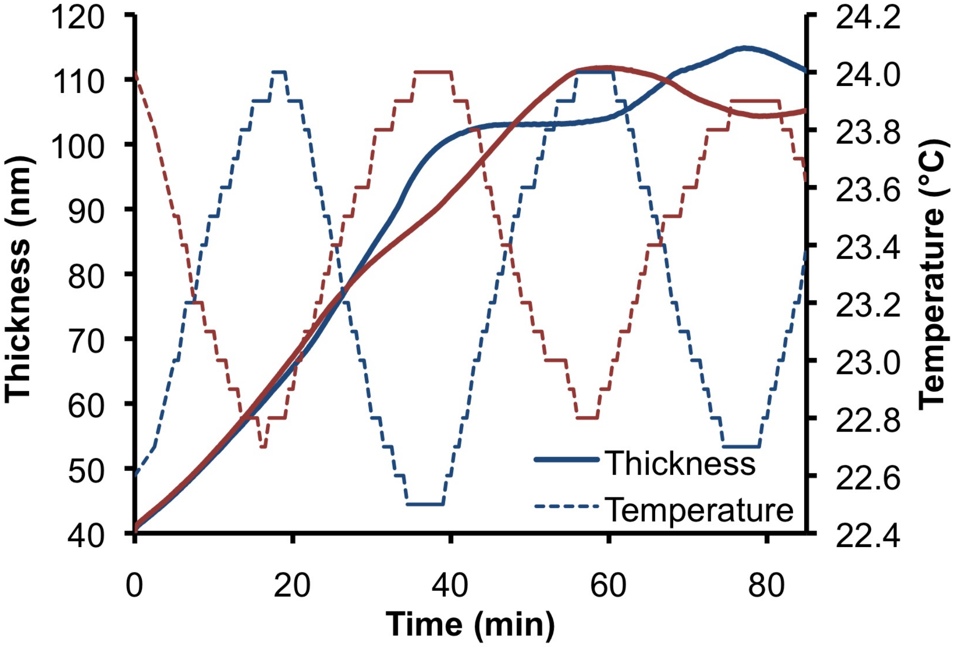

Figure 3.19: Two identical BCP samples were solvent annealed in identical neat THF vapour conditions while the temperature fluctuations within the room were monitored. The first sample (blue) started at a low point in the temperature cycle, while the second sample (red) started at a high point in the temperature cycle. The film thicknesses (solid lines) and measured temperatures (dotted lines) of both samples were then plotted together for comparison.

variations appeared at unpredictable times and were not repeatable from sample to sample. After some investigation, it was observed that the room temperature oscillated in 40 min cycles within a temperature range of 1.5 °C.

To determine whether these temperature fluctuations were the source of the variations in the curves, two identical 40 nm BCP films were annealed in identical solvent (neat THF) conditions, except that they began at different points in the temperature cycle. A solvent anneal was initiated at a low point in the cycle (see blue lines in Figure 3.19) while the ellipsometer was monitoring the film thickness and a thermometer was monitoring the room temperature. As shown in the figure, the peaks in the swelling curve coincided with the lower temperatures in the cycle, while the valleys in the curve was found to coincide with higher room temperatures. This effect became more pronounced as the film grew thicker, likely due to the increased solvent content in the film. A second anneal on an identical sample was then initiated at a high point in the temperature cycle (see red lines in Figure 3.19). The same relations described with the blue sample were observed in the red samples except that the locations of the red peaks were out-of-phase with the blue peaks. These results strongly suggest that the culprit behind these variations in swelling was the slight temperature fluctuations in the room. Thus, the temperature during a solvent anneal has a significant impact on the swelling behaviour of BCP films. To improve the repeatability of solvent anneals, the anneal chamber must therefore be insulated from the effects of the oscillating room temperature.

3.8 Conclusions

By using the three-dimensional arrangement of BCP templated bilayer cylinders, metal lines may be patterned at double the density normally possible if only a monolayer of cylinders was used. *In situ* film measurements during the solvent anneal revealed that the solvent film swells to different thicknesses during the anneal. By removing the samples at specific points in the anneal, it was observed that the BCP structures slowly evolved from quasi-hexagonal patterns to the desired density-doubled patterns. Through the addition of water to the anneal solvent, issues such as missing lines or line discontinuities were minimized, allowing for very well-defined metal lines to be produced. Control over the initial film thickness and temperature was also critical for repeatably producing the desired density-doubled patterns across the sample. Thus, by controlling parameters such as h_o, D, solvent composition, and temperature, this technique holds great promise for pushing the limits of feature density in BCP nanopatterning.

References

[1] N. L.-Y. Wu *et al.*, "Density doubling of block copolymer templated features," *Nano Lett.*, vol. 12, no. 1, pp. 264–268, 2011.

[2] S. Darling, "Directing the self-assembly of block copolymers," *Progress in Polymer Science*, vol. 32, no. 10, pp. 1152–1204, 2007.

[3] J. Bang *et al.*, "Block copolymer nanolithography: Translation of molecular level control to nanoscale patterns," *Advanced Materials*, vol. 21, no. 47, pp. 4769–4792, 2009.

[4] H.-C. Kim, S.-M. Park, and W. D. Hinsberg, "Block copolymer based nanostructures: Materials, processes, and applications to electronics," *Chemical Reviews*, vol. 110, no. 1, pp. 146–177, 2010.

[5] K. Galatsis *et al.*, "Patterning and templating for nanoelectronics," *Advanced Materials*, vol. 22, no. 6, pp. 769–778, 2010.

[6] D. J. Milliron *et al.*, "Solution-phase deposition and nanopatterning of GeSbSe phase-change materials," *Nature Materials*, vol. 6, no. 5, pp. 352–356, 2007.

[7] R. Ruiz, E. Dobisz, and T. R. Albrecht, "Rectangular patterns using block copolymer directed assembly for high bit aspect ratio patterned media," *ACS Nano*, vol. 5, no. 1, pp. 79–84, 2011.

[8] T. Thurn-Albrecht *et al.*, "Ultrahigh-density nanowire arrays grown in self-assembled diblock copolymer templates," *Science*, vol. 290, no. 5499, pp. 2126–2129, 2000.

[9] K. Naito *et al.*, "2.5-inch disk patterned media prepared by an artificially assisted self-assembling method," *IEEE Transactions on Magnetics*, vol. 38, no. 5, pp. 1949–1951, 2002.

[10] K. W. Guarini *et al.*, "Low voltage, scalable nanocrystal flash memory fabricated by templated self assembly," in *IEEE International Electron Devices Meeting 2003, Technical Digest.* Piscataway, NJ: IEEE, 2003, pp. 22.2.1–22.2.4.

[11] C. T. Black, "Self-aligned self assembly of multi-nanowire silicon field effect transistors," *Applied Physics Letters*, vol. 87, no. 16, pp. 163 116(1–3), 2005.

[12] A. M. Urbas *et al.*, "Tunable block copolymer/homopolymer photonic crystals," *Advanced Materials*, vol. 12, no. 11, pp. 812–814, 2000.

[13] A. M. Urbas *et al.*, "Bicontinuous cubic block copolymer photonic crystals," *Advanced Materials*, vol. 14, no. 24, pp. 1850–1853, 2002.

[14] M. Arnold *et al.*, "Activation of integrin function by nanopatterned adhesive interfaces," *ChemPhysChem*, vol. 5, no. 3, pp. 383–388, 2004.

[15] N. Walter *et al.*, "Cellular unbinding forces of initial adhesion processes on nanopatterned surfaces probed with magnetic tweezers," *Nano Letters*, vol. 6, no. 3, pp. 398–402, 2006.

[16] A. N. Semenov, "Contribution to the theory of microphase layering in block-copolymer melts," *Soviet Physics JETP*, vol. 61, no. 4, pp. 733–742, 1985.

[17] A. C. Edrington *et al.*, "Polymer-based photonic crystals," *Advanced Materials*, vol. 13, no. 6, pp. 421–425, 2001.

[18] M. B. Runge and N. B. Bowden, "Synthesis of high molecular weight comb block copolymers and their assembly into ordered morphologies in the solid state," *Journal of the American Chemical Society*, vol. 129, no. 34, pp. 10 551–10 560, 2007.

[19] E. Kim *et al.*, "Directed assembly of high molecular weight block copolymers: Highly ordered line patterns of perpendicularly oriented lamellae with large periods," *ACS Nano*, vol. 7, no. 3, pp. 1952–1960, 2013.

[20] M. D. Whitmore and J. Noolandi, "Self-consistent theory of block copolymer blends: Neutral solvent," *The Journal of Chemical Physics*, vol. 93, no. 4, pp.

2946–2955, 1990.

[21] M. B. Runge *et al.*, “Investigation of the assembly of comb block copolymers in the solid state,” *Macromolecules*, vol. 41, no. 20, pp. 7687–7694, 2008.

[22] J. Rzayev, “Synthesis of polystyrene-polylactide bottlebrush block copolymers and their melt self-assembly into large domain nanostructures,” *Macromolecules*, vol. 42, no. 6, pp. 2135–2141, 2009.

[23] Y. Xia *et al.*, “Efficient synthesis of narrowly dispersed brush copolymers and study of their assemblies: The importance of side chain arrangement,” *Journal of the American Chemical Society*, vol. 131, no. 51, pp. 18 525–18 532, 2009.

[24] “International technology roadmap for semiconductors 2011 edition,” Semiconductor Industry Association, San Jose, CA, Tech. Rep., 2011. [Online]. Available: http://www.itrs.net

[25] F. S. Bates and G. H. Fredrickson, “Block copolymer thermodynamics — Theory and experiment,” *Annual Review of Physical Chemistry*, vol. 41, pp. 525–557, 1990.

[26] E. Helfand, “Block copolymers, polymer-polymer interfaces, and the theory of inhomogeneous polymers,” *Accounts of Chemical Research*, vol. 8, no. 9, pp. 295–299, 1975.

[27] Y. Zhao, E. Sivaniah, and T. Hashimoto, “SAXS analysis of the orderdisorder transition and the interaction parameter of polystyrene-*block*-poly(methyl methacrylate),” *Macromolecules*, vol. 41, no. 24, pp. 9948–9951, 2008.

[28] E. W. Cochran, D. C. Morse, and F. S. Bates, “Design of ABC triblock copolymers near the ODT with the random phase approximation,” *Macromolecules*, vol. 36, no. 3, pp. 782–792, 2003.

[29] K. H. Dai and E. J. Kramer, “Determining the temperature-dependent Flory interaction parameter for strongly immiscible polymers from block copolymer segregation measurements,” *Polymer*, vol. 35, no. 1, pp. 157–161, 1994.

[30] Y. S. Jung *et al.*, “A path to ultranarrow patterns using self-assembled lithog-

raphy," *Nano Letters*, vol. 10, no. 3, pp. 1000–1005, 2010.

[31] J. W. Jeong *et al.*, "Highly tunable self-assembled nanostructures from a poly(2-vinylpyridine-*b*-dimethylsiloxane) block copolymer," *Nano Letters*, vol. 11, no. 10, pp. 4095–4101, 2011.

[32] J. D. Cushen *et al.*, "Thin film self-assembly of poly(trimethylsilylstyrene-*b*-d,l-lactide) with sub-10 nm domains," *Macromolecules*, vol. 45, no. 21, pp. 8722–8728, 2012.

[33] J. D. Cushen *et al.*, "Oligosaccharide/silicon-containing block copolymers with 5 nm features for lithographic applications," *ACS Nano*, vol. 6, no. 4, pp. 3424–3433, 2012.

[34] J. E. Poelma *et al.*, "Cyclic block copolymers for controlling feature sizes in block copolymer lithography," *ACS Nano*, vol. 6, no. 12, pp. 10 845–10 854, 2012.

[35] H. P. Huinink *et al.*, "Asymmetric block copolymers confined in a thin film," *The Journal of Chemical Physics*, vol. 112, no. 5, pp. 2452–2462, 2000.

[36] H. P. Huinink *et al.*, "Surface-induced transitions in thin films of asymmetric diblock copolymers," *Macromolecules*, vol. 34, no. 15, pp. 5325–5330, 2001.

[37] A. Knoll *et al.*, "Phase behavior in thin films of cylinder-forming block copolymers," *Physical Review Letters*, vol. 89, no. 3, pp. 35 501(1–4), 2002.

[38] A. Knoll, R. Magerle, and G. Krausch, "Phase behavior in thin films of cylinder-forming ABA block copolymers: Experiments," *The Journal of Chemical Physics*, vol. 120, no. 2, pp. 1105–1116, 2004.

[39] G. E. Stein *et al.*, "Layering transitions in thin films of spherical-domain block copolymers," *Macromolecules*, vol. 40, no. 7, pp. 2453–2460, 2007.

[40] J. Y. Cheng *et al.*, "Integration of polymer self-assembly for lithographic application," *Proceedings of SPIE*, vol. 6921, pp. 92 127(1–8), 2008.

[41] Y. S. Jung and C. A. Ross, "Orientation-controlled self-assembled nanolithography using a polystyrene-polydimethylsiloxane block copolymer," *Nano Letters*,

vol. 7, no. 7, pp. 2046–2050, 2007.

[42] G. R. Whittell *et al.*, "Self-assembly and applications of polyferrocenylsilane block copolymers," in *Complex Macromolecular Architectures: Synthesis, Characterization, and Self-Assembly*, N. Hadjichristidis *et al.*, Eds. Singapore: John Wiley & Sons, 2011, pp. 491–526.

[43] J. Chai *et al.*, "Assembly of aligned linear metallic patterns on silicon," *Nature Nanotechnology*, vol. 2, no. 8, pp. 500–506, 2007.

[44] J. Chai and J. M. Buriak, "Using cylindrical domains of block copolymers to self-assemble and align metallic nanowires," *ACS Nano*, vol. 2, no. 3, pp. 489–501, 2008.

[45] Y.-C. Tseng *et al.*, "Enhanced block copolymer lithography using sequential infiltration synthesis," *Journal of Physical Chemistry C*, vol. 115, no. 36, pp. 17 725–17 729, 2011.

[46] W. Kern, Ed., *Handbook of Semiconductor Wafer Cleaning Technology: Science, Technology, and Applications.* Westwood, NJ: Noyes Publications, 1993.

[47] G. Coulon *et al.*, "Surface-induced orientation of symmetric, diblock copolymers: A secondary ion mass-spectrometry study," *Macromolecules*, vol. 22, no. 6, pp. 2581–2589, 1989.

[48] A. Loxley and B. Vincent, "Equilibrium and kinetic aspects of the pH-dependent swelling of poly(2-vinylpyridine-*co*-styrene) microgels," *Colloid and Polymer Science*, vol. 275, no. 12, pp. 1108–1114, 1997.

[49] A. Fernández-Nieves *et al.*, "Charge controlled swelling of microgel particles," *Macromolecules*, vol. 33, no. 6, pp. 2114–2118, 2000.

[50] D. Rio *et al.*, "Study on line edge roughness for electron beam acceleration voltages from 50 to 5 kV," *Journal of Vacuum Sciences & Technology B*, vol. 27, no. 6, pp. 2512–2517, 2009.

[51] J. Crank and G. S. Park, *Diffusion in Polymers.* Oxford, UK: Academic Press Inc., 1968.

[52] J. Barrett and C. Clement, "Kinetic evaporation and condensation rates and their coefficients," *Journal of Colloid and Interface Science*, vol. 150, no. 2, pp. 352–364, 1992.

[53] J. K. Bosworth *et al.*, "Control of self-assembly of lithographically patternable block copolymer films," *ACS Nano*, vol. 2, no. 7, pp. 1396–1402, 2008.

[54] M. Y. Paik *et al.*, "Reversible morphology control in block copolymer films *via* solvent vapor processing: An *in situ* GISAXS study," *Macromolecules*, vol. 43, no. 9, pp. 4253–4260, 2010.

[55] M. Konrad *et al.*, "Volume imaging of an ultrathin SBS triblock copolymer film," *Macromolecules*, vol. 33, no. 15, pp. 5518–5523, 2000.

4

Tuning of Silica Bilayered Structures

4.1 Introduction

Silicon dioxide is an important material in nanotechnology, not only because it is cheap and ubiquitous, but also because of its many desirable properties. For example, thin film silica has been and remains a key component in integrated circuit technology almost since the inception of the semiconductor industry. It is used for dopant masks, surface protectors and passivators, component isolators, and gate insulators for metal-oxide-semiconductor devices.[2, 3] Several reasons for its popular usage include the ease of forming an amorphous oxide on silicon wafers with excellent insulating properties, high electrical breakdown, and mechanical stability at normal operating temperatures. Films of silica can be deposited through a high-temperature thermal oxidation process, or through the lower temperature plasma-enhanced chemical vapour deposition.[4] These films are then converted into nanoscale patterns using top-down processing techniques such as photolithography. Silica may also be patterned through spin on glass resists such as HSQ that are then subsequently patterned *via* EBL.

In contrast to the top-down processing approach, the bottom-up approach to

---

The material in this chapter is based on published work from [1]. In this work, Dr. Kenneth Harris and Dr. Jillian Buriak contributed to useful discussions. Jeffrey Murphy and Andrew Wong also facilitated the investigation by developing a program to automate the collection of *in situ* ellipsometry measurements.

nanosilica production relies on the self-assembly of silica precursors to form ordered nanostructures. One field in self-assembled silica nanostructures that has attracted considerable interest is the use of mesoporous silica nanoparticles (MSNs) for disease diagnosis and therapy.[5–9] MSNs are solid silica nanoparticles with hundreds of hollow channels, and have been proposed as promising candidates for carriers of therapeutic agents for diabetes, inflammation, cancer, and bone/tendon tissue engineering. They are produced through the condensation of silica precursors around self-assembled surfactant templates. Besides the synthesis of MSNs, the bottom-up approach has also been used to create inverse opal silica structures.[10, 11] Silica precursors are allowed to infiltrate and condense around films of colloidal latex spheres. Subsequent removal of these latex spheres produces inverse opal silica structures that may then be used for photonics, sensing, tissue engineering, and catalysis.

4.1.1 PS-*b*-PDMS Block Copolymer Patterning

One other path towards silica nanopattern fabrication through self-assembly is the use of silica-based BCPs. PS-*b*-PDMS is one such silicon-based polymer that would be useful for nanofabrication purposes. One advantage of this polymer is its high χ parameter ($\chi_{\mathrm{PS-PDMS}} = 0.27$ compared to $\chi_{\mathrm{PS-P2VP}} = 0.18$ at room temperature),[12, 13] which allows it to self-assemble into very small, well-defined structures with lower LER.[14, 15] In addition to this, due to the differences in block compositions, there is also a very high etch contrast between the two blocks if plasma etching is used. Thus, very clean and distinct structures may be observed after the polymer is etched.

One recent innovative application of PS-*b*-PDMS is the formation of phase-change memory devices.[16] Lamellar patterns or hexagonally-packed silica nanodot patterns with 6 to 18 nm diameters were self-assembled on electrodes using PS-*b*-PDMS polymers (Figure 4.1). These structures were then treated with a plasma etch, and could then be electrically stimulated either through the deposition of an electrode layer or by probing by a conducting AFM tip.

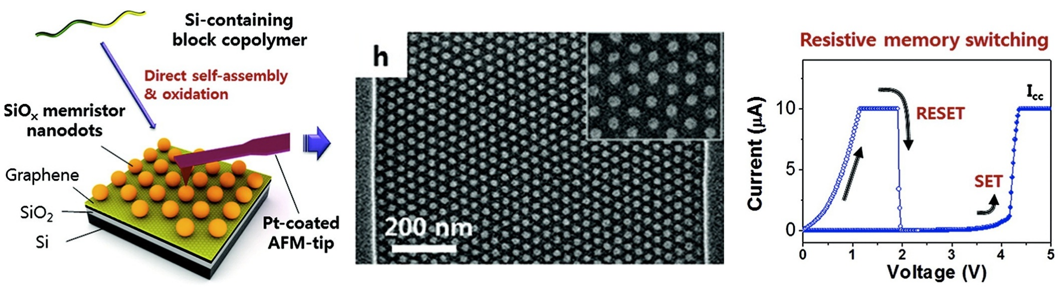

Figure 4.1: Hexagonally-packed SiO$_x$ nanodots templated by PS-*b*-PDMS were used as memristor devices. Reprinted with permission from ref. [16]. Copyright © 2012 American Chemical Society.

In both cases, memristive switching behaviour with current-voltage hysteresis loops were observed. In the hexagonally-packed patterns, reset and set voltages were found to be 2.0 and 4.6 V, respectively. These properties remained after over 80 cycles, and the signals were retained for over 10^4 s. This same group also used various PS-*b*-PDMS polymers to tune the properties of $Ge_2Sb_2Te_5$ (GST) based phase-change memory devices.[17] By inserting a self-assembled PS-*b*-PDMS film between the GST and the heating element of the device, the power consumption of the device could be minimized.

4.1.2 Density Doubling of PS-*b*-PDMS Structures

Bilayers of PS-*b*-PDMS cylinders have been studied in the past by Tavakkoli *et al.*,[18] who showed that by using densely-packed pre-patterned posts, these bilayered lines could be coaxed into overlapping arrays of lines intersecting at controllable angles. These results suggest that multilayered BCP films could provide promising solutions to patterning problems such as increasing feature densities or interconnecting components in precisely controlled directions. In this chapter, the process of density-doubling introduced in the Chapter 3 is applied to bilayers of cylinder-forming PS-*b*-PDMS to generate closely-spaced silica (SiO$_x$) lines, as outlined in Figure 4.2. The method is almost identical except the metallization step is avoided, since the PDMS may be directly converted into SiO$_x$ upon exposure to plasma treatment.[16, 19] As films of

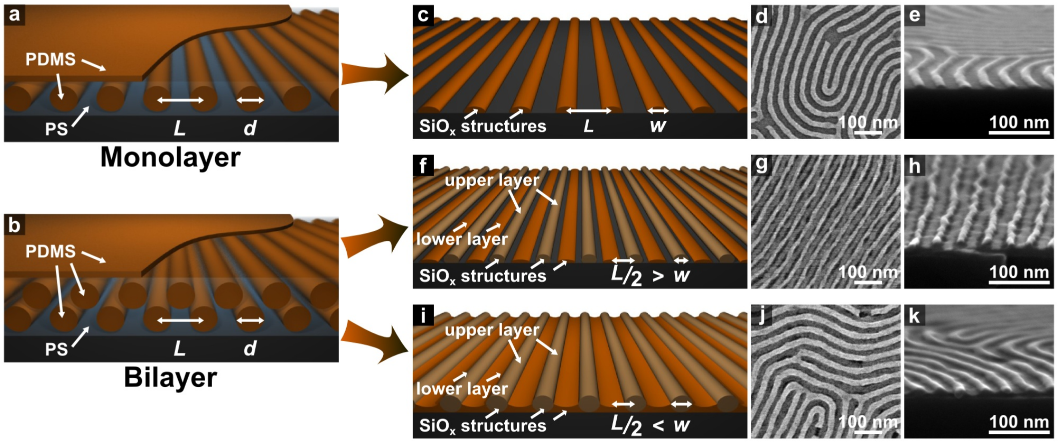

Figure 4.2: Schematics of self-assembled PS-*b*-PDMS monolayer (a) and bilayer (b) cylinders after solvent annealing: PDMS cylinders (characteristic spacing L and cylinder diameter d) are surrounded by a PS matrix and a thin PDMS surface layer on top. After plasma treatment, the cylinders become line patterns, as shown in the plan view and cross section SEM images to the right. (c-e) Lines patterned from monolayers of PDMS cylinders have line pitch L and line width w. (f-h) Ideal lines patterned from PS-*b*-PDMS bilayers are separated and have line pitch $L/2$ and line width $w < L/2$. (i-k) Lines are not neatly separated and may overlap when $w > L/2$. Reprinted with permission from ref. [1]. Copyright © 2013 American Chemical Society.

PS-*b*-PDMS films are solvent annealed in THF vapour, they self-assemble into ordered regions of monolayers (Figure 4.2a), bilayers (Figure 4.2b), and under certain conditions, even trilayers of cylinders on each sample (quantification *vide infra*). Monolayer regions of PDMS cylinders are converted, through plasma-treatment, into silica lines with pitch L and width w (Figure 4.2c-e). After plasma treatment of the bilayer regions, silica lines derived from the upper PDMS cylinders are deposited onto the substrate between silica structures from the lower layers. The resulting structure consists of silica lines with a pitch of $L/2$ (Figure 4.2f-h).

Without process optimization, bilayer regions of PDMS cylinders produce SiO$_x$ line arrays with significant overlap between the lines that originate from the upper and lower layers of PDMS cylinders, as shown schematically in Figure 4.2i and in the SEM images in Figures 4.2j,k. In order to attain sufficient separation of the SiO_x lines as observed in Figure 4.2f, fine control over the line dimensions such as line width and pitch is essential. In this chapter, control over the line width and pitch is demonstrated through tailoring of surface brush layers, polymer film composition, annealing conditions and plasma etch parameters. After the effects of each of these parameters are understood, it is possible to independently control parameters such as line width and pitch to produce distinct density-doubled silica lines from bilayer PDMS cylinders. In addition to this, strategies for maximizing bilayer structures across the entire sample are explored.

4.2 Experimental

4.2.1 Materials

Silicon (100) wafers (prime grade, 100 mm diameter, n-type, phosphorous-doped, $\rho = 5$–$10\ \Omega\cdot$cm) were purchased from University Wafer. 38% HCl (aq) and 30% NH_4OH (aq) were obtained from J. T. Baker; methanol, acetone, isopropanol, hexane, and 30% H_2O_2 were obtained from Fisher Scientific; heptane, tetrahydrofuran (THF), and toluene were obtained from Caledon Laboratories Ltd. Ultrapure water with $\rho > 18$ M$\Omega\cdot$cm from a Millipore Milli-Q system was used for all experiments. Cylinder-forming PS(31k)-*b*-PDMS(14.5k), and OH-terminated PS(10k) and PDMS(5k) homopolymers were obtained from Polymer Source. PS(192k) homopolymer was obtained from Sigma Aldrich.

4.2.2 Nanopattern Fabrication

Silicon wafers were diced into 1 × 1 cm squares and cleaned using standard RCA I and RCA II cleaning procedures as described in Chapter 3.[20] Casting solutions of PS-*b*-PDMS, PS(10k), PS(192k) and their blends were made by dissolving these polymers in toluene. Similar casting solutions of PDMS(5k) were made except with heptane as the solvent. For samples with a brush layer, the OH-terminated homopolymer solutions were spin cast onto the silicon substrates and placed in the vacuum oven at 130 °C for 2 h. After the grafting process was complete, the excess polymer was washed off with hexane, acetone, and isopropanol. BCP solutions were then spin cast onto the silicon substrates to create a thin film, and the resulting film was then either thermally or solvent annealed. In thermal annealing, the sample was heated on a heating block for a specified time and temperature. Solvent annealed films were placed in the aluminum chamber described in Chapter 3 to allow monitoring of the film swelling. This was done using the L116S ellipsometer from Gaertner Scientific as described before. To isolate the samples from the fluctuations in room temperature, the chamber was insulated with bubble wrap and placed on a Teflon sheet. 1 mL of THF with an exposed surface area of 2.6 cm^2 was then deposited inside the chamber before being sealed. Once the desired swelling ratio was obtained, the chamber was opened and immediately purged with air to rapidly (<1 s) relax the swelled film to its original thickness. The kinetically trapped film was then transferred to a Plasmalab µEtch reactive ion etcher for two steps of plasma etching. Unless otherwise noted, the first step used 100 mTorr of CF_4 at 50 W RF power for 10 s, and this was immediately followed by the second step using 100 mTorr of O_2 at 30 W RF power for 30 s. The samples were then analysed using SEM or optical microscopy.

4.3 Tuning of Line Dimensions

As shown in Figure 4.2, well-spaced, density-doubled line patterns require the tuning and optimization of various processing parameters. To attain these well-spaced density-doubled line patterns, the anneal conditions, BCP film composition, surface brush layers, and plasma treatment were all optimized. To evaluate the success of each optimization strategy in producing well-separated, density-doubled lines, SEM images of the samples after their

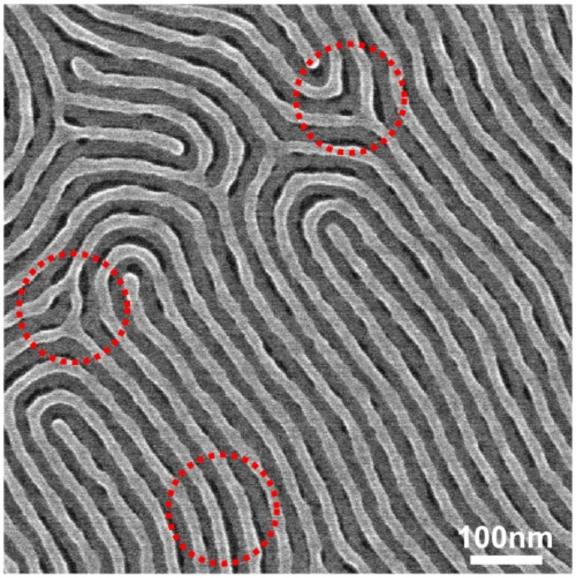

Figure 4.3: Lines originating from upper layer cylinders could be identified by their occlusion of one edge or of a junction found in the adjacent structures.

self-assembly and plasma treatment were acquired using a Hitachi S-4800 SEM. SEM images of these samples revealed that both monolayer and bilayer line regions were present in nearly all of the samples. Lines in bilayer regions could be identified as originating from the top layer of PDMS cylinders if they partially occluded one side of an adjacent line or defects/junctions in the underlying layer (Figure 4.3). As in Chapter 3, the $\mathrm{SiO_x}$ lines templated from the upper layer of PDMS cylinders were consistently observed to be narrower and brighter than their lower layer counterparts when imaged using SEM.

4.3.1 Line Metric Definitions

In the analysis of SEM images, it was important to identify key parameters that describe the efficacy of a particular method in producing the desired density doubled lines. In monolayer regions, these key parameters include the line width (w) and the characteristic cylinder spacing (L) of the polymer. A Quartz PCI imaging program was used for measuring both the w and L of lines

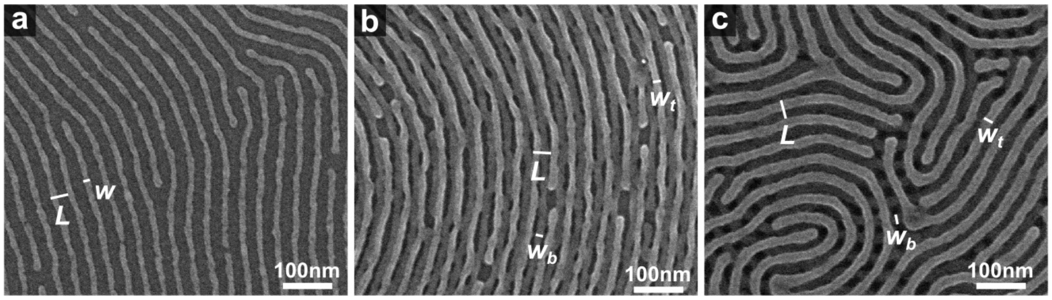

Figure 4.4: Line structures templated from monolayer (a) and bilayer (b,c) cylinder regions. The white lines indicate example measurements of monolayer line pitch (L) and width (w), as well as bilayer top (w_t) and bottom (w_b) line widths.

in the SEM images. Line width measurements were obtained by measuring the distance from one side of the line to the other as shown in Figure 4.4a. The average and standard deviation of at least 40 such measurements were taken from at least 2 SEM images from different regions in the sample. Line pitch was measured from the left side of one line to the left side of an adjacent line, and similar average and standard deviation values were extracted from the images.

Line dimensions of bilayer regions could be measured as well, although these measurements proved to be more difficult as lines tended to be wavier and were found to touch or occlude each other in many places. Measurements could only be made at positions where sharp contrast delineated line edges (Figure 4.4b). The line width measurements of lines in the top and bottom layers were denoted as w_t and w_b, respectively, and were measured similar to the monolayer line widths. Line pitch was measured from the left edge of a top layer line to the left edge of an adjacent top layer line. Top layer lines were used rather than bottom layer lines due to edge occlusion of the bottom layer lines. The edge occlusions placed an especially problematic limitation on the measurement of density-doubled regions of thick lines, because specific defect regions with intersecting top and bottom layer lines (Figure 4.4c) were required for the measurement of lower layer line width, w_b. Restricting the measurement positions to these locations with specific attributes may lead to measurements that do not necessarily reflect the true average line width and pitch for the entire sample. Thus, due to the edge occlusions and inherent waviness of bilayer lines, a comparison of the bilayer line properties between samples was extremely difficult.

One parameter that was especially useful in describing the overlap of bottom layer lines by top layer lines was the monolayer fill ratio (F). The monolayer fill ratio, which is defined by Equation 4.3.1, describes the fraction of surface occupied by silica line features templated by monolayer cylinders. As shown in Figure 4.5a, a fill ratio of $F = 0.50$ describes lines separated by spaces equal to the line width. If SiO_x lines templated from a monolayer region of PDMS cylinders have $F = 0.50$, then lines formed from a bilayer of PDMS cylinders on the same sample will consist of silica lines in contact with one another, with no visible line separation and no overlap (Figure 4.5c). If a fill ratio of $F > 0.50$ is observed in a monolayer region, the corresponding bilayer regions will display lines originating from the upper PDMS cylinders overlapping with lines originating from the lower layer of PDMS cylinders (Figure 4.5b). Finally, if a fill ratio $F < 0.50$ is observed in a monolayer region, the corresponding bilayer regions will display density doubled lines separated by distinct gaps (Figure 4.5d).

$$F = \frac{w}{L} \tag{4.3.1}$$

It should be noted that these calculations are considered to be ideal, since it is assumed that silica lines originating from bilayer regions have the same L and w as those found in monolayer regions. In practice, while L remains the same, lines templated from the lower layer of bilayer cylinders tend to be wider than lines templated from the upper layer, and both tend to be wider than lines templated from a monolayer. Also, as the fill ratio increased, increased line occlusion or contact between adjacent lines prevented reliable measurements of w, L, and F from being made. Because of these challenges, initial process op-

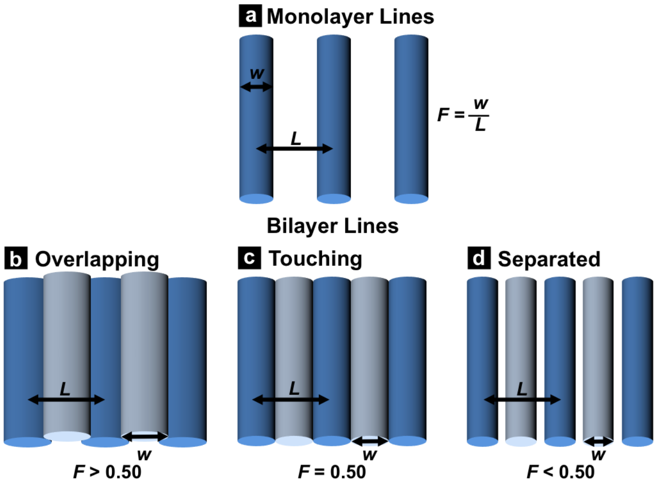

Figure 4.5: (a) Schematic representation of lines derived from a monolayer of cylinders. Fill ratio F is defined as the ratio of line width w to line pitch L, as measured in a monolayer region. (b-d) Assuming the simplest case where $w_t = w_b$ in bilayer lines, $F > 0.50$ results in bilayer lines that overlap (b); $F = 0.50$ results in lines that touch (c); and $F < 0.50$ results in lines that are separated (d). Reprinted with permission from ref. [1]. Copyright © 2013 American Chemical Society.

timization was carried out on monolayer regions; the information learned from the monolayer optimization was then applied to the more challenging bilayer system. Unless otherwise stated, fill ratios, pitches and line widths were measured exclusively in regions of the substrate formed from monolayers of BCP cylinders. Our goal was a monolayer fill ratio of $F \leq 0.25$, which would then lead to bilayer lines separated by gaps as wide as the lines themselves; this goal may be overly ambitious, but was chosen to provide a buffer to accommodate for line waviness, differences in line widths, and other phenomena.

4.3.2 Thermal Annealing

Thermal annealing is a viable approach to promote the self-assembly of horizontal cylinders. By elevating the temperature above the glass transition temperature of both blocks, enough thermal energy is given to allow the poly-

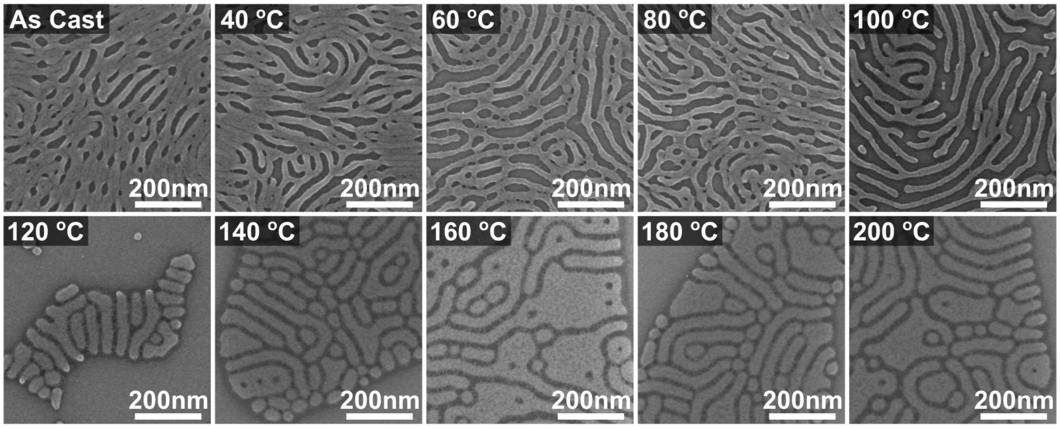

Figure 4.6: Line structures of 43 nm thick PS-*b*-PDMS films annealed at various temperatures for 40 min on a heating block.

mer chains to slide past each other and rearrange into thermodynamically favourable configurations. The melting point of PDMS is around -50 °C, and the glass transition temperature of PS is around 100 °C,[21, 22] thus heating the BCP films above 100 °C should free the PS matrix and allow the BCP film to assemble into the thermodynamic equilibrium configurations. 43 nm thick neat BCP film samples were placed on a heating block for 40 min at various temperatures, and the resulting structures after plasma treatment are displayed in Figure 4.6.

As shown in Figure 4.6, the structures did not deviate much from the as-cast film for temperatures below 100 °C. As the temperature increased towards 100 °C, the multiple layers of lines from the as cast film began to disappear and were slowly replaced by well-spaced lines. For temperatures beyond 100 °C, however, the lines suddenly became thicker, and other phases including perforated lamellar and lamellar structures were observed. The lines from the thermal anneal above 100 °C had line width, $w = 32 \pm 2$ nm; line pitch, $L = 49 \pm 2$ nm; and fill ratio, $F = 0.64 \pm 0.06$. The fill ratio for these lines was much too large for any density-doubled line patterns to be useful in patterning density-doubled lines, so this anneal technique was abandoned in favour of solvent annealing.

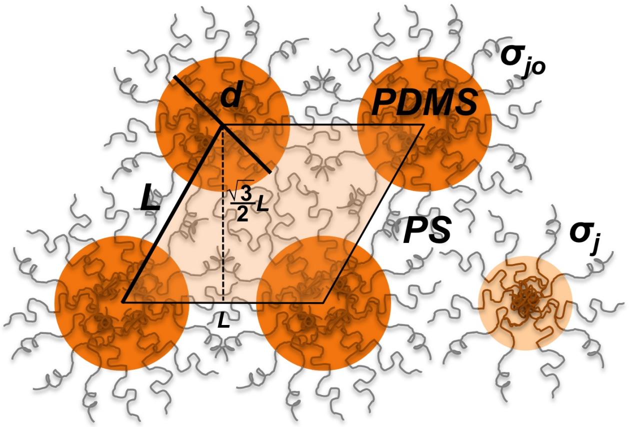

Figure 4.7: Schematic of hexagonally-packed cylinders with diameter d, cylinder spacing L, and the average area occupied by a BCP junction in a neat BCP film σ_{jo}. If the film is altered such that the average area occupied by a BCP junction changes to σ_j, the dimensions of the cylinders change.

4.3.3 Polymer Film Swelling

One way to tune the fill ratio of the templated line structures is to tune the dimensions of the BCP cylinders during the annealing step. Figure 4.7 shows a cross section schematic of a hexagonally-packed cylinder system with cylinder diameter (d), and cylinder spacing (L). During self-assembly, each BCP chain assembles such that the PDMS blocks are found solely in the cylinder regions, and the PS blocks are found solely in the surrounding matrix. The junctions of each BCP, where the two blocks are covalently linked, are located at the interface between the cylinders and surrounding matrix. Assuming that the width of the interface is negligibly thin, that the polymer film is incompressible, and that full phase separation has occurred, two key relations may be derived from the geometry just as they were obtained for lamellar BCPs.[23, 24]

As the cylinder dimensions are reduced, the surface area to volume ratio of the cylinders increases. Due to the incompressibility of the film, smaller cylinders must invariably contain fewer polymer chains, and thus have fewer BCP chain junctions at their interface. One important parameter that essentially describes the surface area to volume ratio of the polymer is the average interfacial area occupied by a single BCP junction, σ_j, which is found by geometry to be related to d as described in Equation 4.3.2. $M_{n,\mathrm{PDMS}}$ is the molecular weight of a single PDMS block, and ϱ_{PDMS} is the density of PDMS. Thus, changes in σ_j will result in inverse changes in d.

$$d = \frac{4M_{n,\mathrm{PDMS}}}{N_A \varrho_{\mathrm{PDMS}} \sigma_j} \tag{4.3.2}$$

The volume fraction of PDMS, ϕ_{PDMS}, may be calculated from Figure 4.7 by examining the fraction of the parallelogram unit cell covered by the PDMS cylinders. The relation may be rewritten to describe the ratio of cylinder diameter to cylinder spacing ($\frac{d}{L}$) as a function of PDMS volume fraction (ϕ_{PDMS}) as described by Equation 4.3.3.[23] Ideally, if the PDMS cylinder geometry directly translates to the templated line morphology, the $\frac{d}{L}$ ratio is exactly equal to the fill ratio F. Due to a non-zero block-to-block interfacial width, possible changes during solvent annealing, and non-ideal plasma conditions, however, $\frac{d}{L}$ and F may be different. Since the ϕ_{PDMS} of the neat PS-*b*-PDMS films is known to be approximately 0.34, the $\frac{d}{L}$ of the thermally annealed samples *vide supra* should theoretically be around 0.61, which agrees within error with the experimentally obtained value of $F = 0.64 \pm 0.06$. Thus, as shown here, F is highly dependent on the ratio $\frac{d}{L}$, and thus, also on ϕ_{PDMS}. If the volume fraction of the PDMS block could be tuned, a greater degree of control on the fill ratio could be gained.

$$\frac{d}{L} = (\frac{2\sqrt{3}\phi_{\mathrm{PDMS}}}{\pi})^{1/2} \tag{4.3.3}$$

While synthesizing a new PS-*b*-PDMS BCP may be an option for tuning ϕ_{PDMS}, a simpler solution which eliminates the need to synthesize new polymers for each new set of line parameters is the introduction of a selective solvent or homopolymer to swell blocks in the BCP film.[25, 26] Selective solvent swelling of a BCP film increases the mobility of the BCP, thus facilitating the self-assembly process. However, the swelling is temporary, since at the end of the treatment, the solvent is removed from the film, leading to a collapse in the film structure. Homopolymer swelling, on the other hand, does not increase the mobility of the BCP chains significantly. However, this type of selective swelling of the BCP film is permanent, as there is little chance for the large homopolymer chains to escape from the film. Since swelling occurs during a solvent anneal, the effect of solvent swelling on the line structures during solvent annealing was investigated first.

Solvent Swelling

Solvent annealing was performed inside the aluminum chamber designed in Chapter 3, using neat THF and monitored by *in situ* ellipsometry. Since THF is a selective solvent for PS,[27] it was expected that as the film swelled during the anneal, the volume fraction of the PS would increase, thus ultimately reducing the fill ratio of the line patterns. This phenomenon was also observed in a P2VP-*b*-PDMS system by Jeong *et al.*[28]

As with the PS-*b*-P2VP films, the PS-*b*-PDMS films initially swelled rapidly before reaching a plateau as shown in Figure 4.8a. Starting with an initial PS-*b*-PDMS film thickness of ~ 36 nm, the solvent vapour anneal was terminated at different target degrees of swelling, D, with a quick purge of air to kinetically trap the self-assembled structures. Representative SEM images of $\mathrm{SiO_x}$ line structures obtained by terminating solvent anneals at different predetermined D are displayed in Figure 4.8b. For samples containing both monolayer and bilayer line regions, the monolayer and bilayer regions are displayed in the top and bottom halves of the images, respectively. The widths (w), pitches (L), and fill ratios (F) of monolayer line structures resulting from terminating the anneal at different D are plotted in Figure 4.8, panels c, d, and e, respectively.

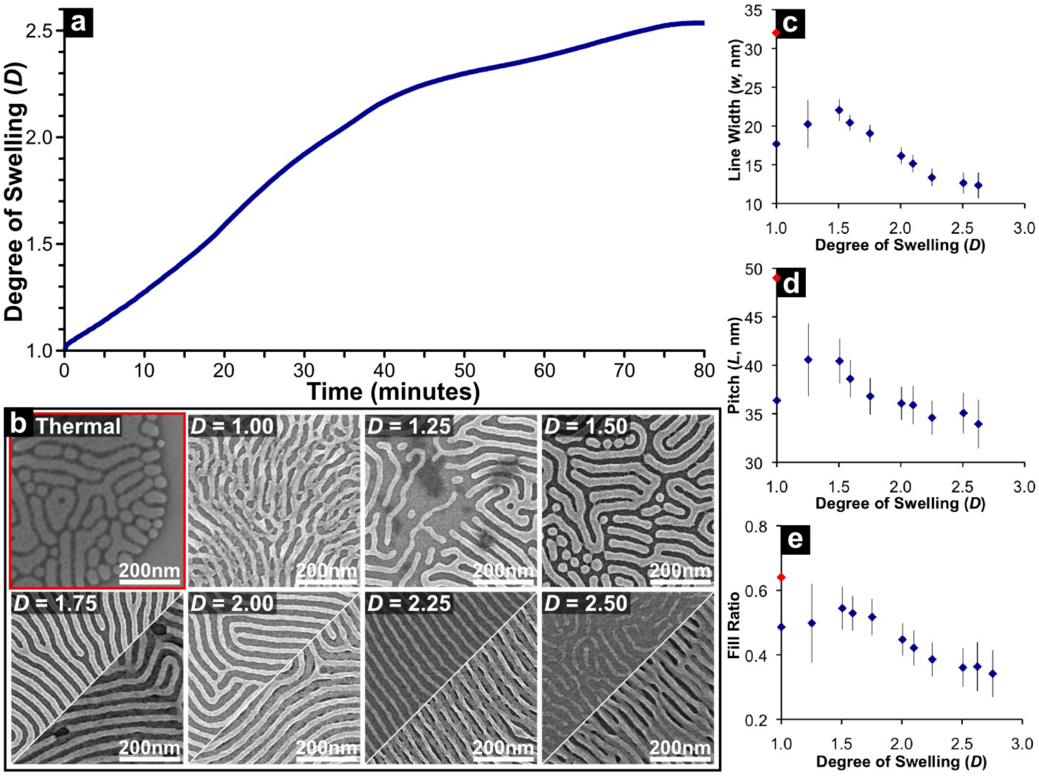

Figure 4.8: (a) Plot showing swelling over 80 min of a 36 nm PS-*b*-PDMS film in THF vapour. (b) SEM images of the plasma treated samples after stopping anneals at different degrees of swelling. Images split in half display monolayer and bilayer regions in the top and bottom halves, respectively. A sample thermally annealed at 180 °C for 40 min is outlined in red and included for comparison. Plots showing line width (c), pitch (d), and fill ratio (e) after swelling to different D are also displayed. The red points represent the thermally annealed sample. The error bars represent the standard deviation of the measurements made. Adapted with permission from ref. [1]. Copyright © 2013 American Chemical Society.

Data and SEM images of a BCP film thermally annealed at 180 °C for 40 min from the previous section are also included for comparison and are highlighted in red.

During the solvent anneal, w, L, and F were all observed to increase for $D \leq 1.50$, before slowly decreasing as the film continued to swell to $D = 2.63$. The initial increase in w, L, and F could be attributed to a gradual shift of polymer structures from their kinetically trapped as-cast state to a more thermodynamically favoured state, as shown by the thermally annealed sample. Because insufficient solvent plasticizer was present early on, the initial reorganization was slow and non-uniform, as suggested by the large standard deviation in pitch and line width in the $D = 1.25$ samples. As the solvent content increased to $D \geq 1.50$, however, the mobility of the polymer became sufficient for a complete transition into the cylinders favoured at equilibrium, and the standard deviation in cylinder pitch and width dropped markedly (Figure 4.8c,d).

As expected with sufficient polymer mobility, swelling of PS-*b*-PDMS above $D = 1.50$ with a PS selective solvent resulted in a decrease in F as D increased. This was a result of an decrease in PDMS volume fraction, forcing the self-assembled cylinders to reduce the $\frac{d}{L}$ ratio, as described by Equation 4.3.3. Besides the decrease in F, there was also a decrease in w and L as D was increased. This has previously been attributed to a solvent shielding effect, which lowers the effective χ parameter of the system.[1, 28] Since the effective Flory parameter χ_{eff} of a solvent swelled system is related to D and the BCP Flory parameters between the blocks and solvent (χ_{AB}, χ_{AS}, χ_{BS}), as shown in Equation 4.3.4, combining with Equation 3.1.1 results in the relation displayed in Equation 4.3.5. The changes in line pitch with respect to D, however, are much too large for a $D^{-1/6}$ dependence. Thus, some other effects must also be at work in reducing the line pitch.

$$\begin{aligned}
\chi_{eff} &= \frac{\chi_{AB} + \chi_{AS} - \chi_{BS}}{D} && (4.3.4)\\
L &\sim aN^{2/3}(\chi_{AB} + \chi_{AS} - \chi_{BS})^{1/6}D^{-1/6} && \\
L &\sim D^{-1/6} && (4.3.5)
\end{aligned}$$

Another effect that may contribute to the decrease in w and L would be the infiltration of solvent molecules between BCP chains. At the block-to-block interfaces, this translates to an increase in average area per BCP junction (σ_j), thus decreasing the diameter of cylinders (as described in Equation 4.3.2) in the swelled film and the resulting line widths of the silica lines. Because of the significant reduction in w (from 22 ± 1 to 12 ± 2 nm) during solvent swelling (from $D = 1.50$ to 2.50) and the slower decrease in F (from 0.54 ± 0.07 to 0.34 ± 0.07), the L was forced to be reduced (from 34 ± 3 to 40 ± 2 nm) to maintain the relationship in Equation 4.3.1. Significant line overlap was still observed in all bilayer regions, and so additional experimental refinements were required to form distinctly separated lines.

Homopolymer Swelling

Homopolymer blending has also been shown to be an effective way of tuning the spacings of BCP templated features.[24, 25, 29, 30] In several studies, it was found that the length of homopolymer played an important role in the tuning of both cylindrical and lamellar domain sizes. For example, in early studies by Winey *et al.*,[24] the introduction of PS homopolymer in a lamellar-forming PS-*b*-PI polymer led to an increase in PS domain width and a reduction in PI domain width. They also found that blends with larger molecular weight PS produced structures with lower σ_j. This suggested that larger PS homopolymers did not uniformly swell the PS domains especially near the domain interfaces, but instead tended to segregate from the PS blocks and formed their own region. Smaller homopolymers, however, tended to segre-

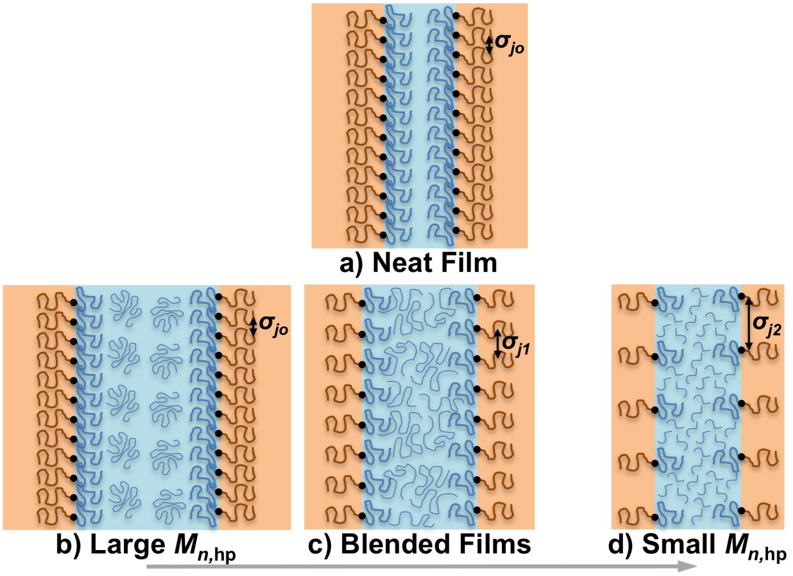

Figure 4.9: (a) Neat BCP films self-assemble with an average area per junction of σ_{jo}. (b-d) As the homopolymer molecular weight, $M_{n,\mathrm{hp}}$, is decreased, the average area per junction increases from σ_{jo} to σ_{j1} and σ_{j2}. The domain dimensions also decrease, although the relative ratios between dimensions remain constant so long as the volume fractions remain the same.

gate more uniformly and were found at the block-to-block interfaces between junctions as well. The presence of these homopolymers at interfaces resulted in a greater separation between BCP junctions (increase in σ_j) at the interfaces (as shown in Figure 4.9). This lateral expansion of the BCP along the cylinder interfaces must be balanced by a reduction of the domain sizes in order for the polymer density in both blocks to remain constant. It is important to note, however, that although the size and periodicity of the polymers change inversely with σ_j, the fill ratio remains constant so long as the relative volume fractions of each block remain constant.

In the present case, by adding PS homopolymer to form a PS/PS-*b*-PDMS blend, the volume fraction of PS would increase and thus lower the fill ratio, F. A large PS homopolymer with molecular weight $M_w = 192$ kg/mol was used to form a blended film with 20 wt% homopolymer. Figure 4.10 displays the structures obtained from this polymer as cast, and also when swelled to

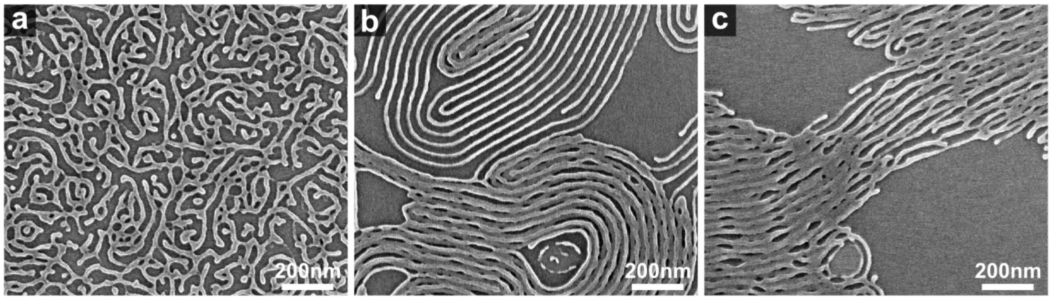

Figure 4.10: A $M_w = 192$ kg/mol homopolymer was blended at 20 wt% with the PS-*b*-PDMS polymer. SEM images of the resulting as cast films (a), films swelled to $D = 2.00$ (b), and $D = 2.25$ (c) are shown.

$D = 2.00$ and $D = 2.25$. As shown in panels b and c, these blends produced very large regions with no line structures, making the polymer unsuitable for producing highly ordered patterns. These regions were likely the result of homopolymer segregation, since the polymer chains were too large to properly integrate with the BCP domains. Thus, a much smaller polymer was used for homopolymer blending.

Solutions of PS/PS-*b*-PDMS homopolymer blends were prepared with the homopolymer PS (10 kg/mol) content varying from 0 wt% to 30 wt%. Films of these blended polymers were then cast into 36 nm thick films; annealed in THF vapour to $D = 1.75$, 2.00, and 2.25; and plasma treated as described previously. SEM images of the self-assembled structures formed after swelling films to $D = 2.25$ are displayed in Figure 4.11a. The measured w, L, and F for these samples are plotted in Figure 4.11, panels b, c, and d, respectively.

As the homopolymer concentration was increased, there was a slight tendency toward thinner and more widely-spaced lines. For example, in the case of $D = 2.25$, line widths were reduced from 13 ± 1 to 10 ± 1 nm (Figure 4.11b), the pitch increased from 35 ± 2 to 38 ± 2 nm (Figure 4.11c), and the fill ratio decreased from 0.38 ± 0.05 to 0.26 ± 0.04 (Figure 4.11d) when a 25 wt% PS homopolymer blend was used. It was interesting to note that unlike solvent swelling, w decreased only very slightly and L increased as the homopolymer concentration was increased. This could be explained by the fact that because

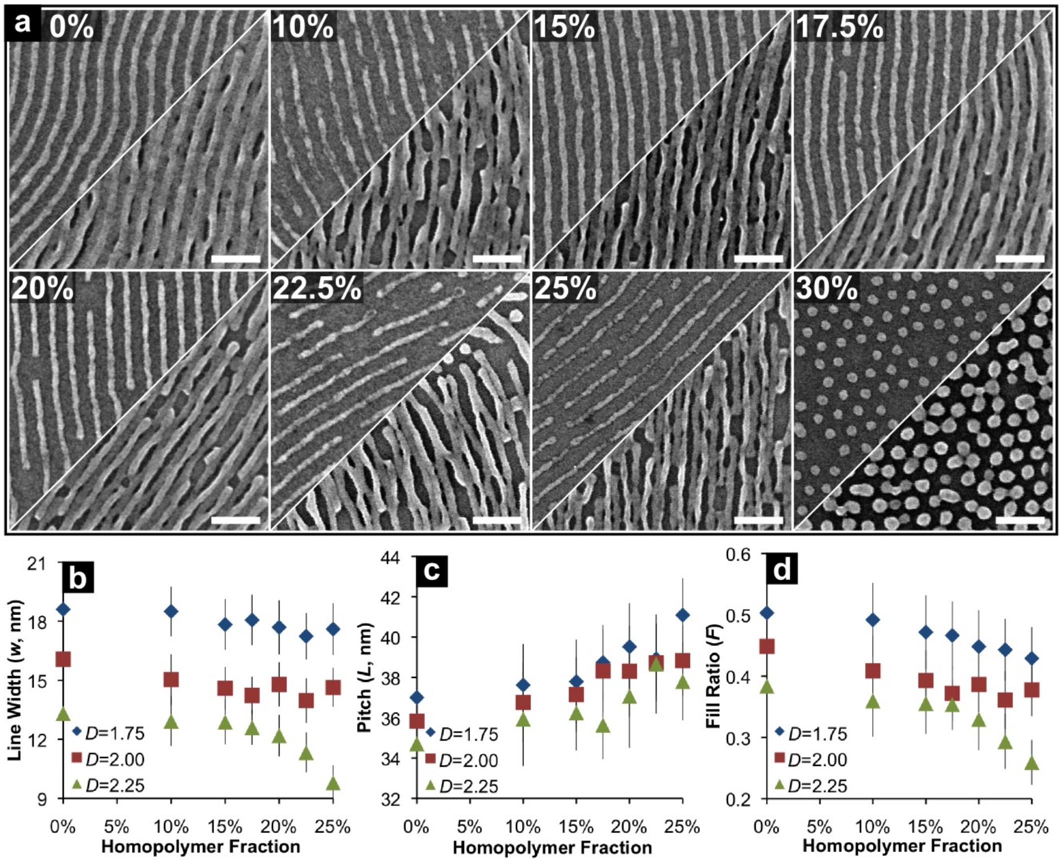

Figure 4.11: (a) SEM images demonstrating the evolution of structures swelled to a uniform $D = 2.25$ as the fraction of PS homopolymer in the films was increased. The top half of each image displays patterns found in monolayer regions, while the bottom half shows patterns found in bilayer regions, and all scale bars are 100 nm. Plots of line width (b), pitch (c), and fill ratio (d) as the concentration of PS homopolymer is increased up to 30 wt% are also shown. All samples have an initial film thickness of 36 nm. The error bars represent the standard deviation of all the line width or pitch measurements that were made. Adapted with permission from ref. [1]. Copyright © 2013 American Chemical Society.

the homopolymer was considerably larger than the solvent molecules, there was a smaller increase in σ_j for homopolymer swelling as compared with solvent swelling. To maintain uniform polymer density and to satisfy the volume fraction requirements, the cylinder spacings, and thus also the line pitch L increased as the homopolymer concentration in the film increased.

In the final panel of Figure 4.11a where a homopolymer fraction of 30 wt% was used, the structures changed drastically from line patterns to dot patterns. This morphological change delineates the upper limit for PS homopolymer in the blend composition. Even at 25 wt%, the line structures displayed numerous defects, such as interruptions with areas of hexagonal dots and discontinuities. Similar trends were observed for $D = 1.75$ and $D = 2.00$ with respect to the pitch (Figure 4.11c), although the decrease in line width was not as pronounced and within the measured standard deviations (Figure 4.11b). It was concluded that a homopolymer composition of 22.5 wt% PS/PS-*b*-PDMS with a solvent degree of swelling $D = 2.00$ would be applied to the bilayer system (*vide infra*) since it minimized the fill ratio while avoiding most defects observed at 25 wt% and 30 wt% PS.

4.3.4 Brush Layers

It was observed in the annealing experiments described in Figure 4.12 that the SiO_x lines derived from top level lines were consistently 2 or 3 nm narrower than their lower level counterparts. For example, in neat BCP films annealed to $D = 2.25$, the line widths w_t and w_b were 14 ± 1 and 16 ± 1 nm, respectively. While one possible cause may have been the difference in plasma exposure leading to increased etching of upper layer lines, inspection of cross-section and tilted SEM images revealed that lines originating from lower layer cylinders were also flat and spread over the wafer surface, suggesting possible interactions with the silicon surface. To confirm this conjecture, PS and PDMS brush layers were grafted onto clean silicon substrates by heating films of hydroxy-terminated PS or PDMS at 130 °C in a vacuum oven for 2 h. The

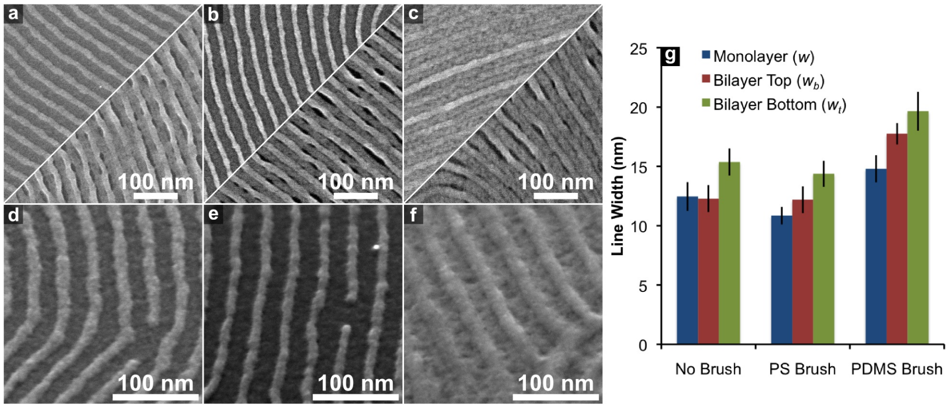

Figure 4.12: SEM images of SiO_x line structures produced from solvent annealed PS-*b*-PDMS BCPs on Si wafers with no brush layer (a,d), PS brush layer (b,e), and PDMS brush layer (c,f). The h_o of these films including their brush layers were 35 nm, 40 nm, and 37 nm, respectively. In (a-c), monolayer and bilayer regions are displayed in the top left and bottom right of each panel, respectively. Close-up SEM images of the single-layer films tilted at 45 ° are displayed below for bare wafers (d), PS brush (e), and PDMS brush (f). (g) Graph of line widths measured from all samples. Reprinted with permission from ref. [1]. Copyright © 2013 American Chemical Society.

excess polymer was then rinsed off with toluene, acetone, and isopropanol, and the brush thicknesses for the PS and PDMS films were found by ellipsometry to be 2 and 5 nm, respectively. The addition of brush layers modifies the interfacial energy at the polymer-surface interface, which has the potential to greatly modify the self-assembly of the polymer.[31]

When a BCP film was then deposited on the substrate, a film normally 35 nm on the native silicon oxide was measured to be 37 nm on a PDMS brush, and 40 nm on a PS brush. A neat BCP film was spin-coated on a PS brush-coated surface and annealed in THF vapour to $D = 2.00$. After plasma treatment, the structures derived from the monolayer and bilayer regions were compared to their analogues assembled on native oxide. The plot in Figure 4.12g demonstrates that the use of a PS brush resulted in a very small reduction in monolayer and bottom layer line width. In contrast, the PDMS brush yielded lines that were always wider than their analogues on native oxide or PS brushes.

The PDMS brushes also resulted in line structures that were partially obscured by a haze, likely of SiO_x, originating from the brush (see Figure 4.12f). Thus, it seems that the use of a PS brush allows a slight but observable advantage with respect to line width.

4.3.5 Plasma Etching

Besides swelling the film with solvents and homopolymers or altering the interfacial properties, another strategy for tuning feature dimensions and line fill ratios is to control the plasma step after self-assembly. The plasma treatment used thus far consisted of two distinct steps: a short 10 s CF_4 plasma step to remove the PDMS layer at the polymer-air interface,[32] and a longer 30 s O_2 plasma step to remove the PS matrix. These two steps rely heavily on the etch selectivity or the difference in PS and PDMS etch rates of these plasmas.

The etch rates of PS and PDMS in O_2 and CF_4 plasmas were determined by exposing PS and PDMS homopolymer films to these plasmas for different durations. The change in film thickness after the plasma treatment was plotted (Figure 4.13), and the etch rate for each material was calculated from the slope of the trendlines. PS was etched at 54 nm/s and 15 nm/s in the presence of O_2 and CF_4, respectively. PDMS was etched at 1 nm/s and 38 nm/s in the presence of O_2 and CF_4, respectively.

By optimizing both plasma steps, reduced fill ratios F may be attained for a particular self-assembled geometry as determined by film swelling and interfacial properties. For demonstration purposes, the plasma optimization was carried out for a 22.5% PS blended film swelled to $D = 2.00$ on a PS brush. Similar optimization routines may be applied to any other film.

Due to its etch selectivity for PDMS, CF_4 plasma was used to remove the surface PDMS layer formed during the solvent anneal. Samples were exposed to this plasma (50 W, 100 mTorr) for different durations and SEM images of the resulting lines were analysed (Figure 4.14). In samples where monolayer

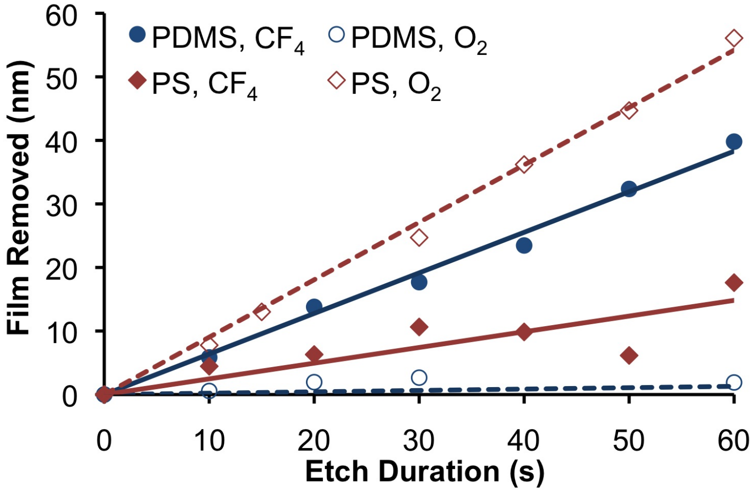

Figure 4.13: Film thickness changes after samples were exposed to O_2 or CF_4 plasmas at 100 mTorr and 30 W.

and bilayer line patterns produced different structures, the SEM was split in half with the top and bottom images displaying monolayer and bilayer regions, respectively. Faint line patterns were observed on the surface prior to plasma etching, suggesting some surface morphology on the PDMS surface. However, these patterns disappeared as the CF_4 etch proceeded. At around 10 s, dark line patterns began appearing, and as the etch continued, it became apparent that these dark lines were trenches formed from etching away the CF_4 cylinders. At the interfaces between monolayer and bilayer regions, dark dots also suggested that hexagonally-packed pits were present. After durations exceeding 20 s, the line structures in bilayer regions were also observed to be more wavy and collapsed compared to monolayer line regions. Since the dark lines first appeared around 10 s, this must be the point at which the PDMS top layer was removed, and the plasma was just beginning to access the underlying cylinder structures. Thus, the ideal duration for the initial step for a 22.5% PS blended film swelled to $D = 2.00$ on a PS brush was between 8 to 10 s.

After optimizing this PDMS removal step at 10 s, the length of time of the subsequent O_2 plasma step (30 W, 100 mTorr) was then varied on identically

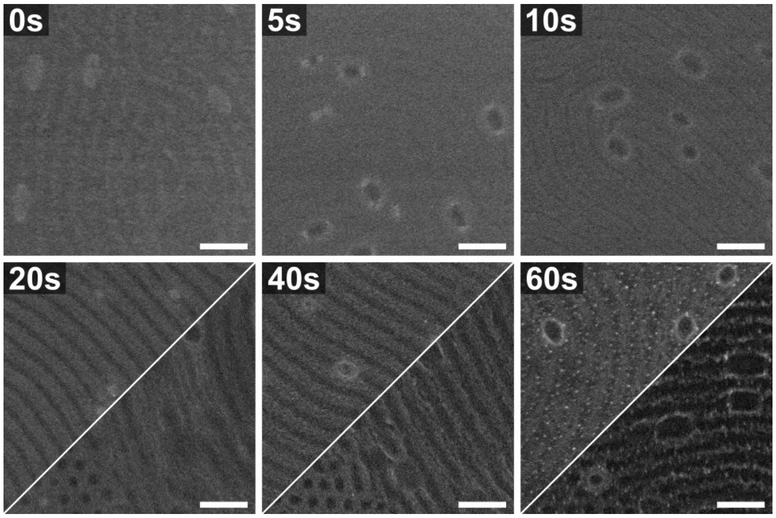

Figure 4.14: SEM images of a 22.5% PS blended film swelled to $D = 2.00$ after exposure to CF_4 plasma at 50 W and 100 mTorr. Scale bars are 100 nm.

prepared samples (36 nm of the 22.5% PS blended film on a PS brush, swelled to $D = 2.00$). The purpose of this second step was to selectively etch the PS and convert the PDMS structures to SiO_x.[17, 19] As the O_2 plasma exposure time was increased from 10 to 30 s, the edges of the cylindrical structures, which were initially nebulous, became sharper and more well-defined (Figure 4.15a). With increasing O_2 plasma time, however, these lines began to merge and by 50 s, the bilayer line structures consisted of large agglomerations of silica. Thus, after the initial 30 s of O_2 plasma treatment, no improvement in fill ratio was observed.

Another strategy to optimize the plasma treatment was to use a more aggressive plasma to slightly etch the PDMS cylinders, while simultaneously removing the PS matrix. Since O_2 and CF_4 plasmas selectively etch different BCP blocks, a plasma with tunable selectivity could be created from a combination of the two gases. In an attempt to find the ideal plasma composition and time, plasmas incorporating 10%, 20%, and 30% CF_4 were used, and SEM images of the resulting structures obtained from varying plasma exposure times are displayed in Figures 4.15b-d. As observed in these SEM images, an increase in plasma CF_4 content led to a decrease in line widths derived from both the

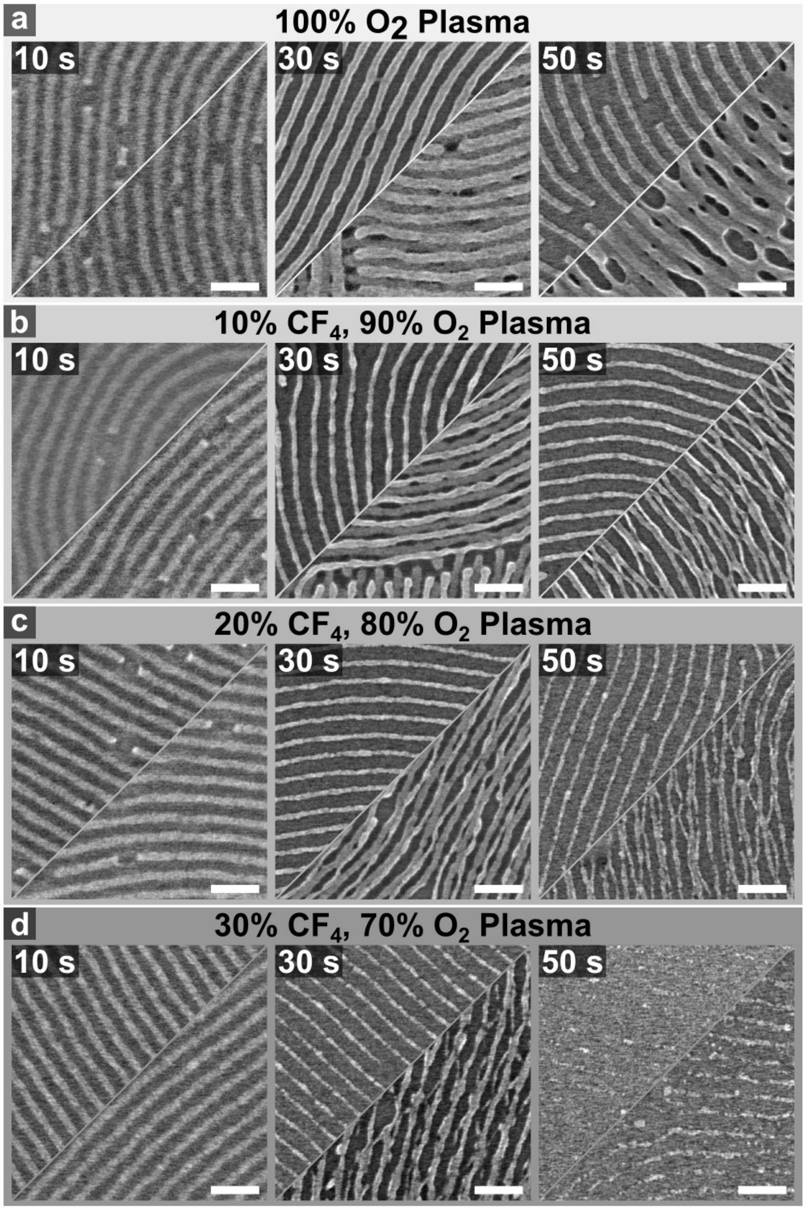

Figure 4.15: 22.5% PS blended samples swelled on a PS brush layer to $D = 2.00$, treated with 10 s of CF_4 plasma to remove the surface PDMS layer, and then subsequently subjected to 100% O_2 (a) or mixed O_2/CF_4 plasmas (b-d) for varying durations. The top halves of each image panel display monolayer regions, while the bottom halves display bilayer regions on the same sample. All scale bars are 100 nm. Reprinted with permission from ref. [1]. Copyright © 2013 American Chemical Society.

upper and lower layers of PDMS cylinders, and thus there was a noticeable increase in the spacing between adjacent lines. As the concentration of CF_4 increased, however, the differences in w_t and w_b also increased due to the fact that the upper lines were exposed to the etchant for longer periods of time. For example, a 20 s plasma exposure at 20% CF_4 produced $w_t = 14 \pm 1$ nm and $w_b = 17 \pm 1$ nm, while an identical exposure in 30% CF_4 produced $w_t = 12 \pm 1$ nm and $w_b = 16 \pm 1$ nm. As the plasma exposure times increased to 50 s or longer, individual lines began to deform and stick to adjacent lines. Thus, the plasma parameters had to be tuned such that enough CF_4 was present to fully separate adjacent lines without etching the top layers too quickly. For the 22.5% PS blended films, a 10% CF_4 plasma step for 25-30 s (Figure 4.16) or a 20% CF_4 plasma step for 20-25 s (Figure 4.17) gave optimum results.

Thus, after combining all these methods, the sample that minimized the F was a 22.5% PS/PS-b-PDMS blended film swelled to $D = 2.00$, subjected to a pure CF_4 plasma step for 10 s, followed by a 10% CF_4 plasma step for 25 s. The resulting densely-packed lines had a bilayer pitch $L/2 = 19 \pm 2$ nm, and widths of $w_t = 10 \pm 1$ nm and $w_b = 14 \pm 1$ nm. The monolayer fill ratio of these samples was $F = 0.27 \pm 0.05$, which was very close to the target of $F = 0.25$.

4.4 Maximizing Bilayer Regions

Besides tuning the line width, pitch, and fill ratio, it was also important to ensure that the bilayer patterns would be observed uniformly over the entire wafer. Almost all the samples produced monolayer, bilayer, and sometimes trilayer regions after the annealing step. These regions were distinct terraces with discretized thicknesses as a result of the self-assembly of the BCP. When observed under an optical microscope, the regions were visually distinct with clear boundaries and different colours. The colours were a result of optical interference, and since each terrace level had a specific film thickness, each level was also uniquely coloured. Thus, by analysing images from optical

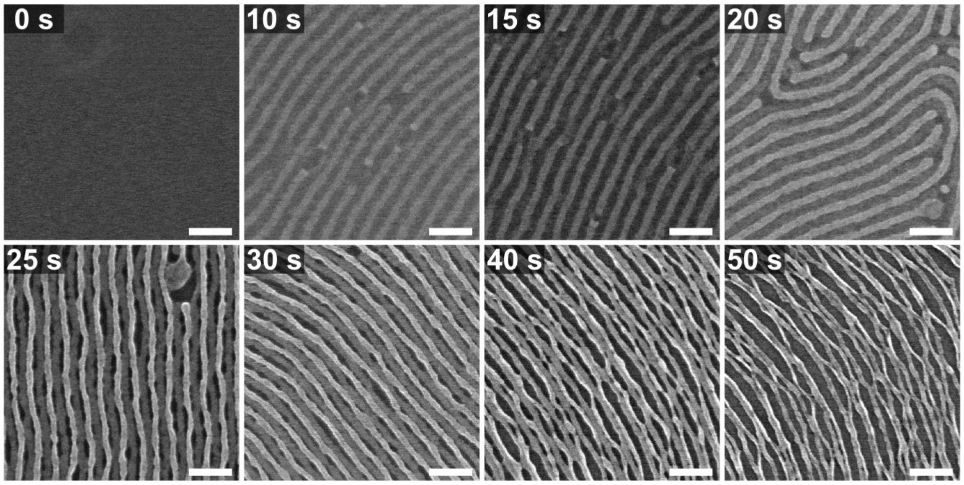

Figure 4.16: SEM images of 22.5% PS blended film swelled to $D = 2.00$ and exposed to 10 s of the initial CF_4 plasma. These samples were then treated with 10% CF_4 mixed plasma at 30 W and 100 mTorr. The time in the top left corner of each box indicates the duration of the mixed plasma treatment. Scale bars are 100 nm.

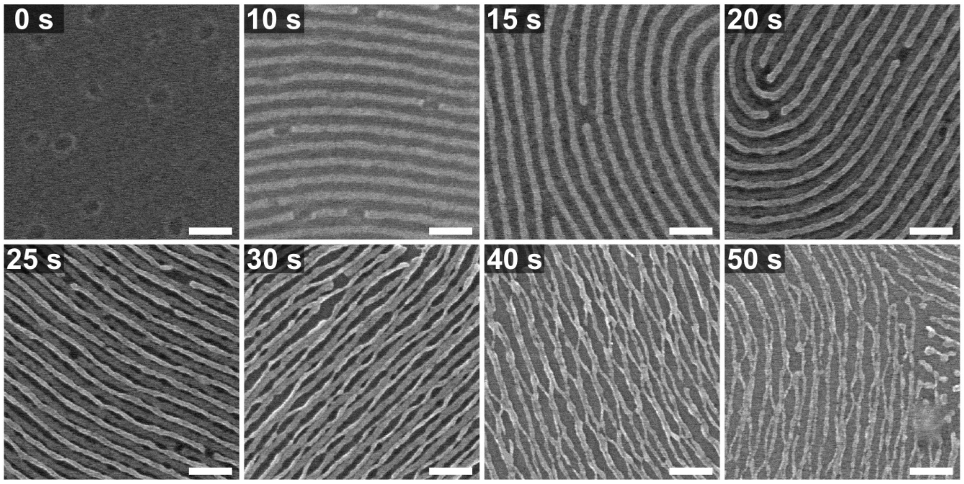

Figure 4.17: SEM images of 22.5% PS blended film swelled to $D = 2.00$ and exposed to 10 s of the initial CF_4 plasma. These samples were then treated with 20% CF_4 mixed plasma at 30 W and 100 mTorr. The time in the top left corner of each box indicates the duration of the mixed plasma treatment. Scale bars are 100 nm.

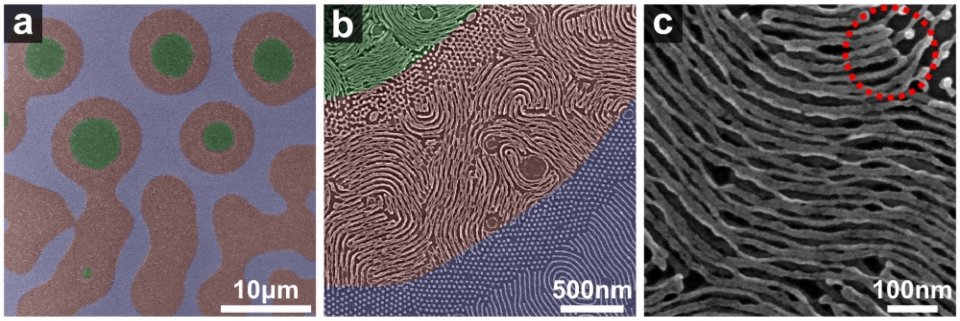

Figure 4.18: (a) SEM of a 22.5% PS/PS-b-PDMS blend swelled to $D = 2.00$. The blue, red, and green false colours were added to highlight the different regions, which corresponded to monolayer, bilayer and trilayer lines, respectively, upon closer inspection (b). A close-up of the green trilayer region (c) shows a third array of lines protruding from underneath one of the two top layer lines.

microscopy, it was possible to determine the area fractions of each of these regions. The samples were also characterized in the SEM so that structures from different regions could be correlated to the appropriate coloured region observed in optical microscopy.

4.4.1 Optical Microscopy Analysis

The bilayer coverage of a sample was measured by taking 200x optical microscopy images from 5 distinct regions in each sample. By taking high-magnification SEM images of these regions, it was confirmed that these regions corresponded to monolayers, bilayers, and trilayers (Figure 4.18). For 22.5% PS blended films, thin strips of dot patterns were also observed at the monolayer/bilayer and bilayer/trilayer interfaces.

To characterize the coverage of each layer, optical microscopy images were processed using the image processing program ImageJ (Figure 4.19). First, the image was converted into a grayscale image. A threshold function was then applied at different pixel intensities to create multiple black and white maps. For the image shown in Figure 4.19, four separate maps were created,

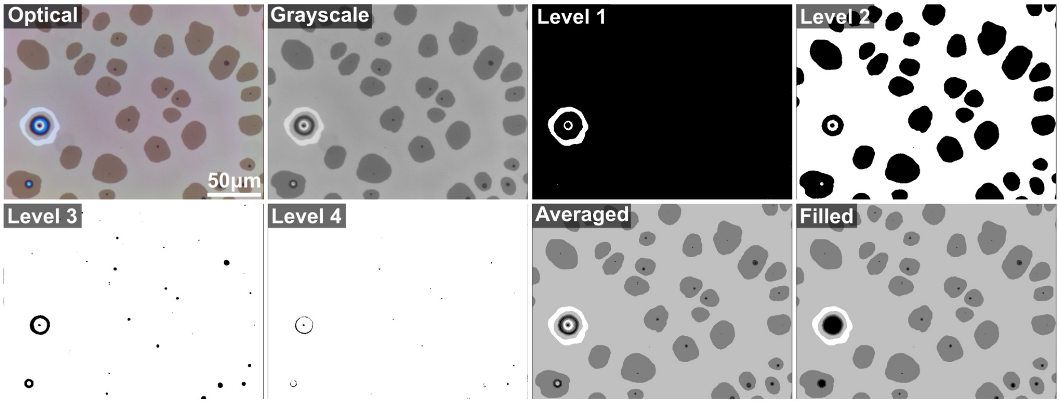

Figure 4.19: The optical image was first converted to a grayscale image. Thresholding was applied 4 times to create 4 different maps, and these maps were averaged. The rings were then filled in with black, and the pixels at each grayscale level were counted.

which were used to differentiate monolayer, bilayer, trilayer, quadlayer, and debris/higher level (5+ layers) regions. These level images were then averaged to create a map with discrete levels of pixel intensity: white regions corresponded to monolayers, each additional layer corresponded to a darker gray, and black corresponded to any of the higher level regions or debris. The averaged image sometimes contained ring structures because the grayscale image could not distinguish the white monolayer regions from the blue, yellow, or orange higher level regions. Thus, these rings were manually filled in with black to group them with the debris/higher level regions. The completed image was then analysed by counting the number of pixels at each intensity. This process was repeated for 5 images in different locations in each sample, and the result was averaged. Sample pixel counts of the image processed in Figure 4.19 are displayed in Table 4.1.

4.4.2 Degree of Swelling

To investigate the effect of film swelling on the fraction of monolayer, bilayer, and trilayer regions, neat 36 nm thick BCP films were spin coated on a PS

Table 4.1: Layer Coverage of Sample

	Averaged		Filled	
Region	Pixels	Percent	Pixels	Percent
Monolayer	21666	1.13%	20137	1.05%
Bilayer	1420653	73.99%	1418840	73.90%
Trilayer	456976	23.80%	454495	23.67%
Quadlayer	11472	0.60%	8228	0.43%
Debris, Higher level	9233	0.48%	18300	0.95%

brush-coated sample and annealed to different degrees of swelling, similar to the samples in Figure 4.8. The percent coverage of each region was then determined for each sample using the image processing techniques described above and displayed in Figure 4.20. Neat BCP films swelled to $D = 1.25$ showed some fluctuations in film thickness (Figure 4.20a), but discrete terraces were not observed until after $D > 1.50$ (Figure 4.20b). Upon closer inspection by SEM of the edges of these discrete terraces (Figure 4.20c), a clear transition from monolayer to bilayer lines was observed. As the films continued to swell, monolayer regions, which covered 97.2 ± 0.4 % of the sample at $D = 1.50$, linearly gave way to bilayers until $D = 2.25$, when the distribution became <0.1 % monolayers, 92.4 ± 0.8 % bilayers, and 6.6 ± 0.4 % trilayers (Figure 4.20d). After this point, if the anneal was left to continue, bilayer regions began to convert into trilayer regions.

Experiments performed for the 22.5% PS blended films in identical conditions showed behaviour similar to the neat BCP films with two key exceptions. Firstly, inspection by SEM revealed a 400-500 nm-wide strip of hexagonal PDMS dots at the boundary of monolayer/bilayer regions (Figure 4.20e). One possible explanation for the presence of the dot interface at the boundaries was that the film thicknesses fell in between that of the monolayer and bilayer regions, and so these local film thicknesses favoured the local formation of spherocylinders,[33] which were then converted into dot patterns upon exposure to plasma. These dot patterns were not observed in the neat films because this phase does not exist at the higher PDMS volume fraction ($\phi_{\mathrm{PDMS}} \sim 0.34$ for neat films, ~ 0.26 for 22.5% PS blended films). Secondly, unlike the swelling

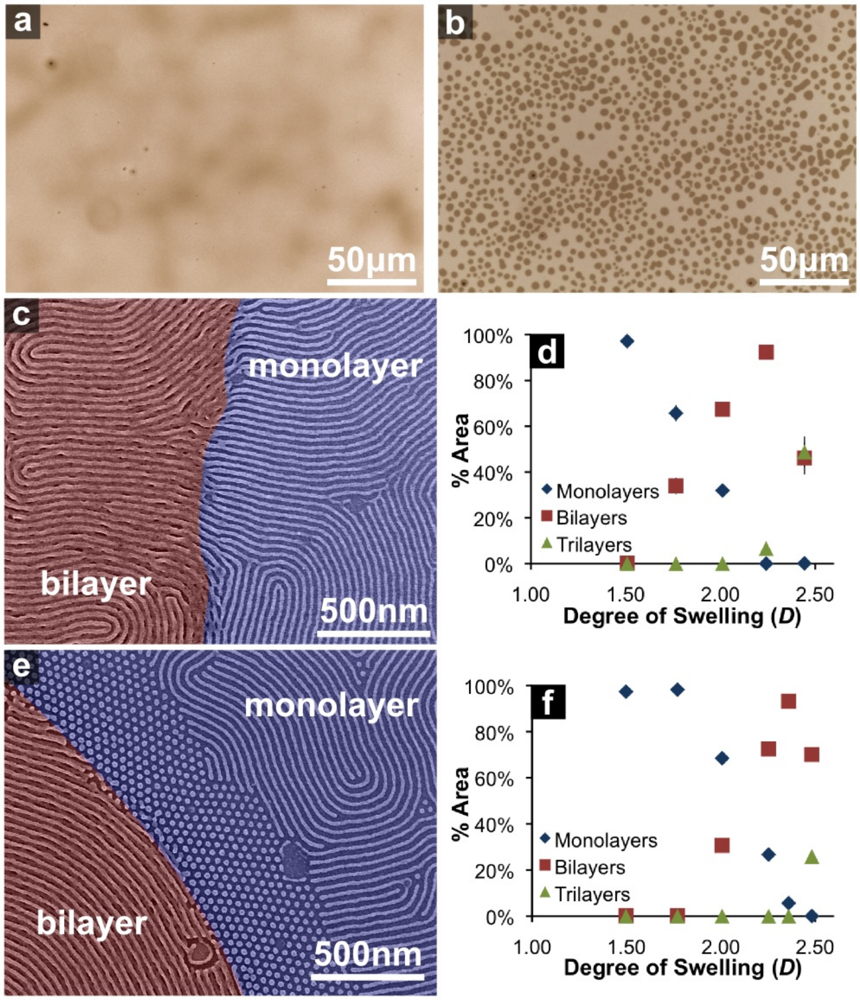

Figure 4.20: Optical micrographs of neat BCP films swelled to $D = 1.25$ (a) and $D = 1.75$ (b). (c) SEM image showing the interface between monolayer and bilayer regions for neat PS-*b*-PDMS films. (d) Plot of the evolution of monolayer/bilayer/trilayer coverage with swelling, D, for neat PS-*b*-PDMS films with initial thickness of 36 nm (excluding the PS brush). (e) SEM image of the monolayer/bilayer interface within the 22.5% PS/PS-*b*-PDMS blended films. (f) Plot of the evolution of monolayer/bilayer/trilayer coverage with swelling, D, for 22.5% PS/PS-*b*-PDMS blended films with initial thickness of 36 nm. Reprinted with permission from ref. [1]. Copyright © 2013 American Chemical Society.

of neat BCP films, the monolayer regions did not begin to transform into bilayers until after $D = 1.75$ (Figure 4.20f). After $D = 1.75$, the monolayers continued to convert into bilayer regions until at $D = 2.36$, where the bilayer fraction peaked at 93.2 ± 2.1 %, with 5.6 ± 1.6 % monolayers and <0.1 % trilayers.

4.4.3 Initial Thickness

Although the degree of swelling, D, clearly had an effect on the percent coverage of these layered structures in the film, it was not a useful parameter to tune the coverage of bilayer regions, as it also had great influence over line widths and pitch. An alternative parameter was the initial film thickness, h_o. As shown in Figure 4.21, neat BCP films were deposited at various thicknesses (from 32 to 48 nm) onto a PS brush coated sample and annealed to a fixed degree of swelling of $D = 2.00$. The resulting terrace structures displayed in Figure 4.21a clearly demonstrate that the monolayer, bilayer, and trilayer fractions of a film could be tuned by varying the initial film thickness. As shown in Figure 4.21b, an initial thickness of 41 nm produced monolayer, bilayer, and trilayer area fractions of 1.3 ± 0.9 %, 96.7 ± 0.8 %, and 1.7 ± 0.4 %, respectively. Thus, near-uniform bilayers were attained across the entire sample when a 41 nm film was swelled to a degree of swelling of $D = 2.00$. When these films were subjected to identical and optimized (10% CF_4 for 25 s in the second step) plasma conditions, no obvious relationship between the initial film thickness and the width or pitch of these lines was observed (Figure 4.21c). This decoupling of these parameters was important, since it meant that initial film thickness could be independently varied to optimize for bilayer formation without affecting line width and pitch.

As shown in the optical micrographs in Figure 4.22, 22.5% PS blended films behaved quite differently when compared to their neat BCP counterparts. When the same experiments were performed for these blended films, trilayer regions started appearing and growing before all the monolayer regions were

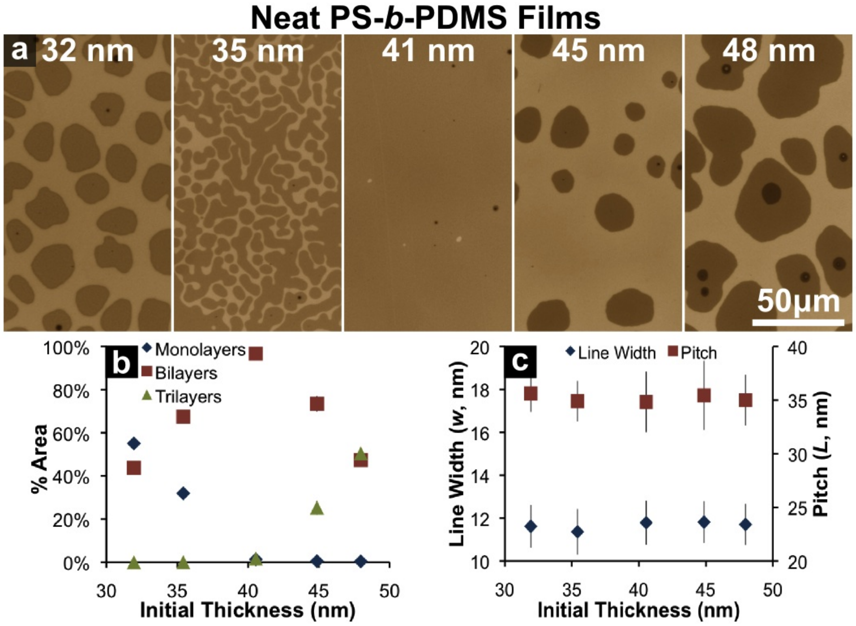

Figure 4.21: (a) Optical micrographs of neat PS-*b*-PDMS films of various thicknesses on a PS brush swelled to $D = 2.00$. (b) Plot of the percent coverage of monolayer, bilayer, and trilayer regions in the same neat PS-*b*-PDMS samples. (c) Plot of line width and pitch of monolayers in these same neat PS-*b*-PDMS samples after a plasma treatment of 10% CF_4 for 25 s. Adapted with permission from ref. [1]. Copyright © 2013 American Chemical Society.

eliminated (Figure 4.22a). One consequence of this early onset of trilayers was that although 22.5% PS blended films could produce line arrays at lower F than neat BCP films, it was impossible to have a high percentage coverage of bilayer regions. SEM images of these films also showed that the initial film thickness had no obvious effect on line width or pitch (Figure 4.22c).

4.5 Conclusions

Utilizing films of bilayer PS-*b*-PDMS cylindrical assemblies as templates, it was possible to generate closely-spaced SiO_x line patterns on a silicon substrate. By tuning the degree of swelling and/or blending the BCP film with

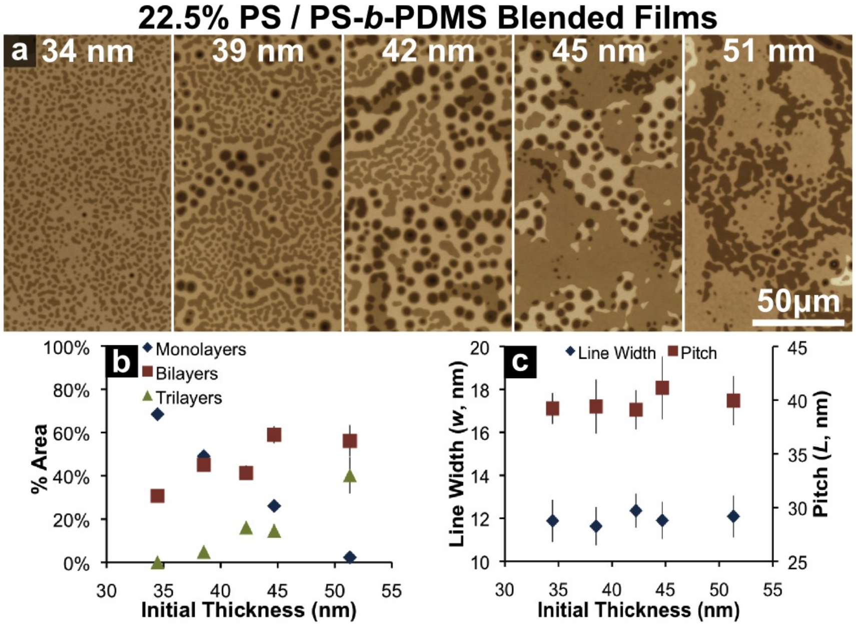

Figure 4.22: (a) Optical micrographs of 22.5% PS/PS-*b*-PDMS blended films swelled to $D = 2.00$. (b) Plot of the percent coverage of monolayer, bilayer, and trilayer regions in the same 22.5% PS/PS-*b*-PDMS blended films. (c) Plot of line width and pitch of monolayers in these same PS blended samples after a plasma treatment of 10% CF_4 for 25 s. Adapted with permission from ref. [1]. Copyright © 2013 American Chemical Society.

PS homopolymer, it was possible to reduce the width and tune the pitch of these silica lines. The line widths of these structures could then be more finely tuned by adjusting a number of other parameters, including the brush layer and the duration/composition of the plasma treatment. If 22.5% PS blended films are used, the monolayer fill ratio could be reduced to $F = 0.27 \pm 0.05$. The coverage of bilayer regions across a sample on the multi-micron scale could then be tuned by adjusting the initial thickness of the BCP film prior to swelling. Thus, a PS-*b*-PDMS polymer that normally produces monolayer silica lines with a pitch of 36 nm can be used to create denser line arrays at a pitch of 18 nm with bilayer coverage as high as 96.7 ± 0.8 %.

There is considerable room for improvement with respect to control over the resulting lines produced through the use of bilayer-based BCP films, particularly with regards to LER and related parameters. As can be seen from the SEM images in Figure 4.2, the monolayer cylinders are smoother, and have obvious lower peristaltic LER. The silica lines derived from the bilayer PS-*b*-PDMS structures present considerable undulations, and will require careful optimization to improve the LER.[34] One possible source of the undulations observed include the melting or flowing of PDMS cylinders (melting point of around -50 °C)[21, 22] if the supporting PS underlayer degrades before the PDMS fully converts into silica. Solutions to this problem could be to add groups to cross-link the PDMS prior to plasma, or to use more anisotropic plasma etching conditions to prevent the underlying PS from degrading underneath the cylinders before they become silica.[35] The undulations may also be a product of the rapid change in film thickness at the end of the anneal. If this was the case, a solution to remediate this problem may be to introduce a gentle secondary thermal anneal.[36] In addition, placement accuracy will also need to be thoroughly investigated with respect to graphoepitaxy and the use of registration marks, as has recently been carried out by Doerk and co-workers.[37] One particularly promising direction to improving LER is to reduce the interfacial tension between the two blocks through the addition of a third non-volatile component as a ‘compatibilizer’ to lower the surface energy at the interfaces in these nanoscale phase-separated domains.[38] The second direction for attention is the plasma conversion step — the transformation of flexible PDMS into a brittle and fragile metal oxide (in this case, silica) locks in the resulting specific shape under these low-temperature conditions. Thus, silica precursors may not be the ideal material to produce lines with low LER when compared with flexible organic, and possibly even metallic precursors that are more readily annealed. These aspects will be the focus of upcoming work.

References

[1] N. L.-Y. Wu, K. D. Harris, and J. M. Buriak, "Conversion of bilayers of PS-*b*-PDMS block copolymer into closely packed, aligned silica nanopatterns," *ACS Nano*, vol. 7, no. 6, pp. 5595–5606, 2013.

[2] D. L. Pulfrey and J. J. H. Reche, "Preparation and properties of plasma-anodized silicon dioxide films," *Solid-State Electronics*, vol. 17, pp. 627–632, 1974.

[3] H. Iwai and S. Ohmi, "Silicon integrated circuit technology from past to future," *Microelectronics Reliability*, vol. 42, no. 4-5, pp. 465–491, 2002.

[4] S. A. Campbell, *The Science and Engineering of Microelectronic Fabrication*, 2nd ed. New York, NY: Oxford University Press, 2001.

[5] I. I. Slowing *et al.*, "Mesoporous silica nanoparticles as controlled release drug delivery and gene transfection carriers," *Advanced Drug Delivery Reviews*, vol. 60, no. 11, pp. 1278–1288, 2008.

[6] J. L. Vivero-Escoto *et al.*, "Mesoporous silica nanoparticles for intracellular controlled drug delivery," *Small*, vol. 6, no. 18, pp. 1952–1967, 2010.

[7] Z. Li *et al.*, "Mesoporous silica nanoparticles in biomedical applications," *Chemical Society Reviews*, vol. 41, no. 7, pp. 2590–2605, 2012.

[8] F. Tang, L. Li, and D. Chen, "Mesoporous silica nanoparticles: Synthesis, biocompatibility and drug delivery," *Advanced Materials*, vol. 24, no. 12, pp. 1504–1534, 2012.

[9] K. Wang *et al.*, "Functionalized silica nanoparticles: A platform for fluorescence imaging at the cell and small animal levels," *Accounts of Chemical Research*, vol. 46, no. 7, pp. 1367–1376, 2013.

[10] B. Hatton *et al.*, “Assembly of large-area, highly ordered, crack-free inverse opal films,” *PNAS*, vol. 107, no. 23, pp. 10 354–10 359, 2010.

[11] I. B. Burgess *et al.*, “Wetting in color: Colorimetric differentiation of organic liquids with high selectivity,” *ACS Nano*, vol. 6, no. 2, pp. 1427–1437, 2012.

[12] E. W. Cochran, D. C. Morse, and F. S. Bates, “Design of ABC triblock copolymers near the ODT with the random phase approximation,” *Macromolecules*, vol. 36, no. 3, pp. 782–792, 2003.

[13] K. H. Dai and E. J. Kramer, “Determining the temperature-dependent Flory interaction parameter for strongly immiscible polymers from block copolymer segregation measurements,” *Polymer*, vol. 35, no. 1, pp. 157–161, 1994.

[14] F. S. Bates and G. H. Fredrickson, “Block copolymer thermodynamics — Theory and experiment,” *Annual Review of Physical Chemistry*, vol. 41, pp. 525–557, 1990.

[15] Y. S. Jung *et al.*, “A path to ultranarrow patterns using self-assembled lithography,” *Nano Letters*, vol. 10, no. 3, pp. 1000–1005, 2010.

[16] W. I. Park *et al.*, “Self-assembly-induced formation of high-density silicon oxide memristor nanostructures on graphene and metal electrodes,” *Nano Letters*, vol. 12, no. 3, pp. 1235–1240, 2012.

[17] W. I. Park *et al.*, “Self-assembled incorporation of modulated block copolymer nanostructures in phase-change memory for switching power reduction,” *ACS Nano*, vol. 7, no. 3, pp. 2651–2658, 2013.

[18] A. Tavakkoli K. G. *et al.*, “Templating three-dimensional self-assembled structures in bilayer block copolymer films,” *Science*, vol. 336, no. 6086, pp. 1294–1298, 2012.

[19] H. Hillborg *et al.*, “Crosslinked polydimethylsiloxane exposed to oxygen plasma studied by neutron reflectometry and other surface specific techniques,” *Polymer*, vol. 41, no. 18, pp. 6851–6863, 2000.

[20] W. Kern, Ed., *Handbook of Semiconductor Wafer Cleaning Technology: Sci-*

ence, Technology, and Applications. Westwood, NJ: Noyes Publications, 1993.

[21] K. A. Andrianov *et al.*, "Some physical properties of polyorganosiloxanes. I. Linear polyorganosiloxanes," *Journal of Polymer Science, Part A-1: Polymer Chemistry*, vol. 10, no. 1, pp. 1–22, 1972.

[22] J. E. Mark, *Polymer Data Handbook*, 2nd ed. New York, NY: Oxford University Press, 2009.

[23] H. Tanaka, H. Hasegawa, and T. Hashimoto, "Ordered structure in mixtures of a block copolymer and homopolymers. 1. Solubilization of low molecular weight homopolymers," *Macromolecules*, vol. 24, no. 1, pp. 240–251, 1991.

[24] K. I. Winey, E. L. Thomas, and L. J. Fetters, "Swelling of lamellar diblock copolymer by homopolymer: Influences of homopolymer concentration and molecular weight," *Macromolecules*, vol. 24, no. 23, pp. 6182–6188, 1991.

[25] J. Peng *et al.*, "Controlling the size of nanostructures in thin films *via* blending of block copolymers and homopolymers," *The Journal of Chemical Physics*, vol. 122, no. 11, pp. 114 706(1–7), 2005.

[26] X. Zhang *et al.*, "Rapid assembly of nanolines with precisely controlled spacing from binary blends of block copolymers," *Macromolecules*, vol. 44, no. 24, pp. 9752–9757, 2011.

[27] I.-F. Hsieh *et al.*, "Phase structural formation and oscillation in polystyrene-*block*-polydimethylsiloxane thin films," *Soft Matter*, vol. 8, no. 30, pp. 7937–7944, 2012.

[28] J. W. Jeong *et al.*, "Highly tunable self-assembled nanostructures from a poly(2-vinylpyridine-*b*-dimethylsiloxane) block copolymer," *Nano Letters*, vol. 11, no. 10, pp. 4095–4101, 2011.

[29] T. Hashimoto, H. Tanaka, and H. Hasegawa, "Ordered structure in mixtures of a block copolymer and homopolymers. 2. Effects of molecular weights of homopolymers," *Macromolecules*, vol. 23, no. 20, pp. 4378–4386, 1990.

[30] U. Jeong *et al.*, "Asymmetric block copolymers with homopolymers: Routes to

multiple length scale nanostructures," *Advanced Materials*, vol. 14, no. 4, pp. 274–276, 2002.

[31] P. Mansky *et al.*, "Controlling polymer-surface interactions with random copolymer brushes," *Science*, vol. 275, no. 5305, pp. 1458–1460, 1997.

[32] Y. S. Jung and C. A. Ross, "Orientation-controlled self-assembled nanolithography using a polystyrene-polydimethylsiloxane block copolymer," *Nano Letters*, vol. 7, no. 7, pp. 2046–2050, 2007.

[33] W. Li *et al.*, "Phase diagram of diblock copolymers confined in thin films," *Journal of Physical Chemistry B*, vol. 117, no. 17, pp. 5280–5288, 2013.

[34] M. P. Stoykovich *et al.*, "Remediation of line edge roughness in chemical nanopatterns by the directed assembly of overlying block copolymer films," *Macromolecules*, vol. 43, no. 5, pp. 2334–2342, 2010.

[35] R. D. Mansano, P. Verdonck, and H. S. Maciel, "Anisotropic reactive ion etching in silicon, using a graphite electrode," *Sensors and Actuators, A: Physical*, vol. 65, no. 2-3, pp. 180–186, 1998.

[36] E. Kim *et al.*, "Directed assembly of high molecular weight block copolymers: Highly ordered line patterns of perpendicularly oriented lamellae with large periods," *ACS Nano*, vol. 7, no. 3, pp. 1952–1960, 2013.

[37] G. S. Doerk *et al.*, "Pattern placement accuracy in block copolymer directed self-assembly based on chemical epitaxy," *ACS Nano*, vol. 7, no. 1, pp. 276–285, 2013.

[38] L. Fang *et al.*, "Precise pattern replication of polymer blends into nonuniform geometries *via* reducing interfacial tension between two polymers," *Langmuir*, vol. 28, no. 27, pp. 10 238–10 245, 2012.

5

Block Copolymer Graphoepitaxy

5.1 Introduction

The focus of the previous two chapters was on using bilayer structures to double nanopattern density and using anneal, surface, or plasma conditions to tune the dimensions and coverage of these density-doubled features. In this chapter, the graphoepitaxy of BCP structures will be explored. As described in Chapter 2, guiding surface topography for graphoepitaxy is usually formed using top-down patterning techniques such as photolithography or EBL. Thus, this chapter will begin by using wide wells or trenches patterned by EBL to guide the assembly of density-doubled BCP patterns. BCP self-assembly need not, however, rely on lithographically patterned features for graphoepitaxy. BCP-templated features may themselves be used as guiding features for the self-assembly of subsequent layers of BCP. The second half of this chapter will explore the use of multiple layers of BCP to create high-quality densely-packed self-assembled features.

The material in this chapter is based on unpublished work. In this work, Dr. Kenneth Harris and Dr. Jillian Buriak contributed to useful discussions.

5.2 Experimental

5.2.1 Materials

Silicon (100) wafers (prime grade, 100 mm diameter, n-type, phosphorous-doped, ρ = 5–10 $\Omega\cdot$cm) were purchased from University Wafer. 38% HCl (aq), 30% NH_4OH (aq) and 25% aqueous tetramethylammonium hydroxide (TMAH) were obtained from J. T. Baker; methanol, acetone, isopropanol, and 30% H_2O_2 were obtained from Fisher Scientific; heptane, tetrahydrofuran (THF), and toluene were obtained from Caledon Laboratories Ltd.; methyl isobutyl ketone (MIBK) was obtained from MicroChem; and 6% hydrogen silsesquioxane (HSQ) in MIBK was obtained from Dow Corning (XR-1541). Ultrapure water with $\rho > 18$ M$\Omega\cdot$cm from a Millipore Milli-Q system was used for all experiments. The polymers PS(50k)-*b*-P2VP(16.5k), PS(31k)-*b*-PDMS(14.5k), and PS(10k) were obtained from Polymer Source. The metallization salts $Na_2PtCl_4\cdot xH_2O$ and $Na_2PdCl_4\cdot 3H_2O$ were obtained from Strem Chemicals.

5.2.2 Sample Preparation

Silicon wafers were diced into 1×1cm^2 squares and cleaned with the RCA I and RCA II procedures described in Chapter 3. A film of HSQ was then deposited onto the wafers by spin coating dilutions of the 6% stock solution in MIBK at 3000 rpm for 30 s, and baked on a hotplate at 100 °C for 15 min. The baking step was used to drive off excess solvent and prepare the HSQ film for use as a negative resist in the subsequent patterning step. EBL was carried out on the substrate using a RAITH 150-2 system. Patterns such as lines or circles were written with a 10 kV electron beam with an aperture of 10 µm. The electrons caused cross-linking of HSQ units, converting the exposed areas into silica-like material. The samples were then developed in 25% aqueous TMAH, which removed the unreacted HSQ, leaving behind silica walls for guiding BCP

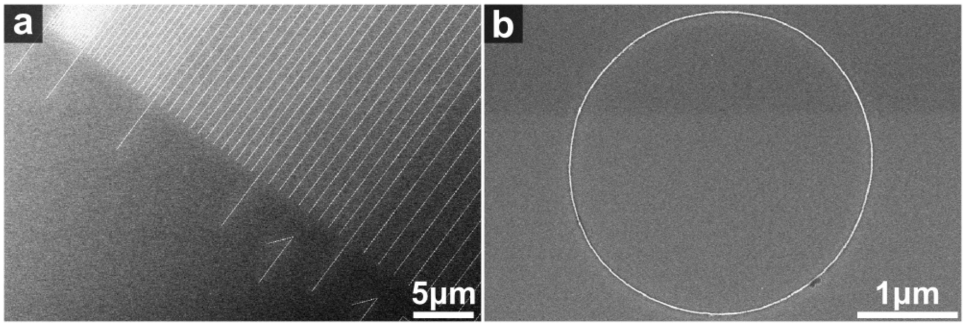

Figure 5.1: SEM images of linear trenches (a) and circles (b) patterned using EBL to be used for graphoepitaxy.

self-assembly. Some examples of the guiding features produced are displayed in Figure 5.1. Parallel lines were produced to delineate linear trenches ranging in width from 200 nm to 10 μm (Figure 5.1a). To investigate the confinement of BCP patterns within wells, circle patterns with diameters ranging from 500 nm to 5 μm were also patterned (Figure 5.1b). The wall features may then be modified by a brush layer by depositing and annealing a brush solution on the substrate at 130 °C for 2 h, as described in Chapter 4.

In the exploration of the effects of EBL patterned walls on BCP self-assembly, the results discussed in this chapter were mainly from the 22.5% PS/PS-*b*-PDMS blends described in Chapter 4, but neat PS(31k)-*b*-PDMS(14.5k) and PS(50k)-*b*-P2VP(16.5k) films were also observed to behave similarly. In the multi-step patterning investigation, all the line patterns were templated by the neat PS-*b*-PDMS polymer, while the dot patterns were templated by the 30% PS/PS-*b*-PDMS blend. The PS-*b*-PDMS polymers were treated with a two-step plasma treatment, with CF_4 for 10 s to remove the top PDMS layer, followed by a 10% CF_4 step for 30 s to remove the PS matrix.

5.3 Lateral Confinement of Block Copolymers

For BCPs to form ordered patterns assembled along the surface topography, sufficient mobility must be granted to the system to allow the BCPs to self-assemble. In most of the systems described in the introduction, thermal annealing was used, which granted mobility through increasing the film temperature. In the case of density-doubled line patterns, solvent annealing was used as the method of granting polymer mobility. Because solvent annealing involves the gradual swelling of BCP films as described in Chapter 3, both the polymer mobility and thickness of the film vary throughout the duration of the anneal. This complication in the system is further exacerbated by the presence of topographical features, as will be described below. The following section explores how the presence of topographical features affects the swelling of the BCP film, which in turn controls the ordering and the type of structures that may be assembled in these regions.

5.3.1 Trench Walls and Terracing

To investigate the effects of adding surface topography, 105 nm tall parallel line features were patterned onto flat substrates using EBL (as shown in Figure 5.1). The wall height was selected to be much greater than the BCP film thickness so as to isolate adjacent trenches and limit the movement of BCP from one trench to another. This lateral confinement of BCPs was maintained even during swelling, as BCP films originally 40 nm thick would need to be swelled above $D = 2.5$ before the BCP could begin overflowing into an adjacent trench. Thus, by spin coating BCP films onto these topographic structures, the effects of complete lateral confinement during solvent annealing may be studied.

A 37 nm film of blended 22.5% PS/PS-*b*-PDMS was swelled to $D = 1.8$ and after plasma treatment, the resulting structures were characterized by SEM (see Figure 5.2). The images revealed that narrow trenches 200 nm in

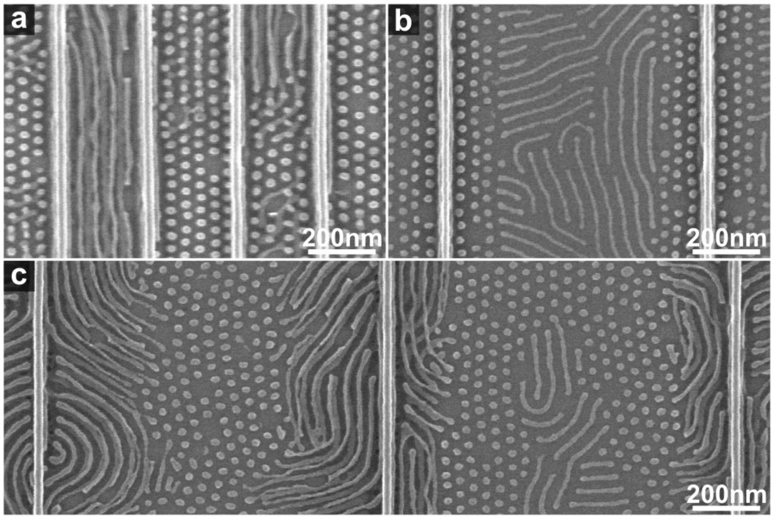

Figure 5.2: SEM images of a 22.5% PS/PS-*b*-PDMS blend swelled to $D = 1.8$. The self-assembling behaviour of BCPs within 200 nm (a), 600 nm (b), and 800 nm (c) wide trenches are shown in the SEM images.

width mainly produced hexagonal dot patterns, but some isolated trenches were also able to form density-doubled line patterns aligned along the long axis of the trench (Figure 5.2a). As the width of the trenches were increased, however, mixtures of patterns were observed in the trenches. For example, in 600 nm wide trenches, hexagonally-packed dot patterns lined the edges of the trenches, while monolayer line patterns were observed in the trench centres (Figure 5.2b). In 800 nm wide trenches, the walls were lined with bilayer cylinders, which then transitioned into hexagonally-packed dots and monolayer cylinders at the centres of the trenches. Similar effects were observed for films of PS(50k)-*b*-P2VP(16.5k) or neat PS-*b*-PDMS except in neat PS-*b*-PDMS films with similar thicknesses and D, bilayer cylinders transitioned immediately into monolayer cylinders without displaying any evidence of dot patterns. The structural transitions observed were strongly reminiscent of the transitions observed at the edges of terraced regions as observed in Chapter 4. They suggest that variations of film thickness exist across the width of the trench, with thicker regions near the walls, and thinner regions near the centre of the trenches. This tendency for thicker terraces to accumulate at the trench

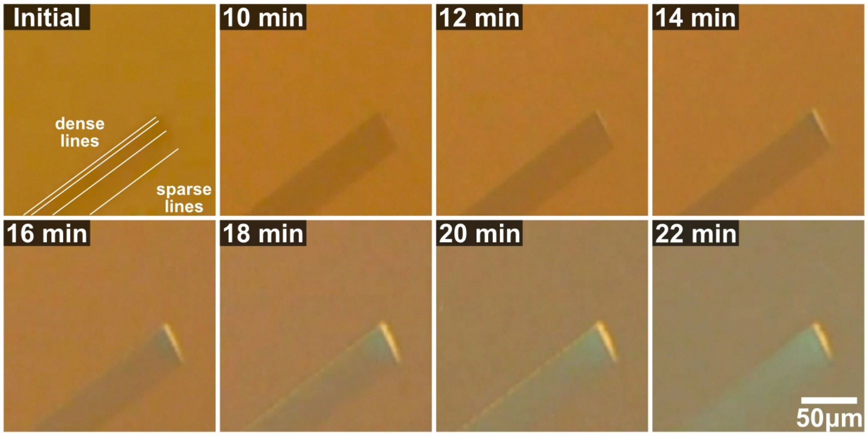

Figure 5.3: Optical micrographs of a PS-*b*-P2VP film near topographical patterns as it is swelled in THF.

walls was also observed by Segalman *et al.* in their work with spherical BCPs in trenches.[1]

The affinity of the BCP to the trench walls also resulted in the diffusion of BCPs toward the wall structures. This diffusion of BCP, likely due to capillary action, has been applied in the past to lamellar-forming BCPs to induce greater order.[2] In our experiments, the phenomenon was made especially clear through *in situ* monitoring of the swelling process of PS-*b*-P2VP in THF using an optical microscope. While no exact measurements of film thickness could be made *in situ*, the changes in film thickness were qualitatively monitored using colour. As the films were swelled, the observed colours slowly changed from light brown to purple, and finally blue, which corresponded to thickness changes from 40 nm to approximately 100 nm (see Figure 5.3). After 12 min, the first signs of diffusion was observed at the end of the trenches. A net flow of BCP into the trenches was evidenced by the depletion of BCP film just outside of the trenches (the formation of a beige region) and the accumulation of BCP film just inside the trenches (the formation of a blue region). The beige and blue regions both expanded from the left to right, suggesting that this redistribution effect was stronger in areas with denser topography. The result was that the trench regions swelled to purple and then blue colour much

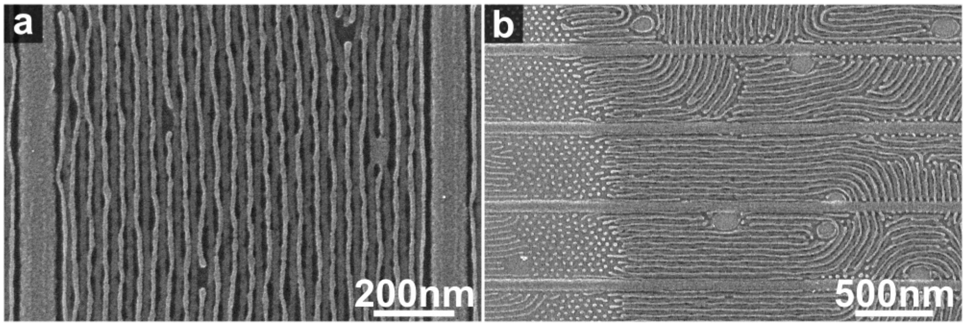

Figure 5.4: SEM images of line patterns from a 22.5% PS/PS-b-PDMS blend swelled to $D = 2.0$ along trenches with short walls. (a) A close-up of the patterns demonstrate that the same patterns span the entire width of the trench. (b) An SEM demonstrating how fingerprint patterns and terrace boundaries span across several trenches.

sooner than the rest of the unpatterned substrate. This meant that films confined by densely-packed lines increased in thickness more quickly than those confined by sparse lines, and BCP material moved from open areas to more confined areas. As a result, the use of topographic structures has the effect of changing the relative swelling rates of the films in different areas. This may be problematic if uniform swelling across the entire substrate is desired.

One possible strategy to reduce this problem may be to use shorter guiding features. The wall heights were reduced from 105 nm to 50 nm. These shorter wall features were expected to direct the assembly of line structures in the lower layers while still allowing some BCP spill over from adjacent trenches during the anneal step. Because of the lower degree of confinement, it was expected that the capillary action from these shorter walls would be significantly reduced, and that there would be less accumulation of thicker terrace regions near the walls. Figure 5.4 displays the BCP structures obtained when films of the 22.5% PS/PS-b-PDMS blends were self-assembled on these short line features. Uniform structures were formed across the entire width of the trenches irrespective of their widths. Some BCP features were also found to assemble on top of the walls (Figure 5.4a). However, because insufficient material was present to form bilayers uniformly across the entire substrate, terraced regions

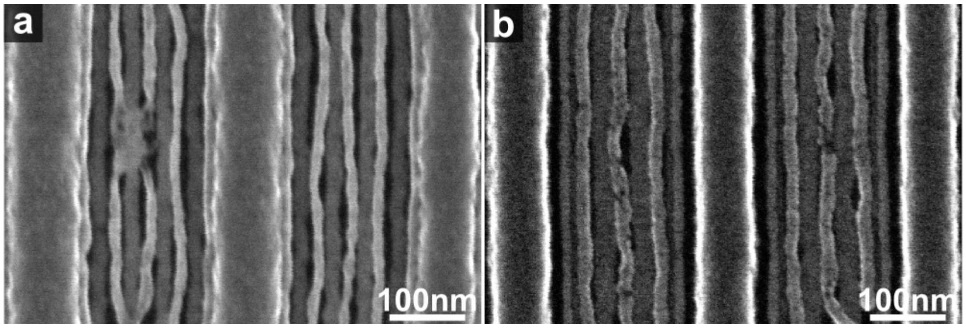

Figure 5.5: SEM images displaying a 22.5% PS/PS-*b*-PDMS blend self-assembling along wall features without a brush (a), and with a grafted PS brush (b).

similar to those formed on flat substrates were formed. These terraces did not accumulate along the walls, as was the case for the 105 nm walls, but instead spanned across trench regions and thus did not seem to correlate at all with the placement of the trench walls. Unlike in Figure 5.2, any defects or terraces that were observed in one trench often continued on to the adjacent trench. Figure 5.4b demonstrates several examples where fingerprint patterns span the widths of several trenches. Thus, while it seemed that lowering the height of the walls was an effective strategy for reducing the accumulation of trench patterns along the walls, it also allowed for the propagation of defects across trenches.

Besides altering the height of the topographic features, the features may also be modified with a brush layer to control the wetting behaviour of the BCP. Given a topographically patterned substrate with no brush layer modification, PDMS blocks were found to preferentially wet the sides of the patterned silica walls (see Figure 5.5). While this did not affect the orientation of the cylinders after self-assembly, it did lead to extra silica accumulating at the wall after the polymer structures were exposed to plasma. To rectify this problem, a PS brush was grafted to the substrate prior to the BCP film deposition and self-assembly. The PS brush changed the affinity of the sidewalls to favour PS wetting. Because PS may be subsequently removed by plasma, the resulting patterns always resulted in a space separating the BCP structures from

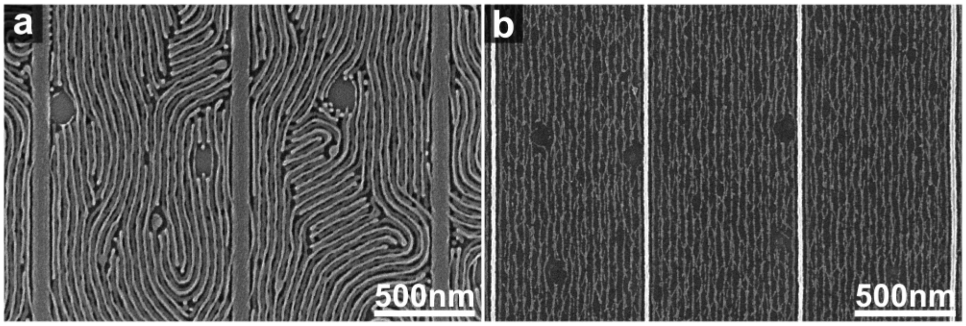

Figure 5.6: (a) Films annealed to $D = 2.0$ produced high-quality density-doubled lines with poor ordering. (b) When annealed to $D = 2.1$, the order of the lines was greatly improved, but the lines were also much thinner and wavier.

the silica walls. The brush layers did not have an affect on the terracing or structure types observed along the trenches.

5.3.2 Block Copolymer Ordering

For the BCPs to form perfectly aligned lines along the trenches, there must be sufficient mobility to allow the polymers to assemble into their thermodynamically favoured state. This may be done by increasing the degree of swelling to plasticize the BCP film. 22.5% PS/PS-*b*-PDMS films were annealed to $D = 2.0$ along trench patterns, but as shown in Figure 5.6a, this D was insufficient for inducing the growth of highly ordered lines. While some areas close to the trench walls displayed perfectly straight lines, other regions displayed fingerprint patterns. New BCP films were then annealed to a slightly higher degree of swelling ($D = 2.1$) to increase the mobility of the polymer films. As shown in Figure 5.6b, there was a significant improvement in the ordering of the BCP structures, and all the lines were shown to orient along the trench direction. However, the new problem was that the resulting structures became very narrow and wavy. This was likely due to the narrower diameters of these self-assembled cylinders, which made them more susceptible to etching and degradation during the plasma etch.

Thus, it may be concluded that while alignment in solvent annealing may be improved by increasing the degree of swelling, this approach is also limited by the fact that as the D is increased, there is also a corresponding increase in the line waviness. To attain structures with higher order while still maintaining the line quality, slower anneals to $D = 2.0$ must be implemented so that more time is given to the polymers to self-assemble and align along the trench directions.

5.4 Block Copolymer Multi-Step Patterning

While the density-doubling technique described in the previous chapters was effective in halving the feature pitch, several issues arose from using that method. As mentioned in Chapters 3 and 4, lines templated from the upper layers tended to be narrower than lines templated from the lower layers. The lines were also found to be more wavy than monolayer lines, suggesting a possible collapse in the PS underlayer. One alternative method of producing density-doubled features is to utilize multi-step patterning, similar to the double patterning techniques used in the semiconductor industry. One advantage gained from using multi-step patterning is the ability to tune and control the dimensions of each layer of cylinders separately.

Figure 5.7 demonstrates how this process may be applied. A thin film of BCP is initially deposited and self-assembled into a monolayer of cylinder or dot patterns. These BCP nanopatterns are then converted into silica or metal nanolines or nanodots, depending on the type of BCP used. To create metal nanostructures, PS-*b*-P2VP is simply self-assembled and metallized in an O_2 plasma step, as described in Chapter 3. To create silica nanopatterns, PS-*b*-PDMS is self-assembled and etched by a two-step CF_4 and O_2 plasma, as described in Chapter 4. A second BCP film is then deposited onto the patterned substrate, and the nanopatterns from the first step act as graphoepitaxial guides for the self-assembly of nanostructures in the second step. The cylinders or dot patterns from the second step are then converted into solid

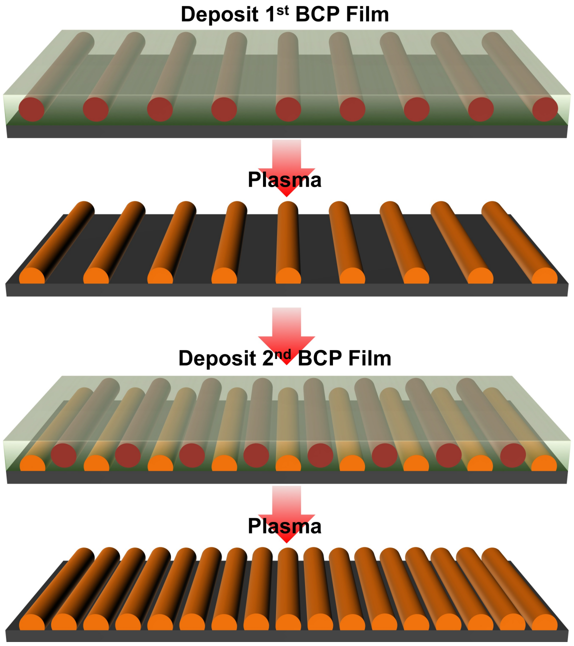

Figure 5.7: Schematic showing the sequential self-assembly and templating of nanostructures.

patterns using metallization or plasma treatments. This process could conceivably be repeated multiple times if so desired. The main limitation of this technique is the control of impurities and defects, as these would accumulate with the number of steps used in the fabrication process. Thus, although this method provides a high degree of flexibility in the type of nanostructure produced, it is also limited by the ability to maintain a high yield of desired structures at the end of each step.

The use of BCP-templated nanostructures to guide the assembly of more BCP-templated nanostructures has also been developed by other groups. The Ross group first used structures templated from a PS(31k)-*b*-PDMS(14.5k) polymer to guide the assembly of a smaller polymer, PS(11k)-*b*-PDMS(5k).[3] The work was then extended by using large line or perforated lamellar patterns templated from a large polymer to graphoepitaxially guide the assembly of dot or line patterns in a smaller polymer.[4] The result was a variety of hierarchical nanostructures patterned using two self-assembly steps (see Figure 5.8).

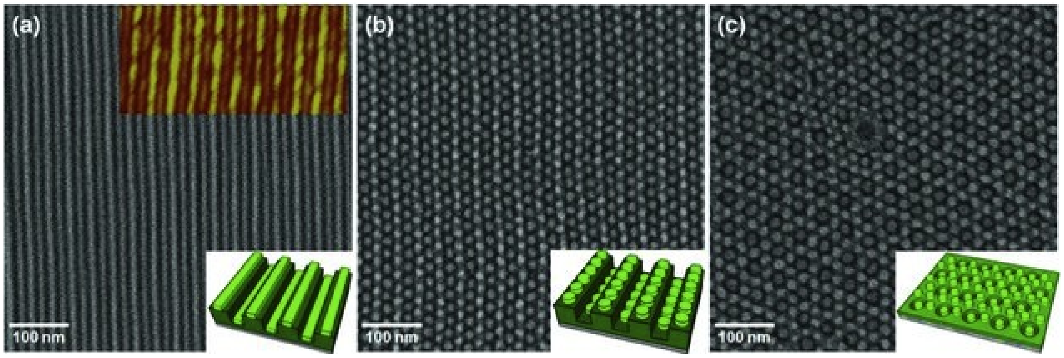

Figure 5.8: SEM images showing three examples where the self-assembly of small BCPs are guided by structures templated by a larger BCP. Reprinted with permission from ref. [4]. Copyright © 2011 Wiley-VCH.

Similarly, Polleux *et al.* also used a sequential BCP self-assembly process to produce titanium dioxide nanolines or nanodots around gold nanodots.[5]

Park *et al.* showed that self-assembled patterns from PS-*b*-PMMA could be used to create surface chemical patterns, which could then be used to direct the self-assembly of another layer of perpendicular lamellar PS-*b*-PMMA to form an identical pattern.[6] Similarly, Ruiz *et al.* demonstrated that horizontal cylinders could be etched half-way to produce aligned chemical patterns that could template the formation of subsequent perpendicular lamellar patterns.[7] This strategy was used because horizontal cylinders form ordered line patterns faster than perpendicular lamellae. Thus, by producing ordered lines assembled by the cylinders first, the authors hoped to reduce the overall assembly time of the ordered perpendicular lamellar lines.

5.4.1 Two-Step Patterning of Lines

While using a large polymer to guide the assembly of a smaller BCP has been demonstrated to be successful in producing hierarchical structures, the use of structures templated by the same polymer to guide its self assembly is slightly more difficult. One of the reasons is due to the fill ratio of the polymer: if the fill ratio of a monolayer structure is greater or equal to 0.5, then the second layer of lines is expected to touch the other cylinders. The methods for tuning nanostructure dimensions developed in Chapter 4 enables this approach to feasibly create density-doubled nanopatterns.

To demonstrate this process, a 38 nm neat BCP film was spin cast onto a sample coated with a PS brush, and solvent annealed with THF to $D = 1.75$. After a two-step plasma treatment, a low-magnification SEM image demonstrated that both monolayer and bilayer regions were present in the sample (Figure 5.9). To facilitate identification of the regions, false colour was added to the SEM images to help identify the different structures in their corresponding regions. The monolayer and bilayer structures were as described in Chapter 4. A second BCP film of approximately the same thickness was then deposited and solvent annealed with THF to $D = 1.75$. After another two-step plasma treatment, the resulting structures were examined using an SEM again. Each BCP film contributed both monolayer and bilayer regions, and so in the multi-step approach, combinations of these regions resulted in three very distinct regions, as observed in the low-magnification SEM image in Figure 5.9d. An image displaying the intersection of all three regions was displayed in Figure 5.9e. The majority blue region clearly displayed a monolayer region self-assembled onto another monolayer region. Unlike the density-doubled lines templated by pure bilayer regions, these density-doubled lines were well-spaced and had similar widths. The red and green regions both appeared to contain at least 3 layers of lines. By observing the line behaviour near defect regions such as the ones shown in Figure 5.9e, inferences could be made on the composition of these regions. For example, the large circular defect in the green regions seemed to suggest that those regions were composed of monolayers from the first BCP film and bilayers from the second BCP film. On the other hand, the similarity in shape of the red regions to the magenta regions suggested that the red regions were composed of bilayers from the first BCP film and monolayers from the second. Interestingly, many of the green regions also tended to form along the edges of red regions, suggesting that the red regions may have helped to seed the growth of green regions. The occurrence of red and green regions may be reduced by finely tuning the initial thicknesses of the films, but the

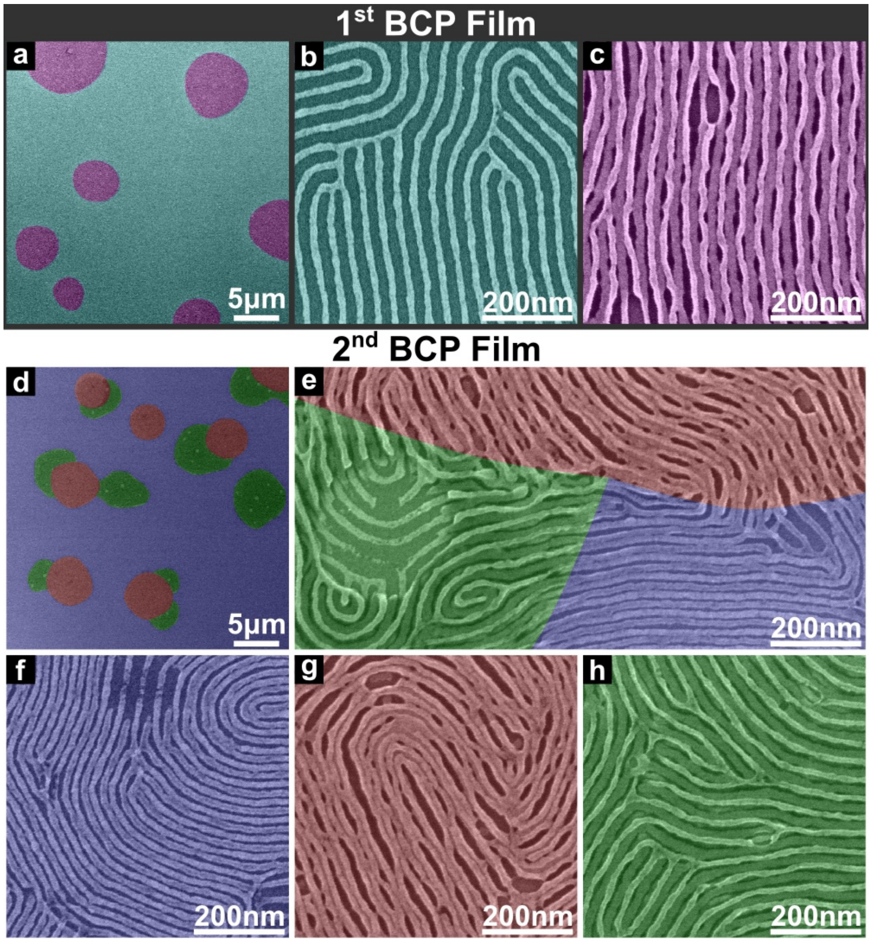

Figure 5.9: SEM images of the terraces (a), monolayer regions (b), and bilayer regions (c) were obtained after the first deposition and plasma steps. The monolayer regions are denoted with cyan, and the bilayer regions are denoted with magenta. After the second deposition and plasma steps, SEM images were obtained of the terraces (d), the region intersections (e), and of the individual regions (f-h). Red, blue, and green false colour was added to denote the different regions.

focus of this study was on the optimization of structures in the blue regions. Thus, for the remainder of the chapter, we focus solely on regions formed from the sequential addition of monolayer nanostructures.

To observe the evolution of the density-doubled structures over time, neat BCP films were deposited on silicon substrates and annealed in identical neat THF vapour conditions to $D = 1.75$. The samples were then treated with 10 s CF_4 plasma followed by a 50 s 10% CF_4/90% O_2 plasma. The resulting monolayer and bilayer line structures are displayed in Figure 5.10a. A second BCP film was then deposited and annealed with neat THF vapour to $D = 1.75$. After a 10 s CF_4 plasma to remove the overlying PDMS layer, the nanolines were as shown in Figure 5.10b. At this point, the samples were subject to different plasma conditions for varying durations of time.

In Figure 5.10c, the samples were subject to 100% O_2 plasma from 10 to 120 s. One noticeable difference from the density-doubled lines templated from bilayer structures was that the bright lines were from the lower layer cylinders. These lines were found protruding from underneath the films at the circular defects displayed in some of these images. After 20 s of exposure to this plasma, no significant change in the line structures were observed. This is due to the fact that the O_2 plasma is very limited in its ability to etch PDMS. Thus, after the PS matrix was removed, no noticeable change occurred for the remainder of the 120 s.

The samples were also subject to 10% CF_4/90% O_2 plasma from 10 to 120 s, as shown in Figure 5.10d. As the duration of plasma was increased from 10 to 40 s, lines templated from the second film became narrower and brighter. From 40 to 120 s, lines templated from both the first and second film became difficult to distinguish from each other because they both had similar brightness and widths. At 120 s, some of the lines appeared rough, suggesting that they had become over-etched. The lines were also well-spaced and did not contain the undulations observed in lines templated from BCP bilayers, even after 120 s. Similar results were observed with 20% CF_4/80% O_2 plasma (Figure 5.10e) except the lines were more well-spaced, and significant LER developed after

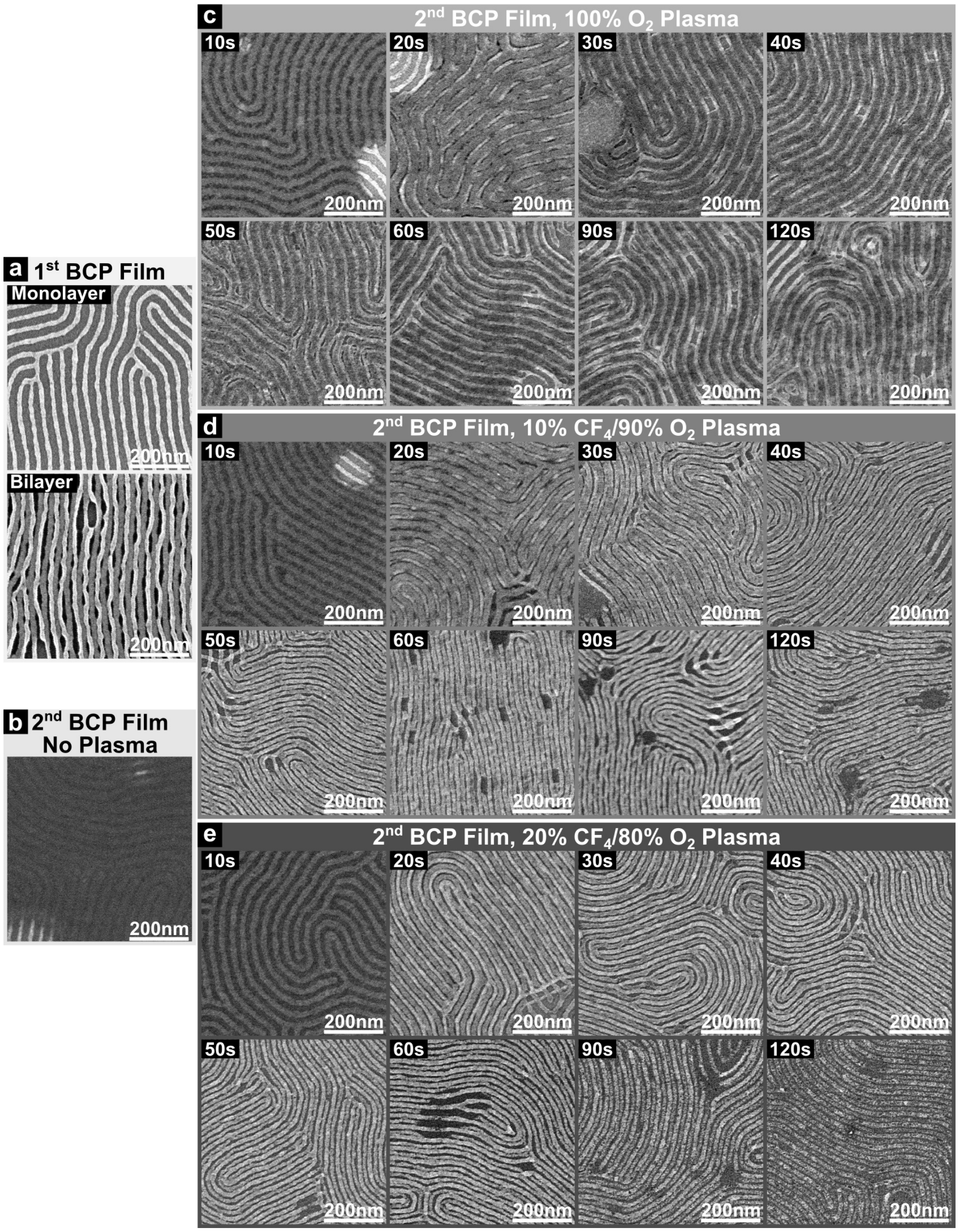

Figure 5.10: (a) Neat BCP films were annealed with THF vapour to $D = 1.75$ and subject to the two step plasma treatment, producing monolayer and bilayer regions. (b) A second BCP film was then annealed with THF vapour to $D = 1.75$ and subject to a 10 s CF_4 plasma treatment. SEM images of the evolution of line structures over time in a 100% O_2 plasma (c), a 10% CF_4/90% O_2 plasma (d), and a 20% CF_4/80% O_2 plasma (e) were then obtained.

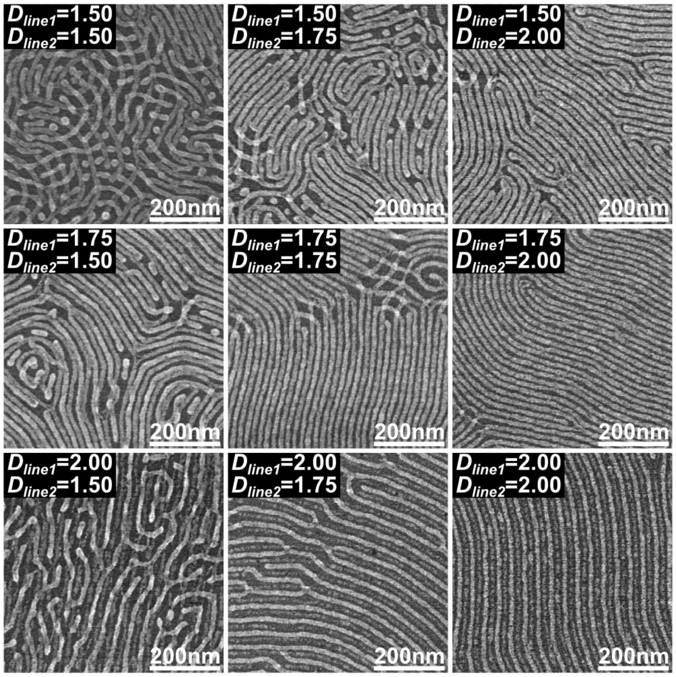

Figure 5.11: First and second layers of line forming BCP films were spin coated on the substrate, swelled to $D = 1.50, 1.75, 2.00$, and subject to plasma. The resulting line structures were captured using SEM.

around 60 s of plasma. Again, no line undulations were observed even after 120 s of plasma. Out of the conditions tested, the 20 % CF_4 plasma conditions gave the widest spaces between lines, and a plasma duration of 50 s seemed to give good quality lines without significant degradation in line edge roughness. Thus, it was decided that the plasma treatment to be used for all BCP films would consist of a 10 s CF_4 plasma followed by a 50 s 20% CF_4/80% O_2 plasma.

To investigate the tolerance of BCP ordering to the underlying pitch, the line pitch of the first and second layer films were varied with respect to each other. As shown in Chapter 4, an increase in swelling during the annealing portion of the anneal resulted in narrower lines with smaller pitch. Thus, by selecting the D of the first and second layer films to be $D = 1.50, 1.75, 2.00$, the tolerance to pitch mismatches may be investigated. After each layer was annealed, the sample was subjected to the standard two-step plasma treatment selected above (10 s CF_4 plasma followed by 50 s 20% CF_4/80% O_2 plasma). The resulting samples are displayed in Figure 5.11. It became immediately apparent that the differences in pitch did not have a significant effect on the pattern imitation. As shown in images along the top row, as D_{line2} was increased from 1.50 to 2.00 (with $D_{line1} = 1.50$), the number of intersection points between lines from the two layers was found to decrease. This trend was also apparent for samples with D_{line1} equal to 1.75 or 2.00. Thus, the most obvious determiner of pattern imitation of the first layer was D_{line2}. One likely explanation is that as D_{line2} increases, greater mobility is afforded to the second layer film to allow the patterns to arrange between features templated by the first layer.

5.4.2 Three-Step Patterning of Features

The multi-step patterning technique described above is not limited to two layers of structures. In the case of dot patterns, for example, a third layer of dot patterns could potentially create density tripled arrays of hexagonally close-packed dots (Figure 5.12a). To confirm whether the arrangements described in the schematic were possible, a dot-forming 30% blend of PS with PS-*b*-PDMS was deposited on a sample and annealed to $D = 1.75$. This blend was shown in Chapter 4 to produce highly ordered hexagonally-packed dot patterns. After the standard two-step plasma treatment (10 s in CF_4 followed by 50 s in 20% CF_4/80% O_2), an ordered hexagonal array of dot patterns was observed (Figure 5.12b). A second dot-forming blend was deposited and the same process was repeated to produce a dot array of open hexagon outlines (Figure 5.12c). A third layer was then deposited under the same conditions, and the result was the predicted density-tripled hexagonally close-packed array of dots (Figure 5.12d). Thus, it is possible to use multi-step patterning to triple the density of dot patterns on the substrate. One disadvantage, however, was that each new layer also contained terraces and disordered hexatic dot structures, and thus the areas containing the desired triple density dot patterns was reduced considerably when compared to samples with only one or two layers.

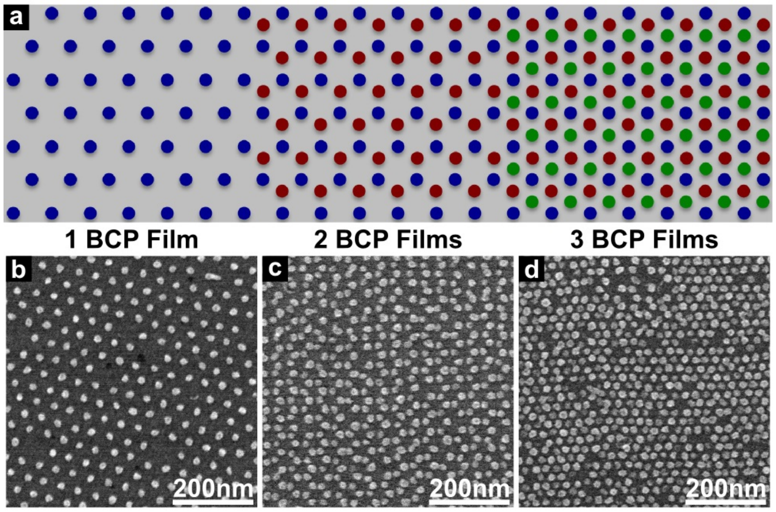

Figure 5.12: (a) Schematic illustrating how monolayer films of dot patterns stack with respect to each other. SEM images were obtained of the line structures after one (b), two (c), and three (d) film deposition steps.

The multi-step patterning technique could also be extended beyond 2 layers in line-forming polymers. A neat PS-*b*-PDMS film was deposited, annealed to $D = 1.75$, and etched with the standard plasma described above. While the second layer of lines is known to deposit between lines from the first layer, it was not immediately clear how the third layer of lines would deposit. A slight height difference was thought to exist between lines templated from the first two layers of cylinders, and this difference may have had the potential to direct the assembly of the third layer. Unfortunately, because of the narrow pitch of these lines, AFM profiles could not be taken to reliably determine the height difference between the two layers. SEM images of the sample after the third layer was deposited demonstrated that in some areas, lines from the third layer did indeed form parallel and directly above lines templated from the first layer. The majority regions, however, showed no correlation between the third layer lines and the underlying two layers (Figure 5.13). Thus, it appeared that any height difference that existed between lines from the first two layers was not always significant enough to direct the alignment of the third layer lines.

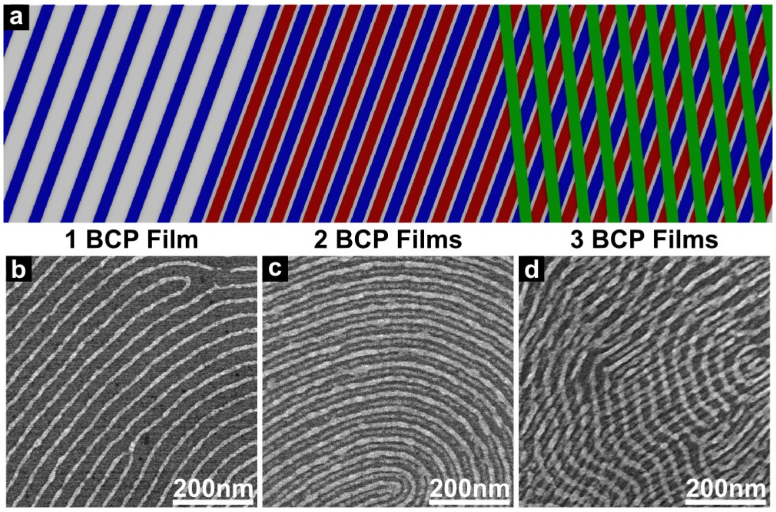

Figure 5.13: (a) Schematic illustrating how monolayer films of line patterns stack with respect to each other. SEM images were obtained of the dot structures after one (b), two (c), and three (d) film deposition steps.

5.4.3 Non-Equilibrium Nanostructures

Besides doubling or tripling the density of nanofeatures, the use of multi-step patterning also has the potential for creating patterns not normally accessible in standard patterning techniques. For example, one pattern of particular interest for dynamic random-access memory (DRAM) fabrication is the formation of line patterns interspersed with dot patterns, as shown in Figure 5.14. These patterns have been created by diBCP blends in the past,[8] however it was with the help of dense pre-patterned chemical features on the substrate that provided 1:1 registration with the BCP domains. In the work here, we produced these patterns without the use of dense chemical pre-patterns by sequentially depositing dot-forming and line-forming BCP layers. In these experiments, dots were formed using the 30% PS/PS-*b*-PDMS blends, while lines were formed using neat PS(31k)-*b*-PDMS(14.5k).

The two layers may be deposited either using a dots-first or lines-first approach. In the dots-first approach, as shown in Figure 5.15a, a dot layer was first deposited on the substrate and was used to guide the assembly of the

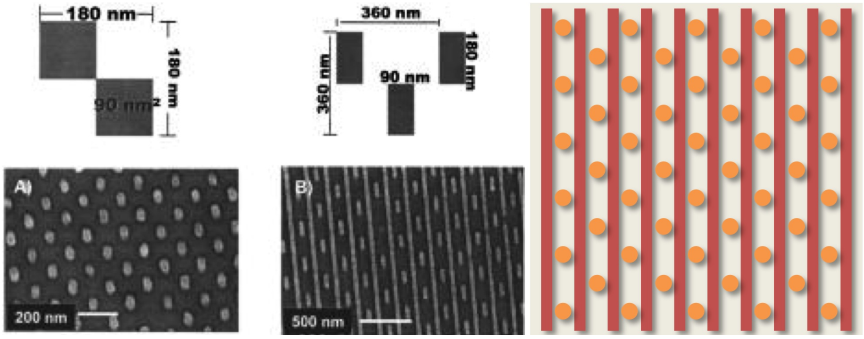

Figure 5.14: Patterns consisting of lines interspersed by hexagonally-packed dots may be used to fabricate DRAM cells. Reprinted with permission from ref. [9]. Copyright © 2005 American Vacuum Society.

subsequent line layer. The D of both layers were varied from 1.50 to 2.00, but no significant difference was observed in the structures, so a representative sample with $D_{dot1} = 1.75$ and $D_{line2} = 1.75$ is displayed. The line patterns consistently passed through or engulfed the existing dot patterns, forming connections between neighbouring dots instead of assembling between them, as was required for the patterns in Figure 5.14. This phenomenon, which was also observed by Yang *et al.*,[10] was a result of the selectivity of the dots towards the minority PDMS blocks in the second layer. Thus, as a result of this selectivity, the dots-first approach was unsuccessful in producing the desired patterns.

In the lines-first approach, line patterns were first deposited onto the substrate and used as guiding features for the assembly of the subsequent dot layer. The SEM of a representative sample with $D_{line1} = 1.75$ and $D_{dot2} = 1.75$ is shown in Figure 5.15b. In contrast to the dot-first approach, the lines-first approach was highly successful in producing lines with dots interspersed between adjacent lines. Because spheres are structures that are confined in all three dimensions, it was more energetically favourable for the spheres to be independent than to be bound or connected to an underlying line feature. Defects where dots were replaced by short lines were still observed in many of these samples, and further process optimization is required before these patterns can be used for DRAM fabrication. One strategy to reduce these defects may be to use

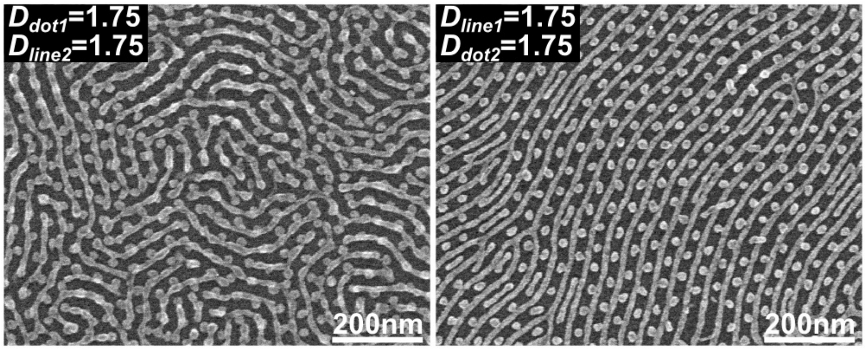

Figure 5.15: SEM images of structures produced in a dots-first approach (left) and in a lines-first approach (right).

a neat spherical-forming BCP instead of the current PS/PS-*b*-PDMS blends. The results presented here, however, are a proof of concept that interesting non-equilibrium structures may be patterned using multi-step patterning.

5.5 Conclusions

Graphoepitaxy is a powerful method for directing the self-assembly of BCPs. By laterally confining polymer films using lithographically templated features, dot and line features produced by BCPs may be induced to form highly ordered patterns. One effect that must be considered when using graphoepitaxy, is the ability for the walls to induce the redistribution of BCPs through capillary effects during solvent annealing. These effects could be minimized by reducing the wall heights of the trenches. Additionally, features templated by BCPs may also be used as guiding structures for the graphoepitaxy of subsequent layers of BCP films, and this ability formed the basis of the multi-step patterning approach. The multi-step patterning approach was demonstrated to be successful not only in doubling line densities, but also in tripling the density of hexagonally-packed dots and in forming non-equilibrium arrangements that could be useful for DRAM manufacturing.

References

[1] R. A. Segalman *et al.*, "Topographic templating of islands and holes in highly asymmetric block copolymer films," *Macromolecules*, vol. 36, no. 12, pp. 4498–4506, 2003.

[2] R. Ruiz *et al.*, "Local defectivity control of 2D self-assembled block copolymer patterns," *Advanced Materials*, vol. 19, no. 16, pp. 2157–2162, 2007.

[3] Y. S. Jung *et al.*, "A path to ultranarrow patterns using self-assembled lithography," *Nano Letters*, vol. 10, no. 3, pp. 1000–1005, 2010.

[4] J. G. Son *et al.*, "Hierarchical nanostructures by sequential self-assembly of styrene-dimethylsiloxane block copolymers of different periods," *Advanced Materials*, vol. 23, no. 5, pp. 634–639, 2011.

[5] J. Polleux *et al.*, "Benzyl alcohol and block copolymer micellar lithography: A versatile route to assembling gold and *in situ* generated titania nanoparticles into uniform binary nanoarrays," *ACS Nano*, vol. 5, no. 8, pp. 6355–6364, 2011.

[6] S.-M. Park *et al.*, "Combinatorial generation and replication-directed assembly of complex and varied geometries with thin films of diblock copolymers," *Langmuir*, vol. 23, no. 17, pp. 9037–9045, 2007.

[7] R. Ruiz, R. L. Sandstrom, and C. T. Black, "Induced orientational order in symmetric diblock copolymer thin films," *Advanced Materials*, vol. 19, no. 4, pp. 587–591, 2007.

[8] H. Kang, G. S. W. Craig, and P. F. Nealey, "Directed assembly of asymmetric ternary block copolymer-homopolymer blends using symmetric block copolymer into checkerboard trimming chemical pattern," *Journal of Vacuum Sciences & Technology B*, vol. 26, no. 6, pp. 2495–2499, 2008.

[9] M. Fritze *et al.*, “Hybrid optical maskless lithography: Scaling beyond the 45 nm node,” *Journal of Vacuum Sciences & Technology B*, vol. 23, no. 6, pp. 2743–2748, 2005.

[10] J. K. W. Yang *et al.*, “Complex self-assembled patterns using sparse commensurate templates with locally varying motifs,” *Nature Nanotechnology*, vol. 5, no. 4, pp. 256–260, 2010.

6

Conclusions

6.1 Thesis Summary

The primary aim of this thesis was to establish different methods for pushing the pattern density limits of BCPs, and to elucidate the different structural and film transformations that take place throughout the solvent annealing process using *in situ* ellipsometry, optical microscopy, SEM, and AFM. Using this information, different process parameters were varied to fine-tune the dimensions of resulting nanopatterns. This chapter will summarize the highlights and developments discussed in previous chapters and will then explore some potential future research directions.

Chapter 1 began by presenting the challenges facing the semiconductor industry as it strives to continually shrink the critical dimensions of nanofabricated devices. Several new technologies currently under investigation as candidates for next-generation lithography were then described, including EUVL, maskless lithography, NIL, and DSA.

In chapter 2, the basic principles of polymer chemistry and the thermodynamics of bulk and thin-film BCP self-assembly were introduced. Different techniques for improving BCP ordering were then explained, including increasing the mobility of polymer chains, introducing external fields to direct the orientation of self-assembled domains, and using substrate topography and surface chemical patterns to guide the assembly process. The chapter then closed with a description of different methods for converting these self-assembled domains into free-standing nanostructures.

Chapter 3 introduced a new concept of density-doubling using solvent-annealed bilayer films of cylinder-forming BCPs. The evolution of nanostructures and film thickness throughout the solvent anneal was elucidated through investigations using *in situ* ellipsometry, microscopy, SEM and AFM. It was determined that the BCP domain morphology was closely-linked to D, the initial film thickness, the presence of water, and the ambient temperature. As the swelling progressed, the films were also found to form discrete steps known as terraces. Thus, the swelling must be carefully controlled to maximize the production of density-doubled patterns across a substrate.

Chapter 4 expanded the utility of the density-doubling technique by introducing various methods for tuning the critical dimensions of line patterns templated by bilayer cylinders of PS-*b*-PDMS. Swelling the film with solvents or PS homopolymer, adjusting the BCP/substrate interface, and varying plasma duration and composition were all strategies that were explored for tuning the line widths and pitch to the desired pattern specifications. The percent coverage of bilayer regions over the substrate surface could also be maximized by adjusting the swelling and initial film thickness.

Finally, in chapter 5, topographic patterns fabricated from EBL were used to guide the self-assembly of density-doubled line patterns. The height of the walls were found to affect the terracing behaviour of the films during swelling, and in some cases also led to polymer redistribution. Sufficient swelling was required for the BCP cylinders to align along these topographic patterns, but excess amounts also led to a degradation of the line structure. A polymer multi-step patterning approach was then used as an alternative method for producing dense arrays of dots or lines. Compared to the bilayer approach, differences between lines templated from different layers were less pronounced. This strategy could also be used to produce density-tripled dot patterns and some complex non-equilibrium structures.

6.2 Future Research Directions

Solvent annealing is a very important annealing technique and was used extensively throughout the work described in the thesis. However, one limitation of solvent annealing is that a significant portion of the anneal is spent swelling the film to the target D. Because this portion of the anneal is generally characterized by low polymer mobility, no significant or lasting changes to the BCP nanostructures are made, and the time is wasted. In addition, the constant change in D during the solvent anneal promotes the constant growth of terrace structures, thus limiting the ability for the BCP domains to self-assemble with higher order. The ideal swelling curve for maximizing the ordering efficiency of the anneal would consist of a rapid swell to the target D, followed by an extended period where the D is held constant. Thus, the future of solvent annealing will be in gaining greater control over the film swelling. One obvious strategy for rapidly swelling a BCP film to the desired D is to use smaller anneal chambers with higher solvent evaporation or leakage rates, as shown in Figure 3.13. For even faster swelling, the anneal chamber could also be pre-saturated with solvent vapour such that when the sample is inserted, there is an immediate swell in the film to a higher D. Preliminary tests with these pre-saturated systems have shown promising near-instantaneous swelling responses by the BCP films. The use of computer-controlled mass flow controllers to manipulate the flow of solvent vapour into and out of the anneal chamber may also be another possibility for controlling the film swelling.

The bilayer patterning strategy described in chapters 3 and 4 could be improved considerably if lines templated from upper and lower cylinders were more similar in width and in colour. In the case of PS-*b*-P2VP, longer or more concentrated metallization exposures may provide more equal metallization between upper and lower layer lines, and changes in the plasma conditions may also allow the line etching in the upper and lower layer cylinders to be more similar. As for the polymer PS-*b*-PDMS, variations in plasma compositions were found to affect the line widths of both upper and lower layer cylinders. It was found, however, that excessive plasma resulted in an increase in line undulations. As described in chapter 4, one possible cause of the undulations was the low melting point of PDMS, and the collapse of the underlying PS support before the PDMS could properly cross-link. Thus, one option is to cross-link the PDMS prior to plasma treatment. Another possible cause of the undulations was the rapid relaxation step after the end of the anneal, which led to rapid changes in the film thickness. In such a case, a possible solution may be to introduce a gentle secondary thermal anneal to correct for these errors.

The multi-patterning technique described in chapter 5 was found to be extremely sensitive to defects. Defect control in this multi-patterning step is even more crucial than in the bilayer patterning approach because multiple self-assembly steps are required. Thus, for the entire process to produce <0.01 defects/cm^2, each layer must produce even fewer defects. Minor fluctuations in film thickness or particles trapped in the polymer films were also found to heavily influence the uniformity of subsequent films deposited on the substrates. To reduce these problems the polymer solutions may require purifying or filtering and all processing steps may be required to take place within a clean room. The film swelling must also be controlled with a high degree of precision to ensure uniform coverage of monolayer cylinders across the entire substrate. Finally, a method for aligning and ordering these structures must be used. Graphoepitaxy, chemical epitaxy, or even the use of external fields such as shear are possible methods for increasing the ordering of these multi-patterned nanostructures.